UTS

Robust Sensor Technologies Combined with Smart Predictive Analytics for Hostile Sewer Infrastructures

by

Karthick Thiyagarajan

A dissertation submitted in partial fulfillment of the requirements for the degree of Doctor of Philosophy

at the
Centre for Autonomous Systems
Faculty of Engineering and Information Technology
University of Technology Sydney

25th July 2018

Declaration of Authorship

I certify that the work in this dissertation has not previously been submitted for a degree nor has it been submitted as part of requirements for a degree except as fully acknowledged within the text.

I also certify that the dissertation has been written by me. Any help that I have received in my research work and the preparation of the dissertation itself has been acknowledged. In addition, I certify that all information sources and literature used are indicated in the dissertation.

Signed: Production Note:
Signature removed prior to publication.

Date: **25th July 2018**

UNIVERSITY OF TECHNOLOGY SYDNEY

Abstract

Faculty of Engineering and Information Technology
Centre for Autonomous Systems

Doctor of Philosophy

by Karthick Thiyagarajan

Underground sewer systems are an important national infrastructure requirement of any country. In most cities, they are old and have been exposed to significant levels of microbial induced concrete corrosion, which is widely regarded as a serious global problem as they pose threats to public health and cause economic repercussions to water utilities. In order to maintain those underground assets efficaciously, it is pivotal for water utilities to estimate the amount of intact concrete left to rebar by predicting the rate of corrosion throughout the sewer network. Existing predictive models incorporate concrete surface temperature and surface moisture conditions as observations. However, researchers and water utilities often use indirect measures like ambient temperature and humidity data as inputs to their models. This is primarily due to unavailability of proven technologies in the state-of-the-art systems and sensing limitations predominantly attributed to the corrosive nature of the sewer environment. Hence, the focus of this dissertation is to provide reliable measures of surface temperature and moisture conditions by developing robust sensor technologies that can facilitate measurements under the hostile sewer conditions.

This dissertation encompasses three main parts:

In the first part, a robust sensor technology using an infrared radiometer sensor for quantifying surface temperature dynamics inside concrete sewer pipes is proposed. In this regard, the sensor was comprehensively evaluated in the laboratory conditions to

study the effects of optical window fogging, incident angle, limit of detection, distance, lighting conditions, reproducibility, humidity and increased surface temperature conditions. Thereafter, the sensor was deployed in sewer pipe for real-time continuous measurements. The field study revealed the suitability of the proposed sensor technology for non-contact surface temperature measurements under the hostile sewer environment. Further, the accuracy of the sensor measurements was improved by calibrating the sensor with emissivity coefficient of the sewer concrete.

In the second part of the dissertation, a non-invasive sensing technique to determine the concrete surface moisture conditions is proposed. In this context, laboratory experiments were conducted to study the behaviour of concrete moisture to electrical resistance variations and different pH concentrations. This study led to utilize the Wenner array method to determine the surface moisture conditions based on concrete surface electrical resistivity measurements. Then, the sensor suite was deployed in concrete sewer pipe to measure the surface resistivity for about three months. Upon on-site calibration, surface moisture conditions were determined and thereof, the field campaign exhibited the feasibility of the proposed sensing method. Further investigations were conducted to locate the reinforcing bar embedded in concrete for optimal sensor installation in order to minimize the effects of reinforcing bar during measurements.

In the third part, sensor technologies were combined with smart predictive analytics to develop a diagnostic toolkit that can digitally monitor the health conditions of the sensors is proposed. This toolkit embraces a seasonal autoregressive integrated moving average model with statistical hypothesis testing technique to enable temporal forecasting of sensor data; identify and isolate anomalies in a continuous stream of sensor data; detect early sensor failure and finally to provide reliable estimates of sensor data in the event of sensor failure or during the scheduled maintenance period of sewer monitoring systems.

Overall, this dissertation significantly contributes to ameliorating the way sewer assets are monitored and maintained in Australia and globally by providing information-rich new data to the predictive models for better corrosion prediction.

Acknowledgements

This dissertation is the result of the research conducted by me during the last four years at the Centre for Autonomous Systems of The University of Technology Sydney, Australia. The presented work is part of a water industry led collaborative project, "Data Analytics on Sewers", funded by Sydney Water Corporation, Melbourne Water Corporation, Water Corporation (WA) and South Australian Water Corporation. The research participants are Data61-Commonwealth Scientific and Industrial Research Organization (CSIRO), University of Technology Sydney (UTS) and University of Newcastle (UoN).

This dissertation is a reality today mainly due to the astounding support and constant guidance of my primary supervisor Prof. Sarath Kodagoda. I sincerely thank him for being inspirational, motivational and making me realize my endurance and fortitude towards research. His research acumen on sensing technologies was pivotal for me in accomplishing this dissertation. Above all, I admire his way of supervision, always open to discussion and never the source of disappointment. Further, I owe my gratitude to my co-supervisor Distinguished Prof. Gamini Dissanayake for accepting me as his student. His suggestions and in-depth knowledge of robotics and sensing technologies were instrumental in producing this dissertation. At this junction, I truly appreciate UTS for offering me the UTS President's Scholarship (UTSP) to assist with living cost and UTS International Research Scholarship (IRS) to cover the tuition fees of my doctoral candidature.

I truly appreciate the support offered by the industrial partners of "Data Analytics on Sewers" project in successful completion of this dissertation. Specially, I would like to acknowledge the support of Mr. Dammika Vitanage, Mr. Gino Iori, Mr. Craig Earl, Mr. Jeremy Hearfield, Mr. Derek Cunningham and Mr. Steve Barclay from Sydney Water Corporation. Technical discussions with Dr. Fang Chen, Dr. Yang Wang and Dr. Bin Li from Data61-CSIRO during Technical Committee Meeting for Sewer Corrosion project were valuable in gaining insights about corrosion modelling. In addition, Prof. Robert Melchers and Prof. Tony Wells helped me to gain domain knowledge on concrete corrosion.

I would like to express my gratitude to Dr. Ravindra Ranasinghe for being my assessor during candidature assessment and providing insightful comments, constructive feedbacks for journals and warm encouragement. I have greatly benefited from the support extended by Dr. Nalika Ulapane and Dr. Linh Nguyen while working on probabilistic models. Kyle

Alvarez has always been a helping hand for me in tackling the engineering aspects of the research.

Working as an academic tutor in the Faculty of Engineering and Information Technology has been one of my rewarding experiences at UTS. I am much obliged to Prof. Sarath Kodagoda, Prof. Shoudong Huang, Prof. Robert Fitch and Dr. Gavin Paul for hiring me to teach Mechatronics subject and mentor projects for Advanced Robotics and Mechanical and Mechatronic Design subjects during the tenure of my Ph.D. candidature.

I am glad to have the acquaintance of Dr. Hayat Al-Dmour, Dr. Deepak Puthal, Dr. Alaa Al-Kaysi, Asma Al-Kabani, Fatma Al-Widyan and Ashish Nanda for being an integral part of the Ph.D. journey filled with euphoric moments and miseries. Thanks Ramya for all the blissful occasions during my Ph.D. Further, I wish to acknowledge my colleagues and friends from CAS for their unconditional support.

This thesis stands as a testament to a lifetime of endless love and unconditional support shown by my parents to bring my long passion for research into fruition. Special mention to my dad for providing the care, love, needs, and support. You have been the clandestine fabric of what I am today. Thanks daddy for everything, without you this dissertation would have been a distant dream.

Contents

Declaration of Authorship i

Abstract ii

Acknowledgements iv

List of Figures x

List of Tables xiii

Nomenclature xvii

Glossary of Terms xxi

1 Introduction 1
- 1.1 Hostile Sewer Infrastructures . . . 3
- 1.2 Research Motivation . . . 5
- 1.3 Statement of the Problem . . . 7
- 1.4 Principal Contributions . . . 9
- 1.5 First Published Appearances of the Described Contributions . . . 10
  - 1.5.1 Journals . . . 10
  - 1.5.2 Conference Proceedings . . . 11
  - 1.5.3 Technical Reports . . . 11
- 1.6 The Structure of the Dissertation . . . 12

2 Robust Sensor Technology for Measuring Surface Temperature in Sewers 13
- 2.1 Introduction . . . 13
- 2.2 Scoping Study: Sensors for Surface Temperature Measurements . . . 16
  - 2.2.1 Sensors for Surface Temperature Measurements . . . 16
    - 2.2.1.1 Fluid Expansion Type Temperature Measurement Devices 17
    - 2.2.1.2 Bimetallic Temperature Measurement Devices . . . 17
    - 2.2.1.3 Resistive Temperature Measurement Devices . . . 18
    - 2.2.1.4 Thermocouple Sensors . . . 19

2.2.1.5 Thermistors . . . 19
2.2.1.6 Infrared Temperature Measurement Devices . . . 21
2.2.1.7 Fiber Optic Type Temperature Measurement Device . . . 24
2.2.1.8 Distributed Temperature Sensing . . . 26
2.2.2 Feasibility . . . 26
2.2.2.1 Temperature Conditions Inside Australian Sewers . . . 27
2.2.2.2 Comparative Analysis . . . 28
2.2.3 Concluding Remarks . . . 29
2.3 Sensor Characterization and Development for Measuring Surface Temperature 29
2.3.1 Assessment of Infrared Radiometer (IRR) Sensor's Optical Window in Varied Humidity Conditions . . . 30
2.3.2 The Effects of Incident Angle on the IRR Sensor Performance and their Limit of Detection . . . 30
2.3.3 Distance, Lighting Condition and Reproducibility . . . 31
2.3.4 Performance of IRR Sensor in Higher Humidity Conditions . . . 31
2.3.5 IRR Sensor Performance with Varying Surface Temperatures . . . 31
2.3.6 Sensor Development and Packaging . . . 32
2.4 Field Deployment for Real-time Continuous Measurements Inside Hostile Sewer Infrastructure . . . 35
2.5 Post-deployment Validations of the IRR Sensor After Long Exposure to Hostile Sewer Conditions . . . 38
2.6 Improving Surface Temperature Measurements of IRR Sensor based on On-site Calibration . . . 38
2.6.1 Theoretical Considerations and On-site Calibration . . . 38
2.7 Experimental Results . . . 40
2.7.1 Pre-deployment Evaluation: Sensor Characterization and Development . . . 41
2.7.1.1 Evaluation of IRR Sensor's Optical Window . . . 41
2.7.1.2 Evaluating the Effects of Incident Angle and Limit of Detection . . . 42
2.7.1.3 Evaluating the Effects of Distance, Lighting Condition and Reproducibility . . . 43
2.7.1.4 Evaluating the Performance of IRR Sensor in Higher Humidity Conditions . . . 44
2.7.1.5 Evaluating the IRR Sensor Performance with Varying Surface Temperatures . . . 45
2.7.1.6 Sensor Development and Packaging Prior to Sewer Deployment . . . 46
2.7.2 Field Deployment Experimentation: Data Collection and Analysis . 47
2.7.2.1 Real-time Sensor Data Showing Temporal Dynamics of Surface Temperature Measurements from the Sewer Pipe . 47
2.7.2.2 Comparative Analysis of Temperature Variables Data . . . 48
2.7.3 Post Deployment Validations . . . 49
2.7.4 Improved Measurements of IRR Sensor with Post Calibration Analysis 50
2.8 Summary . . . 51

3 Robust Sensor Technology for Measuring Surface Moisture in Sewers 54
3.1 Introduction . . . 54
3.2 Scoping Study: Sensors for Surface Moisture Measurements . . . 56
3.2.1 Sensors for Moisture Sensing . . . 57
3.2.1.1 Gravimetric Method . . . 57
3.2.1.2 Gamma Densitometry Method . . . 58
3.2.1.3 Electrical Resistivity Method . . . 58
3.2.1.4 Capacitance Sensor . . . 59
3.2.1.5 Resonator Based Methods . . . 60
3.2.1.6 Time Domain Reflectometry based Sensors . . . 61
3.2.1.7 Frequency Domain Reflectometry based Sensors . . . 62
3.2.1.8 Fibre Optic Sensors . . . 62
3.2.1.9 Micro Electro Mechanical Systems Sensors . . . 64
3.2.1.10 Hyperspectral Sensing . . . 65
3.2.2 Feasibility . . . 65
3.2.3 Concluding Remarks . . . 67
3.3 Experimental Evaluation to Study the Behaviour of Concrete Moisture with Electrical Resistance and pH Conditions . . . 67
3.3.1 Experimental Approach . . . 67
3.3.1.1 Concrete Sample Preparation . . . 67
3.3.1.2 pH Measurements . . . 68
3.3.1.3 Moisture Measurements . . . 69
3.3.1.4 Electrical Resistance Based Sensor System . . . 71
3.3.2 Data-driven Approach for Predicting Moisture Content . . . 73
3.4 Sensor Development and Pre-deployment Evaluation . . . 75
3.5 Field Application for Real-time Measurements of Surface Moisture Conditions 78
3.5.1 Sensor Suite Deployment . . . 78
3.5.2 Field Data Collection and On-site Calibration . . . 80
3.6 Post-deployment Validations of the Moisture Sensor After Long Exposure to Hostile Sewer Condition . . . 81
3.7 Locating the Rebar Orientation using Electrical Resistivity Measurements . 81
3.7.1 Data Collection . . . 81
3.7.2 Spatial Estimation using Gaussian Markov Random Fields . . . 82
3.7.2.1 Gaussian Markov Random Fields . . . 82
3.7.2.2 Spatial Field Model by way of Gaussian Markov Random Fields . . . 83
3.7.2.3 Sensor Data Modelled by GMRF Using SPDE Approach . 84
3.8 Experimental Results . . . 87
3.8.1 Experimental Evaluation to Study the Effects of Concrete Moisture with Electrical Resistance and pH . . . 87
3.8.2 Sensor Development and Pre-deployment Evaluation . . . 90
3.8.3 Field Deployment Application . . . 91
3.8.3.1 Real-time Sensor Data Showing Temporal Dynamics of Surface Resistivity Measurements from the Sewer Pipe . . 92

3.8.3.2 Effects of Concrete Surface Temperature and Sewer Ambient Temperature Conditions . . . 92
3.8.3.3 On-site Calibration and Surface Moisture Interpretations . 92
3.8.4 Post-deployment Validations . . . 95
3.8.4.1 Spatial Estimation of Rebar Using GMRF . . . 97
3.9 Summary . . . 101

4 Smart Predictive Analytics for Detecting Sensor Failure 104
4.1 Introduction . . . 104
4.2 Related Works . . . 107
4.3 Forecasting Temporal Dynamics of Quantified Variables from the Sensing Suite . . . 110
4.3.1 Surface Temperature and Surface Resistivity Data From the Sensing Suite . . . 110
4.3.2 Formulation of Seasonal Autoregressive Integrated Moving Average (SARIMA) Model . . . 111
4.3.3 Automatic Selection of SARIMA Model Parameters . . . 114
4.3.4 Computing Prediction Intervals of the Forecasts at Any Lead Time 114
4.4 SFDA Algorithm . . . 115
4.5 Experimental Evaluation Results . . . 122
4.5.1 Comparative Analysis of Forecasting Models . . . 122
4.5.2 SFDA Algorithm Evaluation: Anomalies and Sensor Failure Detection 127
4.5.3 SFDA Algorithm Evaluation: Forecasting Performance . . . 134
4.5.4 SFDA Algorithm Evaluation: Data Accommodation Process . . . 138
4.6 Summary . . . 141

5 Conclusions 144
5.1 Summary of Contributions . . . 144
5.2 Discussion of Limitations . . . 146
5.3 Implications for the Water Industry . . . 148
5.4 Future Research . . . 149

Bibliography 151

List of Figures

1.1 Multi-sensor robot for condition assessment of sewer infrastructures [1]. . . 2
1.2 Microbial induced corrosion process in concrete sewer assets. 4

2.1 Surface Temperature Sensors (A) Infrared Radiometer Sensor (B) Epoxy coated thermistor sensor 33
2.2 Enclosure testing in sewers. (A) Deploying mechanism of the enclosure (B) Enclosure inside sewer having Hydrogen Sulphide (H_2S) around 5ppm. . . . 34
2.3 Field deployment of a sensor suite at a sewer site for real-time measurements of temperature variables. (A) Installations of the sensing unit at the crown of the sewer pipe for monitoring surface temperature variations (B) Construction of the monitoring unit outside the sewer pipe (C) Housing the monitoring unit using an electrical pillar box having vented air supply. 36
2.4 Assessment of the optical window exposed to different relative humidity conditions inside the humidity chamber. (A) 80% RH (B) 90% RH (C) 100% RH. 41
2.5 Performance efficacy of IRR sensor by positioning it at different incident angles from the surface of interest. 42
2.6 Statistical comparative analysis of IRR sensor measurements obtained in illuminated and dark ambient conditions by positioning the sensor in different distances. 43
2.7 Computed measures of RMSE and MAPE illustrating the IRR sensor performance under different humidity conditions. 44
2.8 Computed measures of RMSE and MAPE illustrating the IRR sensor with varying surface temperature. 45
2.9 Sensor enclosure. (A) New enclosure CAD Model (B) Top-view of the sensor enclosure (C) Front-view of the sensor enclosure. 46
2.10 Surface temperature profiles from IRR sensor and thermistor sensor. 47
2.11 Comparison of surface temperature profile from IRR sensor with the sewer ambient temperature profile from the thermistor sensor. 48
2.12 Comparison of daily average surface temperature profile from IRR sensor with the daily average of ambient temperature outside the sewer pipe. . . . 49
2.13 Sensor enclosure after exposure to hostile sewer conditions. (A) Front view of the sensor enclosure (B) Picture showing the degradation on the germanium optical window (C) Top view of the sensor enclosure. 50

2.14 Improving surface temperature measurements of the IRR sensor between November 2016 and January 2017. 51

3.1 Functional block diagram of the sensor system. 72
3.2 Resistance sensor circuit. 72
3.3 Surface resistivity measurement. (A) Commercial resistivity meter from Proceq (B) Wenner method to measure surface resistivity. 76
3.4 Moisture sensor deployment. (A) Sensing unit near the crown of the concrete sewer pipe (B) Monitoring unit of the access station constructed outside the sewer pipe. 79
3.5 Electrical Resistance vs. Volumetric Moisture Content. 88
3.6 Learned GP model with training data. 88
3.7 GP predictions in 3D. 89
3.8 The behaviour of predicted values corresponding to training data. 89
3.9 The behaviour of predictions vs. measured values (testing data). 90
3.10 (A) Accommodation of resistivity meter inside sensor enclosure CAD model and (B) Sensor enclosure displaying the electrodes of the resistivity meter. . 91
3.11 Surface resistivity profiles obtained from the concrete sewer pipe. 93
3.12 Profiles of surface resistivity, surface temperature and ambient temperature. 94
3.13 Surface moisture profiles obtained from the concrete sewer pipe. 96
3.14 Moisture sensor measurements after long exposure to sewer conditions . . . 97
3.15 Sensor enclosure after exposure to hostile sewer conditions for about three months. (A) Top view of the sensor enclosure displaying the sensor electrodes and (B) Side view of the enclosure displaying the de-colouration occurred during the field evaluation. 98
3.16 Spatial estimation using GMRF by taking resistivity measurements at 0°. . 98
3.17 Spatial estimation using GMRF by taking resistivity measurements at 30°. 99
3.18 Spatial estimation using GMRF by taking resistivity measurements at 45°. 99
3.19 Spatial estimation using GMRF by taking resistivity measurements at 60°. 100
3.20 Spatial estimation using GMRF by taking resistivity measurements at 90°. 100

4.1 Block diagram of hardware redundancy. 107
4.2 Block diagram of analytical redundancy. 108
4.3 Illustration of the sliding window mechanism at time period t. 117
4.4 Illustration of the chi square. 119
4.5 Profile of the training data. 123
4.6 Forecast data profile resulting from the Exponential Smoothing (ETS) model. 124
4.7 Forecast data profile resulting from the TBATS model. 124
4.8 Forecast data profile resulting from the SARIMA model. 125
4.9 Comparison of time series forecasting of sensor data using SARIMA, TBATS and ETS models with the measured sensor data profile. 125
4.10 IRR Sensor: Short-term Evaluation-1 of SFDA algorithm. 129
4.11 IRR Sensor: Short-term Evaluation-2 of SFDA algorithm. 130
4.12 Long-term evaluation of SFDA algorithm. 131
4.13 Moisture Sensor: Short-term Evaluation-1 of SFDA algorithm. 132

4.14 Moisture Sensor: Short-term Evaluation-2 of SFDA algorithm. 133
4.15 Illustration of SARIMA model forecasting performance of surface temperature data. 135
4.16 Illustration of SARIMA model forecasting performance of surface resistivity data. 136
4.17 Illustration of the data accommodation during IRR sensor failure 139
4.18 Illustration of the data accommodation during moisture sensor failure. . . . 140

List of Tables

2.1 Gas-phase temperatures inside confined sewer system. 27
2.2 Feasibility Analysis: Comparison of surface temperature measurement modalities 28
2.3 Specifications of the surface temperature sensors used in this study. 33

3.1 Feasibility: Comparison of surface moisture measurement modalities. 66
3.2 Mass of concrete samples in dry condition. 68
3.3 Mass of concrete samples in wet condition. 68
3.4 Concrete samples in different pH value of solutions. 69
3.5 Depth profile of moisture penetration inside concrete. 70
3.6 Density of concrete samples in dry condition. 70
3.7 Density of pH solution. 71
3.8 Specifications of the resistivity meter. 77

4.1 Statistical Performance Evaluation of Time Series Models. 127
4.2 IRR Sensor: Statistical Evaluation of SFDA Model's Forecasting Performance. 137
4.3 Moisture Sensor: Statistical Evaluation of SFDA Model's Forecasting Performance. 138
4.4 Evaluation of SFDA Model's Data Accommodation Process for IRR Sensor. 141
4.5 Evaluation of SFDA Model's Data Accommodation Process for Moisture Sensor. 141

Acronyms & Abbreviations

1D	One-dimensional
2D	Two-dimensional
3D	Three-dimensional
AC	Alternating Current
AIC	Akaike Information Criterion
AR	Autoregressive
ARMA	Autoregressive Moving Average
ARIMA	Autoregressive Integrated Moving Average
CAS	Centre for Autonomous Systems
CCTV	Closed-circuit television
CW	Critical Wavelength
DC	Direct Current
DTS	Distributed Temperature Sensing
ETS	Exponential Smoothing
FBG	Fiber Bragg Gratings
FDR	Frequency Domain Reflectometry
FG	Fiber Grating

GMRF Gaussian Markov Random Fields

GP Gaussian Process

GPR Gaussian Process Regression

H_2S Hydrogen Sulphide

H_2SO_4 Sulphuric acid

IRR Infrared Radiometer

IRT Infrared Thermography

MA Moving Average

MAE Mean Absolute Error

MAPD Mean Absolute Percentage Deviation

MAPE Mean Absolute Percentage Error

MPE Mean Percentage Error

NTC Negative Temperature Coefficient

RF Radio Frequency

RFs Radio Frequencies

RH Relative Humidity

RMSE Root Mean Square Error

RTD Resistance Temperature Detector

RW Random Walk

SARIMA Seasonal Autoregressive Integrated Moving Average

SDR Successful Detection Rate

SES Simple Exponential Smoothing

SFA Sensor Failure Accommodation

SFDA Sensor Failure Detection and Accommodation

SPDE Stochastic Partial Differential Equations

TDR Time Domain Reflectometry

UTS University of Technology Sydney

Nomenclature

	General Notations
cm	Centimetre (unit).
Dt	Time interval between the two sensor measurements.
df	Degrees of freedom.
mm	Millimetre (unit).
g	Gram (unit).
m_d	Mass of the concrete sample in a dry condition.
m_w	Mass of the concrete sample in a wet condition.
n	Number of Samples.
ppm	Parts per Million (unit).
t	Time (continuous).
V	Voltage (unit).
$^{\circ}C$	Degree Celsius.
μ	Mean.
σ	Standard deviation.
σ^2	Variance.
ρ_d	Density of concrete sample in a dry condition.
ρ_w	Density of pH solution.
θ_G	Wet basis moisture content of a material.
θ_V	Volumetric moisture content of a material.

Sensors

T_{IRR}	Surface temperature measurements from the infrared radiometer sensor.
T_{RIT}	Surface temperature measurements from the reference instrument thermistor sensor.

On-site Calibration of Sensors

E	Measurement error.
E_{ir}	Radiant energy detected by the infrared surface temperature sensor.
E_{tr}	Radiant energy detected by the contact-type surface temperature sensor.
SM	Surface moisture conditions.
SR_S	Surface resistivity value measured from the resistivity meter.
SR_W	Surface resistivity value measured at wet area of the concrete sewer pipe.
SR_D	Surface resistivity value measured at dry area of the concrete sewer pipe.
T_{is}	Temperature measured by the infrared surface temperature sensor.
T_{tr}	Temperature measured by the contact-type surface temperature sensor.
ϵ_{is}	Set emissivity of the infrared sensor.
ϵ_t	True emissivity of the measured surface.
ϵ_{IR}	Set emissivity of the infrared radiometer sensor.
ϵ_T	Estimated emissivity of the surface.
μ	Mean value of ϵ_T.

SFDA Algorithm

$AR(p)$	Autoreggressive model of order p.
$AR(p)_t$	Actual value of $AR(p)$ at time t.
$ARMA(p,q)$	Autoreggressive Moving Average model of order p and q.
$ARMA(p,q)_t$	Actual value of $ARMA(p,q)$ at time t.

$ARIMA(p,d,q)$	Autoreggressive Integrated Moving Average model of order p, d and q.
$ARIMA(p,d,q)_t$	Actual value of $ARIMA(p,d,q)$ at time t.
B	Backshift operator.
d	Parameter governs the level of differencing.
D	Degree of seasonal differencing parameter.
k	Backward observation of the time series.
K_n	Number of parameters estimated to compute one-step ahead forecasts.
L	Maximized likelihood of the $SARIMA(p,d,q)(P,D,Q)_{S_p}$ model.
$MA(q)$	Moving Average model of order q.
$MA(q)_t$	Actual value of $MA(q)$ at time t.
p	Autoregressive model order.
P	Seasonal Autoregressive model order.
q	Moving Average model order.
Q	Seasonal Moving Average model order.
R_t	Observe red sensor data coming from the sewer.
$SARIMA$	$SARIMA(p,d,q)(P,D,Q)_{Sp}$ model with parameters p,d,q,P,D and Q.
S_p	Seasonal period of the stochastic model.
S_{t+f}	Future observable variable.
$\widetilde{S}_{t-n}$	Previous deviations from the mean value of the time series data.
$\hat{S}_{t+f}(+)$	Forecast value resulting from the SARIMA model.
$\hat{S}_{t+f}(+)$	Upper limit of the forecast.
$\hat{S}_{t+f}(-)$	Lower limit of the forecast.
W_L	Size of sliding window
ϕ_n	Finite set of weight parameters of the $AR(p)$.
θ_n	Finite set of weight parameters of the $MA(q)$.
ε_t	Random shock.
$\mu_{\lambda/2}$	Percentiles of the standard normal distribution.
σ_g	Standard deviation of the Gaussian distribution.

χ^2	Pearson's chi-squared test.
χ^2_{df}	Chi-squared distribution.
α	Critical value.

Glossary of Terms

Ambient	Pertains to the immediate surroundings.
Anomalies	Data that deviates from the standard, normal, or expected.
Autonomous	Without human intervention.
Data Accommodation	Utilizing the data coming from the reliable measure, prediction or estimation.
Field Deployment	The transportation of equipment to a place or position for desired operations.
Forecasting	Predict or estimate the future trends or unknown events.
Infrared Radiometer	An instrument for detecting or measuring the intensity of radiation using infrared signals.
Measurements	The action of measuring the physical quantities.
Modelling	A description of a system using mathematical concepts and language. The process of developing a mathematical model is termed mathematical modelling.
Predictive Analytics	A variety of statistical techniques from predictive modelling, machine learning and data mining to predict future trends or unknown events by using historical and transactional data.
Real-time	Relating to a system in which input data is processed within milliseconds so that it is available virtually immediately as feedback to the process from which it is coming.
Relative Humidity	The amount of water vapour present in air expressed as a percentage of the amount needed for saturation at the same temperature.

Resistance	The measure of the degree to which a conductor opposes an electric current through that conductor.
Resistivity	It is a fundamental property that quantifies how strongly a material under test is opposing the flow of electric current.
Robust	Able to withstand or overcome adverse conditions.
Sensing Suite	A set of sensors enclosed in a housing to perform measurements of interest.
Sensor	A device that detects or measures a physical property, indicates or otherwise responds to it.
Sensor Characterization	A description of the distinctive nature or features of the sensor under different condition.
Sensor Failure	The state of improper functioning of a sensor.
Sewers	An underground conduit for carrying off drainage water and waste matter.
Smart	Device programmed so as to be capable of some independent action.
Study	A detailed investigation and analysis of a subject or situation.
Technology	Device or equipment developed from the application of scientific knowledge.
Temporal Dynamics	The properties that changes within a system or process relating to or denoting time.
Quantification	The measurement of the variable of interest.

Chapter 1

Introduction

Robotic systems are no longer in the realm of science fiction. Today, we are witnessing a paradigm shift in scientific advancements that are sliding towards a robotic revolution from the golden era of computers. Curiosity Rover from NASA is a paragon of "How robotic revolution has stretched out its presence from the planet Earth to Mars?". Besides the extraterrestrial life of robots in this day and age, there are several applications where robots can cause technological interventions to achieve the objective of making our planet safer and smarter.

Several pioneering works were accomplished in the past by utilizing the fundamental research areas of robotic science. Currently, the heritage of robotics vividly signifies a proliferating role for mobile robotic systems in the challenging man-made environments. Such emerging trends indicate that scientists are viewing mobile robots as a promising tool to navigate, explore and measure the environmental health of hostile areas, where direct human contact can cause occupational health hazards.

Urban sewerage systems is an ideal example of a man-made hostile environment, where human health and safety can be under threat. Exploiting robotic inspections in such systems not only requires hi-tech robots but also advanced sensing technologies in order to provide credible information about the sewer assets. Therefore, employing robots with robust sensing technologies in high-risk environments can revolutionize the way traditional manual operations are conducted.

FIGURE 1.1: Multi-sensor robot for condition assessment of sewer infrastructures [1].

SewerVue Technology manufactures commercial robots as shown in Figure 1.1 for evaluating the underground pipe conditions of the sewer infrastructures [2]. In such robots, sensors play a crucial role in providing reliable information. However, it is a very challenging problem to develop sensing technologies that can facilitate desired operations under sewer conditions. This dissertation tackles one such problem by developing robust sensor technologies that can yield information about the factors that influence concrete corrosion in the sewer pipes. In the broader context, the developed sensor technologies can be implemented by robots for evaluating the sewer corrosion.

This chapter introduces the research work presented in this dissertation. It commences with an introduction to a background for sewer infrastructures. This background furnishes the historical perspective of sewer corrosion and elaborates on the mechanism involved in the corrosion process of the concrete sewer assets. Following this, the chapter elucidates the research motivation and delineates the statement of the problem with research questions. In addition, the chapter chronicles the principal contributions and enumerates the first published appearances of the described contributions. Finally, the chapter concludes by outlining the structure of the dissertation in order to provide the reader with an overview of the pursued work.

1.1 Hostile Sewer Infrastructures

Urban underground infrastructure like sewer system is an important national property to any country as it allow us to occupy the clean cities of today. However, the notion of having underground sewer systems was historically a part of urban evolution. In fact, archaeological evidence reveals that the sewer systems were constructed in ancient India, China, Greece and Egypt since 1000 AD [3–5]. In that era, sewer systems were used for collecting storm water to irrigate farm lands and discharging sewage. In the early 1900s, few methodological studies presented scientific evidence relating the sewage waste to epidemic diseases. This led to the construction of modern urban sewer systems in Europe during the mid 19^{th} century [4]. Later, the first occurrence of sewer corrosion was noticed in the late 19^{th} century in the USA [6]. However, it was only in the 1940s that the methodological studies conducted in Australia and USA entrenched the biological nature of concrete corrosion [7–9]. Then in the 1980s, a radical increase of concrete corrosion was observed in the sewers of the USA [10] and Europe [11]. Until that time, sewer corrosion was not regarded as a major problem. Increases in sewage temperature due to urbanization factors such as the discharge of household detergents containing sulphur and toxic metals from industries were related to the ascendancy of sewer corrosion in the 1990s [12, 13]. Nowadays, properly planned and managed sewer systems are viewed as a critical infrastructure element in building a sustainable urban society.

Presently, the underground sewer pipes are constructed for thousands of kilometres for servicing various sectors of the community. For instance, in Australia nearly 110,000 kilometres of sewer piping benefits the household and industrial society [15]. In such urban sewer systems, H_2S is mainly produced due to the biological activities of sulphate-reducing bacteria in the rising main sections (pressure pipes) under the anaerobic conditions [16], which is then transported to the gravity flow sections of the sewer [17]. Due to turbulent flow, the dissolved H_2S present in waste water is released to the sewer atmosphere as gaseous H_2S [18], where it is absorbed on the exposed concrete surface, notably on the crown of the sewer pipe. In general, the newly installed concrete possesses surface pH approximately between 12 to 13 [15]. However, when the micro-organisms begin to colonize on the concrete surface the pH falls nearly to 9 [19].

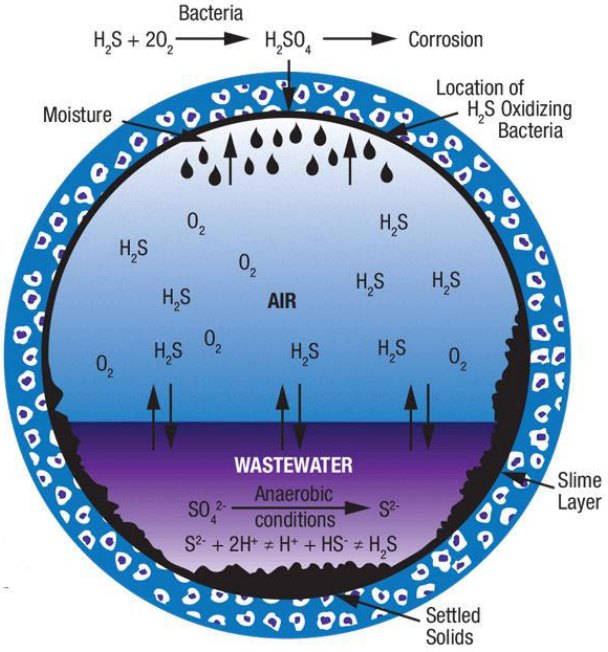

[14]

FIGURE 1.2: Microbial induced corrosion process in concrete sewer assets.

Due to the occurrence of biological oxidation, the absorbed H_2S on the concrete surface is converted into Sulphuric acid (H_2SO_4) by the micro-organisms that dwell on the moist surface of the concrete [20]. The generated biogenic H_2SO_4 penetrates into the pores of the concrete and starts to chemically react with the cement material of the concrete and initiates sewer corrosion [21]. With time and urban growth, the buried concrete sewer pipes are vulnerable to structural deterioration mostly due to the physical and biological process known as microbial induced corrosion [17]. Figure 1.2 illustrates the chemical reaction of microbial induced concrete corrosion in the sewer pipe. The nature of atmospheric conditions inside the sewer system makes the infrastructure a hostile environment.

To address the corrosion problem emanating from the concrete sewer, the water utilities invest in research and development to endeavour sensing technologies that can provide vital information about corrosion. This dissertation originated as a part of Activity 1c of the project on "Data Analytics on Sewers" funded by Sydney Water, Melbourne Water, South Australian Water and Water Corporation (Western Australia). The research organisations include Data61-Commonwealth Scientific and Industrial Research Organisation (CSIRO), The University of Newcastle and University of Technology Sydney.

1.2 Research Motivation

Public Health and Safety: Urban sewerage systems transporting domestic and industrial waste water through underground pipelines have been widely regarded as an imperative infrastructure asset of our public society mainly for the reason that they conserve our civic communities from the menace of sewage-borne diseases, abhorrent odours and unhygienic conditions [22]. However, such infrastructure systems undergo severe H_2S induced corrosion of reinforced concrete sewer pipes particularly in warm climatic countries like Australia. As the sewer concrete corrosion escalates gradually, the structural health of the sewer infrastructure is seriously affected and this leads to sewer pipe deterioration and consequential structural failures. Practising preventive measures such as proper maintenance and timely interventions of such critical sewer infrastructures can thwart the threats posed to nearby residents and surrounding environments due to potential catastrophic events like the structural breakdown of sewer pipes.

Economy: On a global scale, the sewer corrosion causes governments and water utilities a major problem as they incur losses that are estimated to be billions of dollars every year [23]. The value of sewer infrastructure assets in USA and Australia are estimated to be over $1 trillion and $100 billion respectively [24]. This is nearly equivalent to 7% of USA's and 6% of Australia's gross domestic product as of 2016. Failure to maintain such infrastructures will lead the utilities and governments to a range of economic repercussions. For example, the sewer assets are degrading at an estimated annual cost of $13.75 billion in USA [25], $50 billion in Germany [26] and $100 million in Australia [19]. The cost related to the loss of sewer infrastructure is expected to increase as the failure of critical sewer pipes continues [20]. Therefore, the concrete corrosion in sewer systems is regarded as a paramount problem to water utilities around the globe.

Technology: One of the direct measures to address the sewer corrosion problem is to measure the amount of concrete corrosion itself. However, there is no reliable, robust and efficient technology in the state-of-the-art systems to measure this quantity throughout the network. Then, the obvious choice is to seek the quantifiable proxies of concrete corrosion. In this sense, a good proxy could be the surface acid levels. However, there is no proficient long-term measuring technique available for quantifying the surface acid

levels in the sewer system. So, the micro-organisms that are responsible for producing biogenic H_2SO_4 on the concrete surface could be the next level of proxy measure. Adversely, this proxy measurement is an intricate process involving the tedious task to identify the liable bacterial species from other micro-organisms that reside on the sewer pipe. Currently, there is no appropriate technology available for in-sewer application to measure bacterial types that account for concrete corrosion. Then, the researchers have focussed on investigating the attributes that could be quantifiable to estimate the presence of bacteria. In this regard, living conditions for bacteria such as food (H_2S), comfortable temperature (sewer surface temperature) and moist environment (sewer surface moisture) were recognized as the key contributing factors for the growth of bacteria in sewer pipes [19, 27]. Presently, there is an industry-proven commercial system to monitor H_2S levels in sewer systems [28]. However, there are no proven technologies available in the market to quantify surface temperature and surface moisture in the sewer system. The non-existence of such technologies leads to adopting another level of proxies. For this reason, the gas-phase temperature of the sewer air and relative humidity of the sewer air were adopted. There is technology available to measure air temperature inside sewer pipes in a reasonable and robust way. The relative humidity of sewer air can be measured, but the sensors have proven to be of short-term use only as they become non-functional under harsh sewer conditions in a short period of time. There are current developments in the fiber optics sensing technology [29], which may be a feasible option in the future.

In order to effectively manage the sewer infrastructure, the scope for innovative sensing technologies and physical data interpretations has become the need of the hour for the governments and water utilities to comprehend the elements that leverage sewer concrete corrosion. For that reason, the sewer managing bodies are looking forward to an ingenious solution by utilizing smart sensing technology and predictive analytics for reinforcing the present sewer monitoring capabilities by providing pivotal information about the sewer concrete corrosion. Therefore, public health and safety, economy and technology will be the influential factors of motivation for the research problem detailed in the next section.

1.3 Statement of the Problem

Research studies over the years have attained several landmarks on sewer concrete corrosion modelling by using observations like ambient temperature, relative humidity and H_2S levels of the sewer atmosphere [15, 30–33]. Recently, a first pass model for predicting the rate of sewer concrete corrosion and service life of the pipe was formulated by [27], where the model conceptualizes the functional relationship between the corrosion and observations.

The predictive model is of the form as in Equation 1.1:

$$C = A \times [H_2S]^{0.5} \times \frac{0.1602H - 0.1355}{1 - 0.9770H} \times e^{(-45000/RT)} \tag{1.1}$$

where C is the rate of concrete corrosion in sewer pipe (mm year^{-1}), A is the value of the scaling constant (= 207750 mm year^{-1} ppm$^{-0.5}$), H_2S is the concentration of hydrogen sulphide present in the sewer atmosphere (ppm), H is the relative humidity of the sewer air (%), T is the ambient temperature of the sewer air (Kelvin) and R is the universal gas constant (= 8.314 J mol^{-1} K^{-1}).

Despite the model in Equation 1.1 progressing towards conceivable results for corrosion prediction, there is still a large proportion of uncertainty associated with the model prediction. This is primarily due to the reason that the accurate prediction of corrosion across the sewer network is often hampered because of inherent scattering of data or insufficient observations [31, 34], a problem that is commonly referred as "sparsity" in data analytics.

Based on the theory proposed by [27], higher relative humidity levels in the sewer atmosphere does not necessary imply higher moisture conditions on the pores of the exposed concrete surface. For example, 90% of relative humidity is approximately equivalent to 10% of saturated moisture level on the concrete surface. In addition, in locations where the sewer pipe is above the ground level, the surface temperature near the crown can be intermittently distinctive to the temperature of the sewer atmosphere mainly due to the degree of moisture condensation that occurs within the concrete pore

structure. Therefore, the gas-phase temperature of the sewer air and relative humidity of the sewer air are not the representative measures to that of sewer wall moisture and temperature. However, the predictive model in Equation 1.1 uses relative humidity and temperature of the sewer air as observatory variables.

In the contemplation of ameliorating the existing sewer corrosion predictive models with regard to the described statement of the research problem, there arise the following research questions:

1. **Research Question-1:**

   How to quantify the temporal dynamics of surface temperature conditions of the sewer pipes without altering the concrete surface properties under hostile sewer environment?

2. **Research Question-2:**

   How to determine the surface moisture conditions of the concrete sewer pipe without damaging the exposed surface during measurements and will the sensor survive the hostile conditions during long-term monitoring?

3. **Research Question-3:**

   Assuming the fact that there are technologies available to quantify surface temperature and moisture conditions inside sewer pipes, in this scenario, how to automatically determine the measurements from the sensor are reliable and what will happen to the temporal data supplied to the corrosion predicting models in the event of sensor malfunction or scheduled maintenance?

Albeit the fact that existing researchers have focused on measuring different variables in the sewer systems, it is to be noted that there have been no reports in the scientific literatures about the non-invasive measurements of surface temperature and surface moisture conditions of the concrete sewer pipes inside the perilous environmental conditions of the sewer system.

1.4 Principal Contributions

In accordance with the research questions stated in the previous section, this dissertation has developed the new sensor technologies to measure the actual surface temperature and moisture conditions of concrete sewer pipes. The outcomes achieved thus far include:

"*Developed a sensing Proof of Concept System (including the development of hardware, algorithms and electronics by using commercial sensors) that was successfully evaluated in laboratory and in field conditions (e.g. Sydney Water sewer site, Thornleigh suburb of Sydney city, Australia) for 96 days.*"

In this context, this dissertation has led to the following principal contributions in the field of sensor technologies.

1. **Developed a robust sensor technology for measuring surface temperature dynamics inside concrete sewer pipes.**

   Proven and validated infrared radiometer sensor with an antifog coated germanium optical window can be used for non-contact surface temperature measurements in sewer systems. The developed sensor technology is more robust and reliable for deployment in harsh corrosive sewer conditions. It operated for three months without maintenance and can be used on moving platforms. In pursuance of providing more accurate measurements, an in-situ field calibration technique was adopted by determining emissivity value of the sewer concrete surface. These emissivity coefficients of the sewer concrete surface were used to calibrate temperature measurements under real-world conditions.

2. **Developed a robust sensor technology for determining surface moisture conditions inside concrete sewer pipes.**

   Proven and validated electrical resistivity based moisture sensing on the exposed surface of the concrete sewer is feasible using on-site calibration to mitigate the effects of metals (reinforcing bar) in order to provide reliable measurements of surface moisture conditions. This sensing system measures surface moisture, without changing the concrete surface conditions. In addition, a technique for

optimal placement of a sensor on the concrete surface for measurements was proposed.

3. **Developed a machine learning based diagnostic toolkit for detecting early sensor failure.**

   Developed sensing system incorporating smart predictive analytics to intelligently identify sensor failure or unreliable data to prevent the occurrence of false positive or negative results. The predictive algorithm of the toolkit embraces forecasting model with statistical hypothesis techniques. The salient features of the algorithm include: (i) Enabling temporal forecasting of sensor data, (ii) Identifying and isolating anomalies in a continuous stream of sensor data, (iii) Detecting early sensor failure and (iv) Providing reliable estimates of sensor data in the event of sensor failures or during the scheduled maintenance period of sewer monitoring systems. This algorithm was evaluated with the surface temperature and surface moisture data sourced from the instrumented sewer infrastructure.

1.5 First Published Appearances of the Described Contributions

Most of the contributions described in this dissertation have first appeared as the following publications.

1.5.1 Journals

1. **K.Thiyagarajan**, S. Kodagoda, R. Ranasinghe, D. Vitanage and G. Iori, "Robust sensing suite for measuring temporal dynamics of surface temperature in sewers," Nature - Scientific Reports. *(Under Review)*

2. **K.Thiyagarajan**, S. Kodagoda, R. Ranasinghe, D. Vitanage and G. Iori, "Robust sensing system for non-invasive estimation of surface moisture conditions in concrete sewers," Nature - Scientific Reports. *(Under Review)*

3. **K.Thiyagarajan**, S. Kodagoda, L.V. Nguyen, and R. Ranasinghe, "Sensor Failure Detection and Faulty Data Accommodation Approach for Instrumented Wastewater Infrastructures", IEEE Access. *(Under Review)*

1.5.2 Conference Proceedings

1. **K.Thiyagarajan**, S. Kodagoda, L.V. Nguyen, and S. Wickramanayake, "Gaussian Markov Random Fields for Localizing the Reinforcing Bars in Concrete Infrastructures," 35^{th} International Symposium on Automation and Robotics in Construction (ISARC), Berlin, Germany, 2018. pp. 1035-1041.

2. **K.Thiyagarajan**, S. Kodagoda, and L.V. Nguyen, "Predictive Analytics for Detecting Sensor Failure Using Autoregressive Integrated Moving Average Model," 2017 IEEE 12^{th} Conference on Industrial Electronics and Applications (ICIEA), Siem Reap, Cambodia, 2017, pp. 1923-1928.

3. **K.Thiyagarajan**, S. Kodagoda and J. K. Alvarez, "An instrumentation system for smart monitoring of surface temperature," 2016 14^{th} International Conference on Control, Automation, Robotics and Vision (ICARCV), Phuket, Thailand, 2016, pp. 1-6.

4. **K.Thiyagarajan**, S. Kodagoda and N. Ulapane, "Data-driven machine learning approach for predicting volumetric moisture content of concrete using resistance sensor measurements," 2016 IEEE 11^{th} Conference on Industrial Electronics and Applications (ICIEA), Hefei, China, 2016, pp. 1288-1293.

1.5.3 Technical Reports

1. S. Kodagoda, R. Ranasinghe, **K.Thiyagarajan**, G. Dissanayake, "Predictive Analytics for Sewer Corrosion - Final Report". Pages: 1-18, 2017.

2. S. Kodagoda, R. Ranasinghe, **K.Thiyagarajan**, J. K. Alvarez and G. Dissanayake, "Sensors for Surface Temperature and Surface Moisture Measurements - Scoping Study". Pages: 1-35, 2016.

1.6 The Structure of the Dissertation

The remainder of this dissertation is structured as follows:

Chapter 2: This chapter will enumerate the development of a robust sensor technology using an infrared radiometer for non-invasively measuring the surface temperature of concrete sewer pipe inside hostile sewer conditions.

Chapter 3: This chapter will elucidate a non-invasive sensing technique for determining the surface moisture conditions of the concrete sewer pipes based on the surface electrical resistivity measurements.

Chapter 4: This chapter will present a smart predictive analytic framework by combining forecasting model and statistical diagnostic method for detecting early sensor failure in the instrumented sewer infrastructure.

Chapter 5: Finally, this chapter will present a summary of conclusions drawn from the proposed sensor technologies and smart predictive analytics whilst discussing the limitations of the proposed work together with the implications for water industry and future prospects.

Chapter 2

Robust Sensor Technology for Measuring Surface Temperature in Sewers

2.1 Introduction

Robust sensor technologies have become a promising element of tomorrow's smart infrastructures. This is due to their capabilities to enable intelligence and cater reliable measures of critical variables. Integral to the robotics revolution and smart systems, the dominance of sensors has inclined to decipher the dynamics of measurand in several infrastructure monitoring applications. The data obtained from the sensors are utilized to ascertain the real behaviour of infrastructure assets and in addition, they answers to resolve the scale of threats by calling on the amalgamation of smart sensing technology and data analytics. This chapter focusses on the development of a robust sensor technology for measuring temporal dynamics of surface temperature in hostile sewer environments.

The confined sewer pipes are subjected to thermal effects due to interactions with both internal ambient conditions and external atmospheric conditions. As the sewer ambient temperature changes over time, the sewer surface may not come to an equilibrium with

the ambient temperature. Therefore, the sewer walls can potentially have a slightly different temperature to that of the ambient gas temperature. The distribution of the surface temperature on sewer pipes inner walls is affected by many factors such as ambient temperature, air flow, humidity, fluid flow rate and effluent temperature. Therefore, it is important to measure the surface temperature at different locations in sewers to correctly estimate the surface temperature distribution of the sewer wall.

Recent studies have shown the feasibility of measuring different temperature variables in the sewer systems. For example, the gaseous temperature of sewer air was measured inside the corroded sewer pipes in different cities of Australia [19, 27]. Similarly, the effluent temperature and ambient temperature of the sewers were measured in two sewer manholes of the Kent city in England and thereby observed that on average effluent temperature is higher by 3.5°C [35]. A considerable amount of research was performed using Distributed Temperature Sensing (DTS) technology, which utilizes fibre optic cables for measuring the wastewater temperatures in sewer networks [36, 37]. The use of DTS technology has been demonstrated in the application of measuring temperature gradients at different positions of the sewer pipe by placing the fibre optic cable near soffit (top), wastewater level (floating) and invert (bottom) [38]. Although researchers have focused on measuring different temperature variables in the sewer, there have been no reports in the scientific literature about the measurement of concrete surface temperature in sewers. As the sewer corrosion is dependent on the surface temperature variable, the water utilities are looking forward to a sensor technology for measuring the surface temperature at the crown of the sewer pipe inside the confined sewers.

In this chapter of the dissertation, the possibility of measuring surface wall temperature is studied. The surface temperature is a better proxy that can add value to the current development of corrosion modelling and data analytics. Therefore, it is important to develop a surface temperature monitoring suite that can readily perform measurements under the aggressive environmental conditions of the sewers as the temperature data of the concrete surface is necessary to predict the rate of sewer concrete corrosion. However, the sewers are classified as Zone-2 hazardous areas in Australia [39]. So, there are multifarious requirements to be considered in developing a sensor suite as there are no commercial sensor systems proven to be sewer deployable and comply with the

requirements specified by the sewer operators. In the light of the preceding discussion, the sensor suite should possess low maintenance and convenient access to the monitoring data, easily deployable and removable, non-destructive measurements on the concrete surface at regular frequencies, integrated multi-sensor package to accommodate different sensors and finally to sustain in harsh sewer conditions. In order to accomplish it, several laboratory studies were conducted to recognize radiometry based surface temperature measurements as a potential option to address the key challenges emerging from the sewer environments [39–41].

This chapter first reports the scoping study conducted to identify the potential sensors that can perform surface temperature measurements in the aggressive sewer conditions. Then, the chapter elucidates the characterization of the IRR sensor in laboratory conditions. In the IRR sensor characterization, the performance of optical window, the effects of incident angle, limit of detection, distance, lighting condition, reproducibility, humidity conditions, varying surface temperature conditions were investigated. Thereafter, the sensor was deployed in the sewers for evaluating the long-term sensing performance and endurance of the sensor package. The measurements from a non-contact type IRR sensor was examined with the measurements from a contact-type thermistor sensor to furnish a scientific evidence for supporting the application of non-contact surface temperature sensing in the sewer. In addition, the quantifications of ambient temperature in-situ and ex-situ of the sewer pipe were compared and analysed with the measurements resulting from the IRR sensor. After successfully completing the field trial campaign, the sensor suite was brought to the laboratory for post-deployment validation. Further, the measurements from IRR sensor data was improved by calibrating the sensor based on the emissivity coefficient of sewer concrete surface. To the best of author's knowledge, this is the first ever research work that investigates the feasibility of monitoring non-contact surface temperature in the hostile sewer environment with a motive of augmenting the present development of corrosion modelling.

The remainder of this chapter is organised as follows: Section 2.2 presents the scoping study of sensors for surface temperature measurements. Section 2.3 details the methods adopted for sensor characterization in laboratory conditions. Section 2.4 describes the sensor deployment for monitoring the temporal dynamics of surface temperature. Section

2.5 presents the post-deployment investigations. Section 2.6 presents the theoretical consideration for determining the emissivity co-efficient for the measured surface temperature. Section 2.7 presents the experimental results and analyses and finally, Section 2.8 summarizes the main contribution resulting from this chapter with research outcomes.

2.2 Scoping Study: Sensors for Surface Temperature Measurements

This scoping study of sensors for surface temperature measurements investigates a wide range of temperature measurement techniques with the aim of selecting a practically feasible sensor that can potentially be used in sewers.

2.2.1 Sensors for Surface Temperature Measurements

This section covers the review of relevant literatures about the technologies that are associated with the motivation of this research work for measuring surface temperature. Although the temperature can be measured using a wide variety of sensors they all infer temperatures by sensing some change in physical characteristics. Considering this, temperature measurement instruments can be broadly classified into the following types.

1. Fluid expansion type temperature measurement devices
2. Bimetallic temperature measurement devices
3. Resistive temperature measurement devices
4. Thermocouple sensors
5. Thermistors
6. Infrared temperature measurement device
7. Fiber optic type temperature measurement devices
8. Distributed Temperature Sensing

2.2.1.1 Fluid Expansion Type Temperature Measurement Devices

Glass thermometers are well-known fluid expansion type devices that are very common in households to measure body temperature. This is the oldest method to measure temperature or a temperature gradient.

Technology: The fluid expansion based temperature measurement technology works on the principle based on the tendency of volumetric change of matter with respect to change in temperature [42]. They usually come in two main classifications: the mercury type and the organic-liquid type. In these thermometers, a liquid is encased in a narrow glass tube. They have two important parts: a temperature sensor in which some physical change occurs with temperature and some means of converting this sensed physical change into a human readable value.

Discussion: Fluid-expansion sensors do not require electric power and do not pose explosion hazards. The behavior of these temperature sensors is stable even after repeated cycles. However, they suffer from low accuracy and slow response time. There are commercially available sensor types, which utilize organic liquids and gases for expansion based temperature measurements. Stream traps are an ideal example that displays the functionality of these sensor labels. Each of these labels that are attached on the traps contains a white dot, which turns black indicating the change in temperature above a specific point. However, this method has a low response time. So, they do not respond to transient temperature changes.

2.2.1.2 Bimetallic Temperature Measurement Devices

The bimetallic temperature measurement devices are more rugged and low-cost measuring devices compared to the glass thermometers. However, the accuracy of the measurement is comparatively inferior. These bimetallic measurement devices are suitable for many industrial applications where it is sufficient to know what is the temperature of a fluid or device to within a few degrees.

Technology: Bimetallic devices take advantage of the difference in the rate of thermal expansion between different metals. These are constructed using two metal strips bonded

together. When heated, one side expands more than the other, and the resulting bending is translated into a temperature reading by pointing to a temperature indicator [43].

Discussion: These devices are portable and they do not require a power supply to operate. However, they are usually not as accurate as thermocouples or resistive temperature measurement devices. This issue makes the bimetallic temperature measurement devices less suitable for the intended application.

2.2.1.3 Resistive Temperature Measurement Devices

This group of temperature measurement devices includes Resistance Temperature Detector (RTD). A RTD is a temperature sensor that can be used to determine the temperature by measuring the resistance of an electrical wire. These RTD sensors are commonly used in industrial applications that require high accuracy.

Technology: The operating principle of the RTD sensor is based on the change of electrical resistance as a result of a change in temperature [44]. It is called resistance-temperature characteristics. This positive correlation between resistance and temperature is highly predictable, allowing for accurate and consistent temperature measurements. It is actually the inverse of a metals resistivity, that resulted in the development of RTD sensors. Metals are conductive materials and each metal has a specific and unique resistivity that can be determined experimentally. In theory, any metal could be used to measure temperature. However, the metal selected should have a high melting point and an ability to withstand the effects of corrosion. The metal wires that are widely used in RTD sensors are made of materials such as Copper, Nickel and Platinum. Platinum is the most preferred metal for RTD sensors as it has desirable characteristics such as chemical stability, availability in the pure form, and electrical properties that are highly reproducible.

Discussion: The RTD sensors are typically resistive to corrosion while providing more repeatability and stability than their counterparts. With the added repeatability, stability, and accuracy at lower temperatures, the RTD sensors are more prevalent in applications that remain below 600°C.

2.2.1.4 Thermocouple Sensors

The thermocouple is an extensively used thermoelectric sensor for measuring temperature due to its simplicity and cost-effectiveness. They are known for versatility as temperature sensors and hence they are commonly used in a wide range of applications. These are contact type sensors.

Technology: A thermocouple consists of two dissimilar metallic conductors that are coupled to make an electrical junction (measurement junction). This is extended to the reference junction (of a known temperature). The temperature difference between the measurement junction and the reference junction is detected by measuring the change in voltage (electromotive force) at the reference junction [45]. This voltage varies with the temperature difference between the junctions. The temperature of the measurement junction can be calculated based on the knowledge of the temperature at the reference junction. Among the different types of thermocouples, Nickel based K-type thermocouples exhibit high corrosion resistances, good linearity to the measurement of temperature and good resistance against oxidation. There are many applications that can be found in using thermocouples. For example, they were used to monitor ambient temperature in data centers [46] and they were used in a matrix structure to sense the temperature at different locations [47].

Discussion: Thermocouples are generally low-cost and robust as they do not have any moving parts. They can cover a wide temperature range and can operate in harsh environments. However, it has low sensitivity. The accuracy of thermocouples is typically not better than 0.5°C. Moreover the accuracy of thermocouples decreases over time due to changes in the electrical and chemical properties. The technology relies on an accurate reference point to obtain the absolute temperature measurement.

2.2.1.5 Thermistors

A thermistor is a quite commonly used temperature-sensing element composed of a temperature dependent resistor. In this device, the resistance of the material changes with varying temperatures. Thus the temperature can be predicted by using the

variations of the resistance. Thermistors usually have negative temperature coefficients, which means the resistance of the thermistor decreases as the temperature increases.

Technology: Thermistors are made of ceramic semiconductor materials with a resistivity that is especially sensitive to temperature [48]. However, unlike most other resistive devices, the resistance of a thermistor decreases with increasing temperature. This is due to the properties of the semiconductor material that the thermistor is made from. These are known as Negative Temperature Coefficient (NTC) thermistors. There are several forms of commercially available thermistors: discs, beads, rods, washers, and flakes. They utilize resistance as a function of temperature for a typical thermistor. In general, for thermistors, the resistance-temperature curve will have a sharp drop of resistance (say from 100kΩ) to a very small value at a range around room temperature. Therefore, the sensitivity of this device near room temperature measurements is very high. There are positive temperature coefficient thermistors as well. As the name suggests when temperature increases, the resistance of the material increases, and when temperature decreases, the resistance of the material decreases. This type of thermistor is usually used as fuses.

Discussion: The use of thermistors has grown rapidly over the past few years and thermistors are now used in a wide variety of industries. They are even used in the medical instrumentation industry, in clinical laboratories, and in other biomedical applications where they play a critical role in crucially important diagnostic procedures. Thermistors have better accuracy than RTDs and thermocouples. They are small, inexpensive, rugged and reliable. Most importantly, they respond quickly to temperature changes. Furthermore, the high sensitivity of thermistors makes it possible to measure small changes in temperature. Thermistors are easy to use, inexpensive, sturdy, and respond predictably to changes in temperature. While they do not work well with extremely hot or cold temperatures, they are the sensor of choice for many applications that measure the temperature at the desired base point. They are ideal when very precise temperatures are required. These characteristics make thermistors a strong candidate technology to monitor the sewer surface temperature.

2.2.1.6 Infrared Temperature Measurement Devices

There are several technologies based on infrared radiometry. These technologies use devices to capture electromagnetic radiation with longer wavelengths than those of visible light.

Infrared Thermography Infrared Thermography (IRT) is a science dedicated to the acquisition and processing of thermal information from non-contact measurement devices known as the thermal imager or IR camera [49]. An IR camera detects the infrared radiation (heat) that is emitted by an object. This technology allows operators to validate normal operations and, more importantly, locate thermal anomalies (abnormal patterns of heat invisible to the eye) which indicate possible faults, defects or in efficiencies within a system or machine asset. This is a reliable technology and has gained attraction in commercial applications due in large part to the advancement of IR cameras and the considerable reduction of their cost.

Infrared Thermography - Technology: A thermal imaging camera used in IRT detects infrared energy emitted from an object and converts it to an image called thermogram that shows the variation of temperature differences. The concept of infrared thermography is simple. Any object at a temperature above absolute zero (i.e. $T > 0K$) emits infrared radiation [50]. Infrared emissions are invisible to the human eye. Thus, a special instrumentation known as a thermal imager is required to acquire and process these infrared temperature signatures that lie beyond the range of visible light [51]. These cameras simply see the heat that is emitted from the surface of the object that it is viewing. Thermal cameras can usually detect radiation in the far or long wave IR region from 7-14 microns of the electromagnetic spectrum and produce images of that radiation. The thermogram represents the apparent thermal patterns across the surface of the object being inspected. In thermal images, warm objects stand out well against cooler backgrounds; humans and other warm-blooded animals may become easily visible against the environment. The intensity of the infrared radiation emitted by objects is mainly a function of their temperature. This allows thermograms to show variations in surface temperature.

Infrared Thermography - Discussion: IRT is a mature, fast, clean and safe non-contact type technology that is used in a wide variety of applications. These include

detecting problems in building systems and structures, including moisture intrusion, missing or damaged insulation, overloaded circuits, faulty wiring, loose electrical connections, construction defects, water infiltration into building side-walls and storm damage.

IRT has many advantages over other technologies. In general, the salient features include:

1. IRT is a non-contact technology. The devices used are not in contact with the source of heat. In this way, the temperature of extremely hot objects or dangerous products, such as acids, can be measured safely, keeping the user out of danger.

2. IRT provides two-dimensional thermal images, which makes a comparison between different areas of the target possible.

3. IRT provides real-time measurements, which enables not only high-speed scanning of stationary targets, but also acquisition from fast-moving targets and from fast-changing thermal patterns.

4. IRT has none of the harmful radiation effects of other technologies, such as X-ray imaging. Thus, it is suitable for prolonged and repeated use.

5. IRT is a non-invasive technique. Thus, it does not intrude upon or affect the target in any way.

Even though IRT provides 2D thermal images, an enhanced method for monitoring surface temperature in 3D was reported by [52]. In this work, the image from the thermal camera is fused with a depth image acquired through a Kinect camera to produce 3D depth image representing surface temperature variations. There is a variety of limitations of IRT technology that need to be taken into account. Firstly, it is still an expensive option. It may be affected by the instrument and by the environment. These problems can be minimized, but only with adequate setup and testing procedures, which mostly depend on the operators skill. This technology has further limitations to be used in sewer conditions. Specifically, it needs to be protected from corrosive substances, which can be achieved by an enclosure. However, the enclosure needs to be designed to have a thermal ray passing window that does not fog in extremely high humidity conditions. In the case of fogging,

the sensor measures the temperature of the fogged surface rather than the other surface of interest.

Infrared Thermopile Array: Infrared thermopile array is a serially interconnected array of thermocouples, which detects radiant heat emitted by infrared sources in the wavelength range of $2\mu m$ to $22\mu m$ and based on the spectral response, the surface temperatures are measured. They are relatively cheap and effective in temperature measurements by placing in close proximity to the surface of interest.

Infrared Thermopile Array - Technology: Infrared thermopile array is a type of thermal detector which has an absorption layer that absorbs and converts the light into heat and generates an electrical signal representing the change in absorption layer temperature [53]. Thermal detectors respond to any radiation wavelength that is absorbed and can be made to respond over a wide range of wavelengths. Each of the thermocouple in thermopile array consists of two dissimilar materials with a large thermoelectric power and opposite polarities. The thermocouples are placed across the hot and cold regions of a structure and the hot junctions are thermally isolated from the cold junctions. In the hot region, there is a black body for absorbing the infrared, which raises the temperature according to the intensity of the incident infrared [54].

Infrared Thermopile Array - Discussion: These are non-contact type low-cost and durable temperature measurement sensors. These can operate at room temperature. Gas analysis, process temperature monitoring, fire and flame detection, household appliances and explosion detection are some of the applications where infrared thermopile arrays are commonly used. This technology has not yet been reported for using in sewers. As the sensor is dependent on infrared rays, it has similar fogging related issues to that of infrared thermography in high humid environments.

Infrared Radiometers: Infrared radiometers are sensors that measure infrared radiation, which is used to compute surface temperature without touching the surface [55]. This is a non-intrusive type sensor which does not alter the surface temperature during measurement. Infrared radiometer sensors that are commercially available in the market measure the target temperature even at a distance of 2m with great accuracy. An infrared radiometer device senses the gradient of surface temperature based on the

principle of measuring the radiant flux of the electromagnetic radiation between $8\mu m$ $14\mu m$. There are many applications to this sensor including agriculture, meteorology and hydrology.

Infrared Radiometers - Technology: This remote sensing instrument is a passive measuring sensor. That means the sensor can detect natural energy (radiation) which is emitted or reflected by an object or scene being observed [56]. Reflected sunlight is the most common source of radiation measured by passive sensors. It quantitatively measures the intensity of electromagnetic radiation in the infrared band.

Apogee Radiometer is a reliable and sturdy commercially available Infrared radiometer sensor [57]. The Apogee sensor consists of a thermopile, which measures the surface temperature, and a thermistor, which measures sensor body temperature. The thermistor measurement is used with the Stefan-Boltzmann equation to correct for the effect of sensor body temperature on the target temperature. The two temperature sensors are housed in a rugged aluminium body that contains a germanium window.

Infrared Radiometers - Discussion: The radiometer sensor is a non-contact type sensor, which can operate in outdoor conditions. There are many reported agricultural applications to this sensor although it is not reported for use in sewers. Due to the sensor characteristics, it can operate in 100% humid environments; however, condensation can affect the sensor readings. Although this is a promising sensor for sewer applications, the issue of condensation at high humid environments remains a challenge.

2.2.1.7 Fiber Optic Type Temperature Measurement Device

In the previous subsections, the most prevalent technologies used to take temperature measurements such as thermocouples, RTDs and thermistors were presented. While these technologies have been and will continue to be the most economical solutions for most of the temperature sensing applications, fiber optic based temperature sensing has gained attention as an important alternative particularly in harsh environments. Unlike the traditional temperature sensors, fiber optic based temperature sensors are immune to

electromagnetic interference, making the temperature measurement sensors robust and accurate in high Radio Frequency (RF) environments.

Technology: Fiber optic based temperature sensing uses properties of light to measure the temperature [58]. There are three common principles of fiber optic temperature measurement sensors: (a) Fiber Bragg Gratings (FBG) (b) Raman Scattering (c) Interferometry. The FBG is a series of localized changes in the refractive index in the core of the glass fiber. As the temperature changes, the FBG expands or contracts so does the gap between the gratings. This, in turn, affects the refraction index. The change in the refraction index is measured and the shift in wavelength can be converted to a temperature value [59]. In the Raman scattering, when a pulse of light enters the fiber optic cable, most of the light bounces back (i.e back-scatter light) without changing the original wavelength. However, a small amount of the original light is subjected to a few changes through several mechanisms. Raman scattering, the change of the wavelength of the original light source due to molecular vibrations is one such mechanism. Raman Scatter is thermally influenced by temperature as the molecular vibration is sensitive to the temperature, Therefore the amplitude of the scattered light is directly related to the intensity of the thermal excitation and hence the temperature [60]. Fiber optic interferometry can be broadly explained as a technique that utilizes the fundamental principles of optical signal interference to measure a physical property such as temperature. Here two or more light beams are superimposed to measure the phase difference between them. Interferometer utilizes two light beams with the same frequency. Typically an incident light beam of the interferometer is split into two or more parts and then recombined together to create an interference pattern [61].

Discussion: This is a completely passive method, which is immune to electromagnetic interference. These type of sensors can be used in high temperatures and chemically reactive environments. These sensors can also be used to measure the temperature of remote locations. This is, however, a relatively expensive technology and the deployment of fiber optic cables needs changes to the infrastructure.

2.2.1.8 Distributed Temperature Sensing

The Distributed Temperature Sensing (DTS) system is an optical fiber based technology to monitor temperature in a distributed manner based on the Raman scatter principle. DTS system can provide a continuous temperature profile along the fiber optic cable. This technology has been used in a wide range of applications such as smart grids, building infrastructure, oil and gas industry, temperature monitoring in tunnels and waste water systems [37, 38, 62].

Technology: DTS utilizes a laser light to measure temperature along the entire length of the optical fiber cable. Changes in quantities like temperature, pressure and strain can affect the internal structure of the fiber optic sensor changing the way light travels in the fiber. The technology can measure temperature every meter over the fiber cables over a long distance. As discussed in the previous section the basic operating principle of DTS is the Raman scattering. As the light pulse scatters down the fiber optic cable, it produces signals with a longer wavelengths (i.e. stokes signal) and signals with a shorter wavelength (anti-stokes). Both these signals are shifted from the original laser light signal. The temperature is determined by measuring the respective intensities of the stokes and the anti-stokes signals [63]. Additionally, the location of the temperature reading is determined by measuring the time taken for the back-scatter to return to the light source.

Discussion: In order to measure the surface temperature of the sewer crown, the fiber optic cables need to be installed in a way such that they touch the surface. Even though the DTS generates accurate measurements, installing the fiber optic cables along sewer networks requires distributed changes to the infrastructure which may be economically unattractive. Although DTS systems can provide a high resolution temperature profile over a long distance, comparable results may be achieved by combining low-cost sparse temperature measurements with modern day advanced data analytic techniques.

2.2.2 Feasibility

This section indicates the feasibility aspects of the sensing devices to be used to measure surface temperature in the sewer system. In this regard, firstly, this section presents the

atmospheric temperature conditions inside the Australian sewers. Secondly, the section short-lists the potential sensing solutions. The criteria for short-listing includes the technical aspects and cost.

2.2.2.1 Temperature Conditions Inside Australian Sewers

There are significant amounts of research literature pertaining to technologies performing non-contact surface temperature measurement. However, little literature investigates the efficacy of temperature measuring technologies in harsh conditions such as in sewers. Although the sewer conditions are harsh, the temperature range is not extreme. For example, daily averages of gas phase temperatures inside confined sewers in Australia are tabulated in Table 2.1 [19, 64]. It can be noted that the temperatures can only fluctuate approximately between 15°C to 37°C.

Gas-phase temperatures inside confined sewer system [19, 64]			
Field site locations	Maximum temperature (°C)	Minimum temperature (°C)	Average temperature (°C)
Sydney (A)	29.7	15.0	21.6
Sydney (B)	28.8	15.3	21.3
Perth (A)	28.8	22.2	25.8
Perth (B)	36.6	14.0	27.0
Melbourne (A)	22.9	16.5	19.7
Melbourne (B)	24.5	17.7	20.7

TABLE 2.1: Gas-phase temperatures inside confined sewer system.

2.2.2.2 Comparative Analysis

Table 2.2 presents the feasibility analysis for comparing the previously discussed surface temperature measurement modalities.

Feasibility Analysis: Comparison of surface temperature measurement modalities			
Technology	Non-contact (Yes/No)	Feasibility (Yes/No)	Comments
Fluid expansion type	No	No	Low accuracy, low reliability and high response time. Automatic data logging is challenging.
Bimetallic type	No	No	Low accuracy, automatic data logging is challenging.
Thermistors	No	Yes	Small, inexpensive, rugged and reliable. Accuracy is better than RTDs and thermocouples
Thermocouple	No	No	Low cost and durable. Sensitivity is very low and the accuracy of thermocouples decreases with age.
Thermal imaging	Yes	No	Mature, fast clean and safe but expensive. Produce only relative temperature distribution profile. Challenging to use in high humid environments.
Infrared thermopile array	Yes	No	Low cost and durable. Slow to generate an image using the matrix of thermopiles. low accuracy and challenging to use in high humid environments.
Infrared radiometer	Yes	Yes	Expensive, reliable and accurate. Condensation affects the readings.
Fiber optic sensing	No	Yes	Relatively expensive, need to modify the sewer infrastructure to lay fiber optic cables.
Distributed temperature sensing	No	Yes	Expensive, need to modify the sewer network infrastructure to lay fiber optic cables.

TABLE 2.2: Feasibility Analysis: Comparison of surface temperature measurement modalities

2.2.3 Concluding Remarks

This scoping study on sensors for surface temperature measurements in sewers has short listed one non-contact type sensing technology and one contact type sensing technology as potential sensors. For non-contact type sensing: infrared radiometer sensor and for contact type sensing: thermistor sensor.

2.3 Sensor Characterization and Development for Measuring Surface Temperature

In the laboratory investigation on sensor characterization and development, experiments to study the performance of optical window, effects of incident angle, limit of detection, distance, lighting condition, reproducibility, humidity conditions, varying surface temperature conditions were conducted. Two surface temperature sensors, i.e. one IRR sensor and one epoxy coated thermistor sensor were used in this study. The thermistor sensor was employed as a reference measure for all the investigations carried out. For the statistical performance evaluation of laboratory experimentation, Mean Absolute Percentage Error (MAPE) and Root Mean Square Error (RMSE) were used as metrics. MAPE is used because of scale-independency and interpretability whereas RMSE aggregate the magnitudes of errors and it is sensitive to outliers.The MAPE and RMSE are given by Equation 2.1 and Equation 2.2 respectively, where T_{RIT} is the reference surface temperature measurements from the thermistor sensor and T_{IRR} is the surface temperature measurements from the IRR sensor, n is the number of samples and t is the instantaneous time.

$$MAPE = \frac{100\%}{n} \sum_{t=1}^{n} \left| \frac{T_{RIT} - T_{IRR}}{T_{RIT}} \right| \tag{2.1}$$

$$RMSE = \left[\frac{1}{n} \sum_{t=1}^{n} (T_{RIT,t} - T_{IRR,t})^2 \right]^{1/2} \tag{2.2}$$

2.3.1 Assessment of IRR Sensor's Optical Window in Varied Humidity Conditions

This test details the laboratory assessment of the IRR sensor's optical window after exposure to different humidity conditions inside a humidity chamber. Two approaches were shortlisted to mitigate the effects of fogging on the optical window surface. The first approach needs micro-controller based electrical heating of the optical window surface above ambient temperature so that it prevents the surface fogging. Although this approach yielded desired outcomes, it needed an additional power supply to keep the electrical circuitry active all the time. The second approach uses antifog coating material on the surface of the germanium made optical window and thereby avoids the need of an additional power source to prevent surface fogging. To evaluate this method, the sensing unit was placed inside the humidity chamber and set to different Relative Humidity (RH) levels such as 80% RH, 90% RH and 100% RH. The humidity chamber utilizes ultrasound humidification technology based air humidifier (LB 44, Beurer) for humidification inside the chamber and humidity sensor (DHT22, Aosong Electronics Co., Ltd) having 2-5% accuracy is used to measure the chamber's RH. Thereafter, a visual assessment of fogging on the lens was performed.

2.3.2 The Effects of Incident Angle on the IRR Sensor Performance and their Limit of Detection

This test evaluates the sensing performance of the IRR sensor by placing it at different incident angles from the surface of interest in dark lighting condition similar to confined sewers. In this evaluation, the IRR sensor was positioned at different angles so that the sensor focuses the concrete surface of interest proximity to the reference thermistor. The measurements from the sensors were collected and relative RMSE was computed for comparing the IRR sensor performance at different incident angles. This experiment was conducted in the laboratory conditions having the room temperature of 23°C and dark lighting condition. Also, the sensor has 22° half angle field of view, which makes the sensor to have the limit of detection in focusing the target surface.

2.3.3 Distance, Lighting Condition and Reproducibility

In this test, the sensing performance of the IRR sensor is studied in the laboratory by positioning the sensor at different distances from the surface of interest under varying lighting conditions. This test was conducted mainly to recognize the pertinent distance between the IRR sensor and target surface at the time of installing the sensor suite inside the sewer pipe. The IRR sensor was kept at different distances such as 10cm, 20cm, 30cm, 40cm and 50cm from the target surface. This experiment was conducted by placing the sensor at 90° angle to the concrete surface in both illuminated and dark lighting conditions. Then, MAPE was used as a metric for performance evaluation to study the effects of distance and lighting condition during measurements. Further, the reproducibility of the measurement by the IRR sensor was accessed by taking repetitive measurements. These experiments were conducted under the same operating conditions such as having same incident angle, distance and lighting condition. To calculate the reproducibility of the IRR sensor data, MAPE was used as a performance metric.

2.3.4 Performance of IRR Sensor in Higher Humidity Conditions

In general, the RH conditions of the sewer are over 80% [27]. In order to understand the effects of humidity during the IRR sensor measurements, the IRR sensor was exposed to different humidity conditions such as 80% RH, 90% RH and 100% RH inside the humidity chamber focusing the sewer exposed concrete. Then, the IRR sensor readings and the reference sensor readings were used to compute RMSE and MAPE for analysing the humidity effects during measurements.

2.3.5 IRR Sensor Performance with Varying Surface Temperatures

In this laboratory experimentation, we evaluated the IRR sensor by measuring the increased surface temperature inside the humidity chamber having 100% RH. The increased surface temperature levels were 25°C, 30°C and 35°C as in evaluating the methane sensor for sewer application [27]. A heating pad (HP-150, Auber Instruments) was also kept inside the chamber to increase the surface temperature levels to 25°C,

30°C, and 35°C. The reference thermistor sensor was affixed on the pad and IRR sensor was positioned to focus it. Then, the RMSE and MAPE were computed to analyse the effects of increased surface temperatures during measurements.

2.3.6 Sensor Development and Packaging

Two surface temperature sensors, i.e. one non-contact type IRR sensor (Apogee SI-111, ICT International) and one contact type thermistor sensor (THERM-EP, ICT International) were chosen for both laboratory testing and in-situ evaluation. Figure 2.1A shows the IRR sensor used in this work along with thermistor sensor shown in Figure 2.1B. The key specifications of the temperature sensors used in this study are summarized in Table 2.3. The IRR sensor is designed to operate in environments having 0% to 100% RH. However, it is not proclaimed to be applicable in wastewater industry for measuring surface temperature. In this regard, a reliable, robust enclosure system is an essential part of the durability of the sensing system. An enclosure made up of a stainless steel 316L grade material that can withstand the harsh environmental conditions was utilized. This enclosure is IP68 rated and ballistic-proof with an overall dimension of 380mm × 80mm × 165mm, and an internal usable area of 260mm × 80mm × 80mm. The enclosure unit has a wiper mechanism to clean the lens area before taking the surface temperature measurements. The internal area of the enclosure can accommodate an infrared radiometer sensor and electronics for the motor control. Before installing the actual sensors in the sewer, only the enclosure was deployed to evaluate its robustness in the municipal sewers of Sydney city at the Gore Creek Aqueduct. Figure 2.2A illustrates the deployment mechanism of the enclosure in sewers and Figure 2.2B displays the placement of the enclosure inside the sewer having H_2S approximately 5 ppm. As an outcome of this field testing, the sewer operators suggested an enclosure design that is easy to carry and mount on the sewer walls; less weight and should accommodate other sensors. Based on the findings and feedback from the sewer operators, the enclosure was redesigned. The new enclosure design overcomes the limitations of the previously tested design and it accommodates the IRR sensor, thermistor sensor and moisture sensor.

(A) [65]

(B) [66]

FIGURE 2.1: Surface Temperature Sensors (A) Infrared Radiometer Sensor (B) Epoxy coated thermistor sensor .

Name	IRR Sensor (SI-111)	Thermistor Sensor (THERM-EP)
Measurement Range	-30°C to +65°C	-40°C to +80°C
Operating Temperature Range	-55°C to +80°C	-40°C to +80°C
Accuracy	±0.2°C (-10°C to +65°C)	±0.05°C
Resolution	0.01°C	0.01°C

TABLE 2.3: Specifications of the surface temperature sensors used in this study.

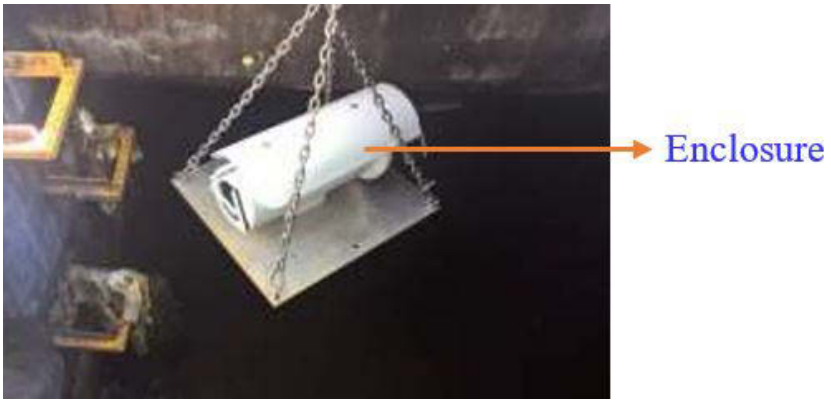

(A)

(B)

FIGURE 2.2: Enclosure testing in sewers. (A) Deploying mechanism of the enclosure (B) Enclosure inside sewer having H_2S around 5ppm.

The IRR sensor is placed inside the enclosure with an angle of inclination 45° focusing on the surface of interest. An optical window is placed in front of the IRR sensor. The optical window used in this study is made up of mono-crystalline germanium with wafer structure having 0.5 mm thickness and diameter of 26 mm. In order to prevent the surface fogging, the optical window has undergone nanometer coating using the fluorine and silicon group. This optical window reduces the effects of water bands below 8μm and above 14μm. Besides the temperature sensors, the sensing unit accommodates electrical resistivity based moisture sensor within the sensor enclosure. All the sensors were packaged in a tailor-made polyvinyl material enclosure. Then, to prevent moisture ingress into the sensor enclosure, plastic compound (Henley's Green Compound) was applied between the enclosure body and sensor lid. The sensor enclosure was designed to accommodate other sensors, to be easy to carry and easily mountable in sewers.

2.4 Field Deployment for Real-time Continuous Measurements Inside Hostile Sewer Infrastructure

An advanced sensor suite comprising sensing and monitoring unit was developed in the laboratory. After a significant amount of lab testing, the sensing suite was introduced to the real sewer environment for evaluating the sensing performance and the durability of the packaged sensors. Based on the recommendations of sewer operators from the Sydney Water, a sewer site at the Thornleigh area in the municipality of Sydney, Australia, was chosen for deploying the packaged units. This site was at a remote location, where there is no electricity and so, a long-term battery powered operation was a requisite. The sensing unit was installed near the crown of the sewer pipe for measuring the surface temperature variations (Figure 2.3A) whereas the monitoring unit was constructed outside the sewer pipe for accessing the data (Figure 2.3B and Figure 2.3C). The field monitoring campaign was carried out for about 96 days during the summer period in the Sydney city of Australia between 3rd November 2016 and 7th February 2017. The field application was done in a sewer having H_2S levels approximately ranging between 2 to 5 ppm. Although this study focusses on measuring surface temperature variable in the sewer system, other temperature variables that may impact the surface temperature like the ambient temperature of the sewer pipe and ambient temperature of the field site were also measured during the field trial campaign.

The sensing unit comprises two temperature sensors namely an IRR sensor and an epoxy coated thermistor sensor. Both the sensors measure surface temperature variations on the exposed concrete surface. The IRR sensor works of the principle of Stefan-Boltzmann Law [39]. The sensor converts the thermal radiations from the surface of interest into an electrical signal, which is used to compute surface temperature without contacting the surface. The thermistor sensor is used as a reference measure and it is a contact type sensor, which performs measurements by touching the surface of the sewer concrete wall. This sensor is made up of a semiconductor material in which resistance varies based on the sensing temperature. Both the sensors were housed in a specially built enclosure, which is made up of PVC material. This enclosure allows the tip of the thermistor to be in contact with the concrete surface while the body of the thermistor is insulated by the

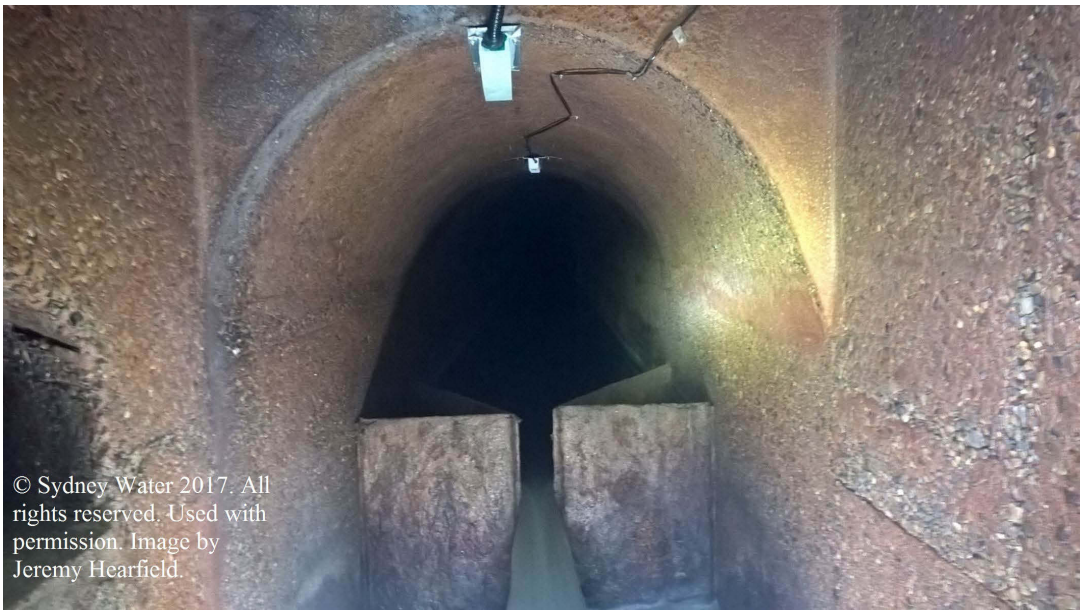

(A)

(B)

(C)

FIGURE 2.3: Field deployment of a sensor suite at a sewer site for real-time measurements of temperature variables. (A) Installations of the sensing unit at the crown of the sewer pipe for monitoring surface temperature variations (B) Construction of the monitoring unit outside the sewer pipe (C) Housing the monitoring unit using an electrical pillar box having vented air supply.

enclosure. Besides the surface temperature sensors, another two thermistor sensors were used to measure the temperature of the sewer air and ambient temperature of the field site. After each measurement, the sensor data was transmitted to the monitoring unit by using a 20 meters long cable. It was brought to our knowledge during the discussions with the sewer operators that the sensor cables transmitting signals need to be animal proofed mainly due to the reason that the vermin in sewers often nibble the cable sheathing. For this reason, the signal transmitting cables were placed inside an electrical conduit from the sensing unit to the monitoring unit.

In the monitoring unit, the incoming analog signals from the temperature sensors are converted into a digital signal by the signal processing unit. Then, the processed digital signal is sent to a logging instrument, where the data is stored after each measurement with the respective time-stamp. The data-logger (TSM-1, ICT International) having five differential ended analogue channels was used for logging all the temperature sensor measurements. The sensor system is set to perform measurements at an interval of one hour in hour boundaries. From the data logger, the sensor measurements data can be accessed and downloaded in the form of a comma separated values file (.csv). Due to the intrinsic safety concerns of the sewers, a DC battery was used to power the sensor system and placed in the outside monitoring unit. No direct access was provided to the sensing unit during the field testing. The sensors were controlled and the data from the sensors were accessed from the monitoring station, where the battery swapping took place. The sensor suite was powered by using 12V 100Ah rechargeable heavy duty batteries. In this field application, the sewer suite did not have an infrastructure to communicate remotely. Therefore, an operator checked the condition of the sensor suite once a week and swapped with fully charged batteries throughout the field trial. The entire monitoring unit was housed inside an electrical pillar box with vented air supply at the field site (Figure 2.3C).

2.5 Post-deployment Validations of the IRR Sensor After Long Exposure to Hostile Sewer Conditions

After completing the field trial campaign, the sensor system was brought to the laboratory for post-deployment validations. In this investigation, the durability of the sensor enclosure and the sensing performance of the IRR sensor were examined. Careful visual inspections were carried out to look for any degradation on the sensor enclosure and optical window. The IRR sensing performance experimentation was performed in the dark lighting conditions of the laboratory similar to the confined sewer system. The IRR sensor was measuring the surface temperature by placing the sewer exposed optical window and a new optical window to pursue comparative analysis. The measurements were obtained from each sensor at certain time intervals and then MAPE was used as a statistical metric to compute the relative percentage error between the IRR sensor and benchmark measures.

2.6 Improving Surface Temperature Measurements of IRR Sensor based on On-site Calibration

The IRR sensor used in developing the sensor suite was calibrated to provide surface temperature measurements for surfaces having emissivity value approximately 0.98. As the emissivity values can vary in different surfaces, there is a need to determine the emissivity value of the surface of interest for providing accurate measurements. In this regard, a method of field calibration was introduced to determine emissivity value of the sewer concrete surface during the Sydney summer period. The following subsection will present the theoretical considerations for determining the emissivity value and the on-site calibration method adopted.

2.6.1 Theoretical Considerations and On-site Calibration

The ratio of radiant energy emitted by the surface to that emitted by a blackbody at the same temperature is known as emissivity [67]. In [68], the radiant energy of infrared

surface temperature sensor is computed by using Equation 2.3.

$$E_{ir} = \epsilon_{is} T_{is}^4 + E \tag{2.3}$$

where E_{ir} is the radiant energy detected by the infrared surface temperature sensor, ϵ_{is} is the set emissivity of the sensor, T_{is} is the temperature measured by the infrared surface temperature sensor and E is the measurement error. According to [68], the radiant energy from the contact-type surface temperature sensor can be determined by using the expression in Equation 2.4.

$$E_{tr} = \epsilon_t T_{tr}^4 \tag{2.4}$$

where E_{tr} is the radiant energy detected by the contact type surface temperature sensor, ϵ_t is the true emissivity of the surface, T_{tr} is the temperature measured by the contact-type surface temperature sensor. By combining Equation 2.3 and Equation 2.4, the expression can be written as in Equation 2.5

$$\epsilon_t T_{tr}^4 = \epsilon_{is} T_{is}^4 + E \tag{2.5}$$

Upon rearranging, the Equation 2.5 can be written as in Equation 2.6

$$\epsilon_t = \epsilon_{is} \left[\frac{T_{is}}{T_{tr}}\right]^4 + \frac{E}{T_{tr}^4} \tag{2.6}$$

In [68], the component $\frac{E}{T_{tr}^4}$ of Equation 2.6 is sensor measurement error and assumed to be normally distributed, uncorrelated and with mean equal to zero. Upon simplification, Equation 2.6 can be written as $\epsilon_t = \epsilon_{is} \left[\frac{T_{is}}{T_{tr}}\right]^4$ [68]. In the field testing, the infrared surface temperature sensor is the IRR sensor and contact-type surface temperature sensor is the thermistor sensor. Therefore, the estimated emissivity of the surface is calculated based on the mathematical expression shown in Equation 2.7.

$$\epsilon_T = \epsilon_{IR}\left[\frac{T_{IRR}}{T_{RIT}}\right]^4 \tag{2.7}$$

where ϵ_T is the estimated emissivity of the surface, ϵ_{IR} is the set emissivity of the IRR sensor, T_{IRR} is the surface temperature measured by the IRR sensor and T_{RIT} is the surface temperature measured by the reference instrument thermistor. In this study, for the surface temperature correction analysis, surface temperature data of about 5 days between 3rd November 2016 and 8th November 2016 were taken as a sample dataset for determining emissivity coefficient. This implies that ϵ_T is determined by using the sensor data of about 5 days. The mean value of ϵ_T is denoted by μ. The value of ϵ_{IR} for the IRR sensor is 0.98.

The relative difference between the reference instrument thermistor and IRR sensor readings is termed as pre-correction data. After determining the emissivity coefficient, the surface temperature was improved by correcting the measured readings. This data is termed as post-correction data. Surface temperature measurements were corrected by using the data from 9th November 2016 to 31st January 2017. The surface temperature measurements from the IRR sensor is corrected by using Equation 2.8, where the $Corrected\_T_{IRR}$ is the corrected surface temperature measure of the IRR sensor measurements. Also, the ϵ_T in the below Equation 2.8 denotes $\mu(\epsilon_T)$.

$$Corrected\_T_{IRR} = \left[\frac{\epsilon_T}{\epsilon_{IR}}\right]^{1/4} T_{IRR} \tag{2.8}$$

The RMSE in Equation 2.2 was used as a statistical performance metric for evaluating the temperature correction after determining the emissivity coefficient.

2.7 Experimental Results

This section presents the experimental results of pre-deployment evaluation, field deployment evaluation, post-deployment evaluation and improvisation of surface temperature measurements.

2.7.1 Pre-deployment Evaluation: Sensor Characterization and Development

2.7.1.1 Evaluation of IRR Sensor's Optical Window

This section demonstrates the laboratory assessment results of the IRR sensor's optical window after being exposed to different humidity conditions inside a humidity chamber. The different humidity conditions are 80% RH, 90% RH and 100% RH. Figure 2.4 presents the images of optical window surface exposed to different humidity levels in the test chamber. The images appear to be gloomy because they were captured in high humidity conditions inside the chamber and also due to lighting conditions of the laboratory. Careful visual inspection revealed that the surface of the germanium-made anti-fog coated optical window led to no surface fogging. Therefore, this antifog coated optical window is regarded as a viable solution to overcome the effects of surface fogging in sewers.

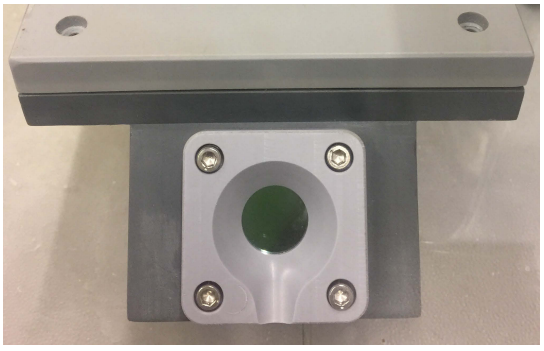

(A)

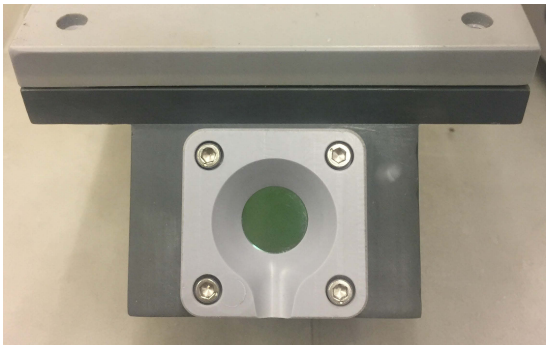

(B)

(C)

FIGURE 2.4: Assessment of the optical window exposed to different relative humidity conditions inside the humidity chamber. (A) 80% RH (B) 90% RH (C) 100% RH.

2.7.1.2 Evaluating the Effects of Incident Angle and Limit of Detection

This evaluation demonstrates the effects of incident angle in the IRR sensor performance and their limit of detection. Figure 2.5 presents the statistically calculated proportions of MAPE for different incident angles, where it can be observed that the variations were relatively small ($\leq 0.5\%$) with no obvious pattern. The relative difference between the sensor and reference measure being less than 2.5% is generally regarded as reliable sensing [28]. In this test, the MAPE for the IRR sensor measurements is less than 2.5% implying the effects of the incident angle between 30° and 150° is reliable and has an imperceptible impact on the IRR sensor performance. The half angle field of view of the IRR sensor which is 22° needs to be considered while mounting the sensor.

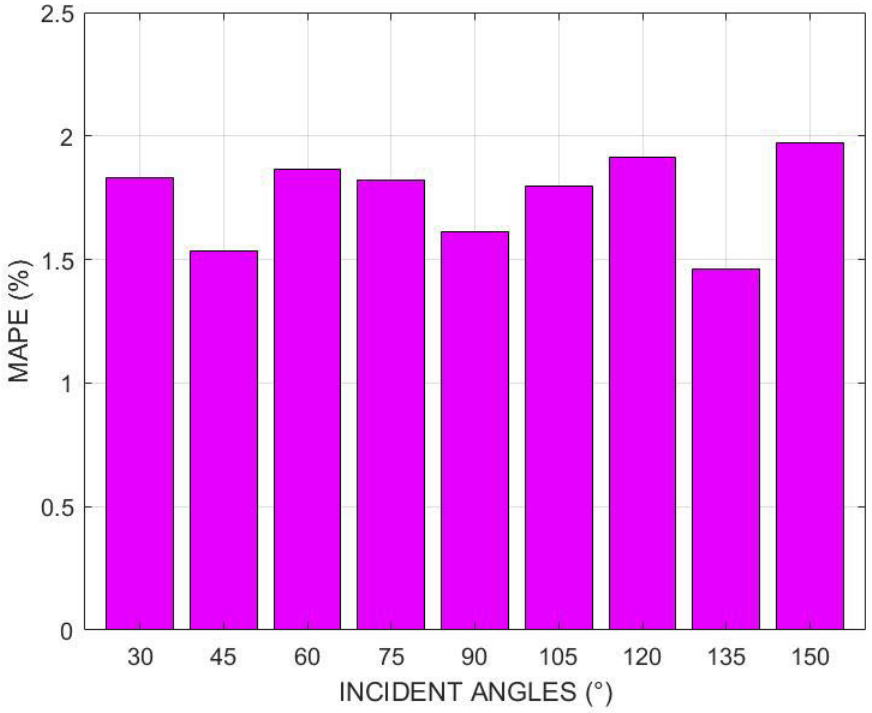

FIGURE 2.5: Performance efficacy of IRR sensor by positioning it at different incident angles from the surface of interest.

2.7.1.3 Evaluating the Effects of Distance, Lighting Condition and Reproducibility

This section presents the evaluation results of the effects of distance, lighting and their reproducibility. Figure 2.6 presents the computed MAPE (%) for the measurements obtained at different distance and lighting condition, where it can be observed that the percentage of MAPE is higher for the dark lighting condition than the illuminated lighting condition for all the distances between 10cm and 50cm. However, the effects of distance in a particular lighting condition had a negligible impact on the performance of the IRR sensor. From Figure 2.5 and Figure 2.6, it can be observed that the MAPE for the IRR sensor performance under different incident angle, distance and lighting conditions is smaller than 2.5%. This implies that the IRR sensor has good reproducibility similar to the sensor monitoring methane in sewers [28].

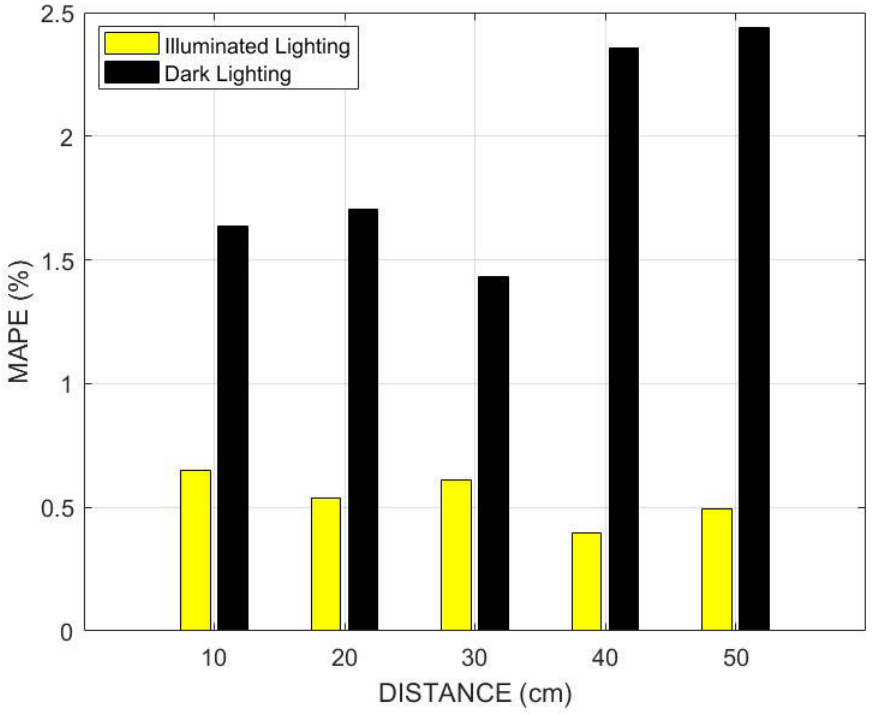

FIGURE 2.6: Statistical comparative analysis of IRR sensor measurements obtained in illuminated and dark ambient conditions by positioning the sensor in different distances.

2.7.1.4 Evaluating the Performance of IRR Sensor in Higher Humidity Conditions

This evaluation demonstrates the performance of the IRR sensor in different RH levels (80%, 90% and 100%). Figure 2.7 presents the computed RMSE and MAPE by using the IRR sensor readings and the reference readings. It can be observed from Figure 2.7 that the RMSE for the range of 80-100% RH was less than 0.5°C and shows no symmetric trend for the different humidity levels. This indicates that the IRR sensor can be used with no further calibration as the IRR sensor is factory calibrated for operating in 0-100% RH conditions. Similar to the laboratory aforementioned experimental results, this test results present MAPE less than 2.5% for the conditions of 80-100% RH (Figure 2.7). These results clearly demonstrate the performance of the IRR sensor is not affected by the high humidity conditions and provides credible measurements.

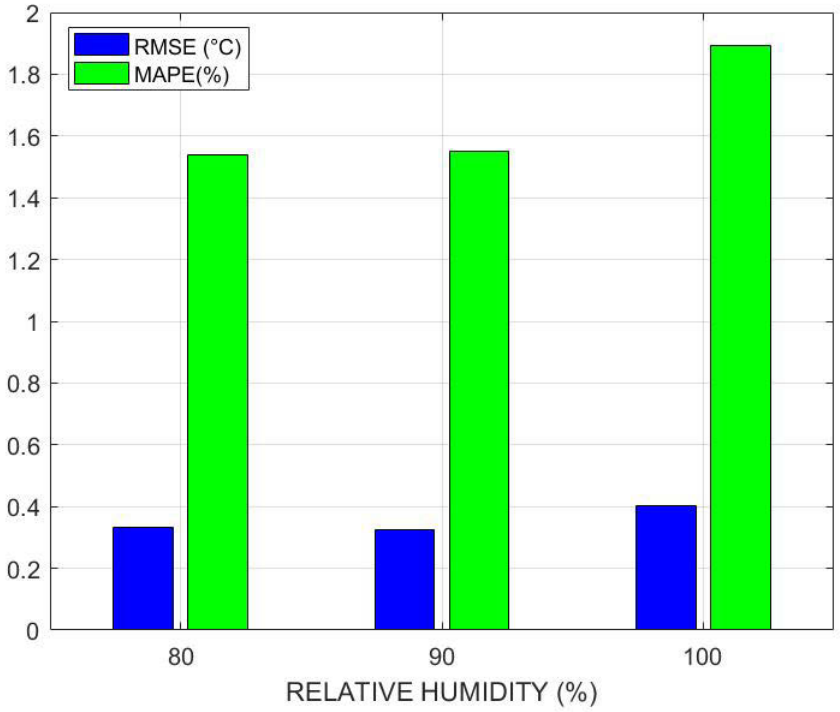

FIGURE 2.7: Computed measures of RMSE and MAPE illustrating the IRR sensor performance under different humidity conditions.

2.7.1.5 Evaluating the IRR Sensor Performance with Varying Surface Temperatures

This evaluation presents the effects of the IRR sensor at increased surface temperature measurements. Figure 2.8 presents the computed RMSE and MAPE for comparing the IRR sensor performance at different temperature levels. It can be noted that the RMSE for all the three temperature levels were approximately 0.4°C. However, the MAPE showed a decreasing trend from 25°C to 35°C. This is due to the reason that the reference measure and IRR sensor measure showed a difference of around 0.4°C while the temperature for each level increased by 5°C. The implications of the results were reasonable and indicate that the IRR sensor can acquire effective measurements under increasing surface temperature levels.

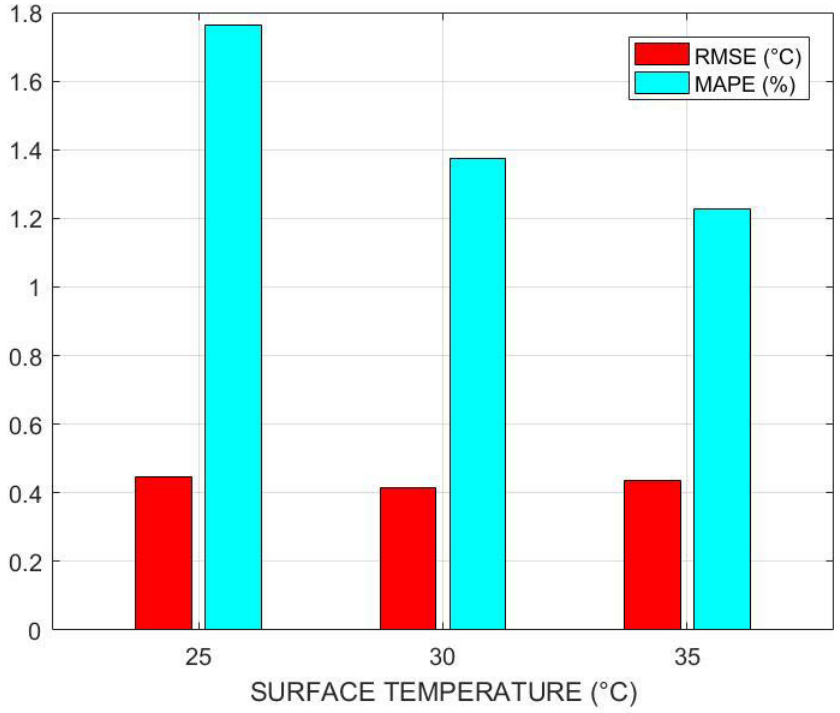

FIGURE 2.8: Computed measures of RMSE and MAPE illustrating the IRR sensor with varying surface temperature.

2.7.1.6 Sensor Development and Packaging Prior to Sewer Deployment

Figure 2.9A presents the newly designed CAD model of the sensor enclosure, illustrating the placement of sensors within the package, where the green colour indicates the IRR sensor and the red colour indicates the moisture sensor. Then, this model was transformed to a physical model made up of PVC material as shown in Figure 2.9B and Figure 2.9C, prior to sewer deployment. The sensor enclosure was designed to mount the sensor unit easily in sewers.

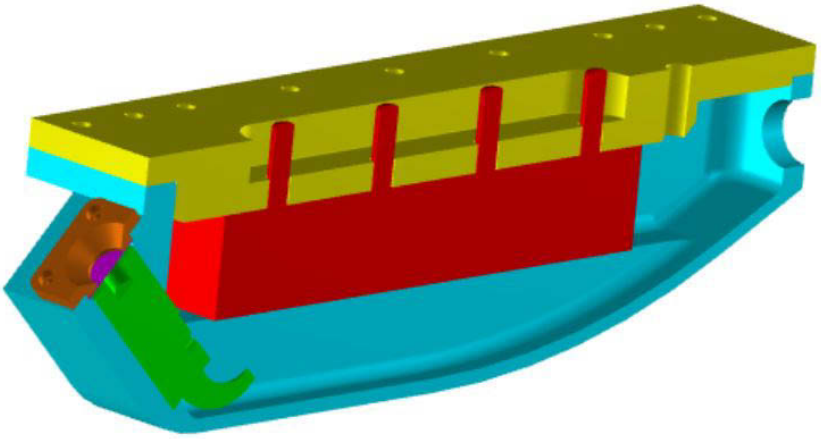

(A)

(B)

(C)

FIGURE 2.9: Sensor enclosure. (A) New enclosure CAD Model (B) Top-view of the sensor enclosure (C) Front-view of the sensor enclosure.

2.7.2 Field Deployment Experimentation: Data Collection and Analysis

2.7.2.1 Real-time Sensor Data Showing Temporal Dynamics of Surface Temperature Measurements from the Sewer Pipe

The surface temperature data obtained from the sewer monitoring campaign using IRR sensor is shown in Figure 2.10, where it can be noticed that there is no sharp variation of measurements between the days. The monthly average of surface temperature measurements for November 2016, December 2016 and January 2017 was 20.30°C, 21.89°C and 23.25°C respectively. For the first week of February 2017, the average surface temperature was 23.88°C. Overall, the average surface temperature measure obtained from the IRR sensor during the field trial was 22.22°C. Figure 2.10 also presents the surface temperature data acquired with the reference instrument thermistor sensor. From both the sensors, the dynamics of the surface temperature profiles were captured reasonably and displayed a similar pattern throughout the field trial. Diurnal pattern tends to vary approximately less than ±1°C. The mean relative difference between the measurements of two sensors was 0.67°C. Overall, the data from both the sensors showed an increasing trend from the month of November 2016 to February 2017. Sewer corrosion is estimated to be 70% higher when the pipe surface temperature is colder by 1°C relative to the sewer air temperature [69]. Hence, sensor accuracy lesser than 1°C is vital.

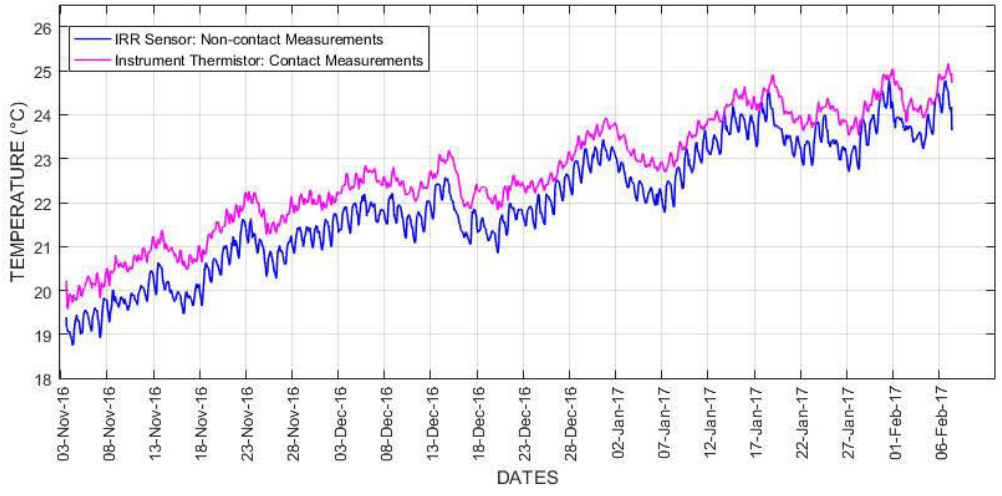

FIGURE 2.10: Surface temperature profiles from IRR sensor and thermistor sensor.

2.7.2.2 Comparative Analysis of Temperature Variables Data

Figure 2.11 shows the profile of sewer ambient temperature measured by the thermistor sensor and the surface temperature profile acquired using IRR sensor. The sewer air temperature and the surface temperature tends to follow a similar pattern. However, there is a slight difference between the two variables due to the reason that the surface takes time to be in equilibrium with the atmospheric temperature. Also, during the night time the difference between the temperature increases. This can be due to the IRR sensor, prone to lighting inside sewers. Figure 2.12 presents the daily average values of surface temperature measurements from IRR sensor and the ambient temperature of the field site. A thermistor sensor was installed on 26th November 2016 to measure the ambient temperature outside the sewer pipe. In Figure 2.12, it can be recognized that the average daily surface temperature remains to be increasing as long as the ambient temperature of the field location increases. In contrast, the surface temperature pattern tends to decrease when the ambient temperature of the field location decreases. This phenomenon implies that the surface temperature of the sewer tends to behave as the dynamics of the sewer air temperature, which synchronizes with the ambient temperature outside the sewers. Hence, there is a clear correlation between the temperature outside the sewers and inside temperature.

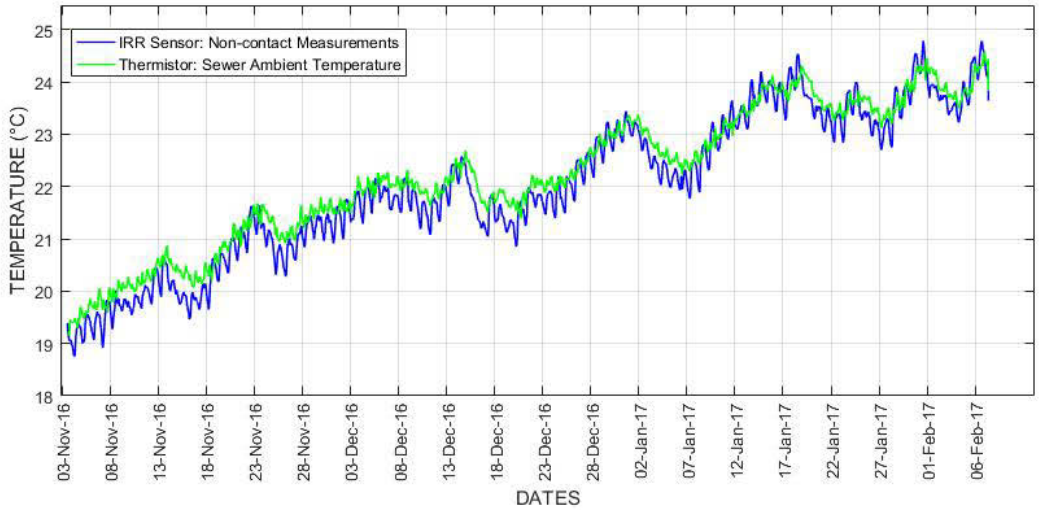

FIGURE 2.11: Comparison of surface temperature profile from IRR sensor with the sewer ambient temperature profile from the thermistor sensor.

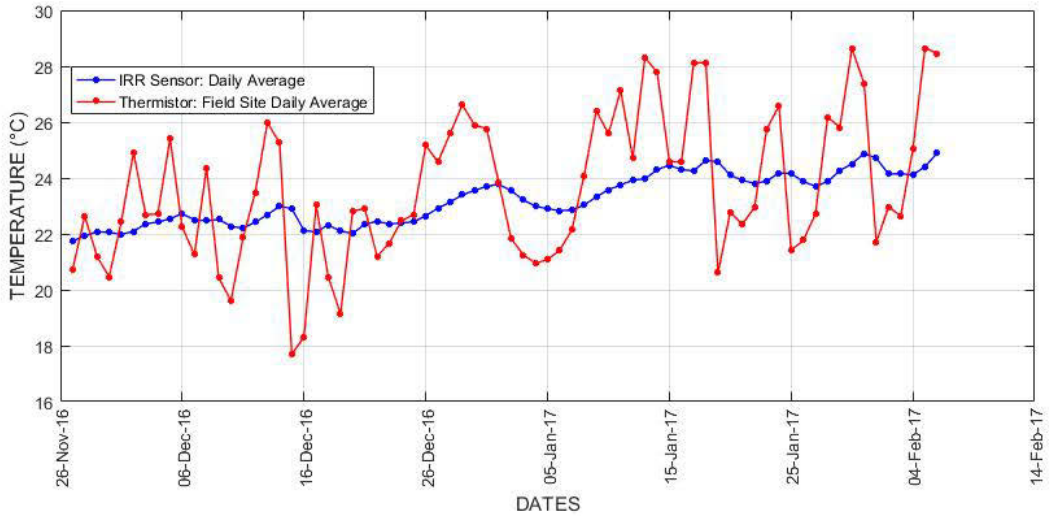

FIGURE 2.12: Comparison of daily average surface temperature profile from IRR sensor with the daily average of ambient temperature outside the sewer pipe.

2.7.3 Post Deployment Validations

The sensor enclosure was visually inspected after field trial program. No visual damages were apparent on the sensor enclosure other than a slight decoloration of the material. The IRR sensor with antifog coated germanium optical window was used in sewers for non-contact type measurements. There was a slight visual degradation observed on the antifog coated optical window after 96 days of exposure to the aggressive conditions of the sewer (Figure 2.13B). The degradations were in the initial stages around the edges of the optics and the central part remains unaffected. As a part of preventive maintenance, it is recommended to replace the lens once in three months for accurate measurements.

The sensing performance of the IRR sensor was evaluated with the sewer exposed germanium optics and with the new germanium optics. The reference instrument thermistor sensor was used as a benchmark against the IRR sensor measurements and thereby MAPE was computed between the two sensor measurements. The MAPE for the IRR sensor measures using the new optics was 1.41% and for the IRR sensor measures using the sewer exposed optics was 2.21%. Despite the exposure of the IRR sensor to the aggressive sewer conditions, the MAPE of the IRR sensor is less than 2.5%, which was the case even in the laboratory experiments under dark lighting conditions prior to the

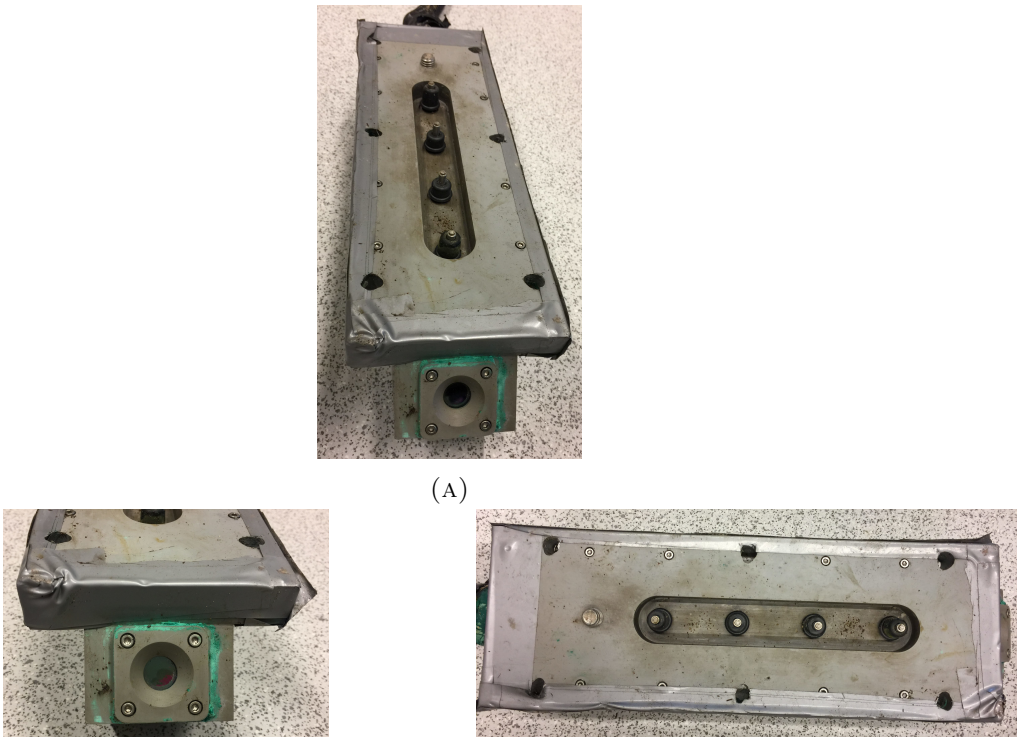

(A)

(B) (C)

FIGURE 2.13: Sensor enclosure after exposure to hostile sewer conditions. (A) Front view of the sensor enclosure (B) Picture showing the degradation on the germanium optical window (C) Top view of the sensor enclosure.

field deployment. Therefore, this evaluation demonstrates the IRR sensor is in good condition with reliable sensing measures.

2.7.4 Improved Measurements of IRR Sensor with Post Calibration Analysis

Surface temperature measurements were corrected by using the data from 9th November 2016 to 31st January 2017. Figure 2.14 shows the plots of error differences between the pre and post correction IRR sensor data. The RMSE was used as a performance metric for evaluating the surface temperature correction performance. The RMSE of the pre-correction data and post-correction data is 0.72°C and 0.25°C respectively. Because of the temperature correction based on the estimated emissivity value, it can be observed that the surface temperature measurements can be improved with estimated concrete sewer emissivity post-calibration.

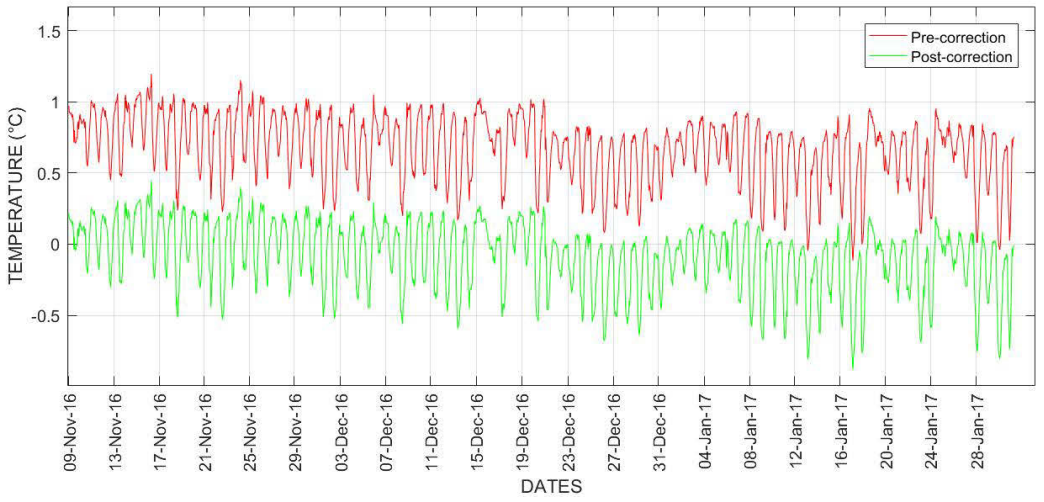

FIGURE 2.14: Improving surface temperature measurements of the IRR sensor between November 2016 and January 2017.

2.8 Summary

The research study presented in this chapter has developed a robust sensor technology for measuring temporal dynamics of the surface temperature in hostile sewer conditions. The author believes that this is the first study to prove non-contact type surface temperature sensing in sewer system. In this regard, this chapter has led to the following key contributions:

1. A scoping study was conducted to review the currently available surface temperature measuring devices indicating the suitability of using them in sewers. Almost all the sensors have their applications in non-sewer conditions, but the scoping study has short-listed two temperature sensors as the potential sensing solutions. They are: (i) infrared radiometer (non-contact type sensing) and (ii) thermistor sensor (contact type sensing).

2. A comprehensive evaluation was conducted in the laboratory condition to characterize and develop the IRR sensor suite for sewer deployment. In this regard, experiments on the performance analysis of optical window, the effects of incident angle, limit of detection, distance, lighting condition, reproducibility, humidity conditions and varying surface temperature were investigated. As an outcome of

these investigations, the IRR sensor demonstrated reliable sensing to the aforementioned environmental conditions.

3. From the field testing experiments, the study has revealed that the IRR sensor with an antifog coated germanium optical window can be used for non-contact surface temperature measurements in sewers. There was a slight degradation observed in the antifog coating after 3 months in the sewer. So, this sensor is more suited for deployments of about three months or can be used on moving platforms and human traversing. For long-term sensing operations using IRR sensor, it is recommended to replace or coat the optical window with antifog material after three months of use. The thermistor sensor has proven to be reliable and it can be used in sewers for contact-type sensing.

4. The post-deployment validations showed the robustness of the sensor enclosure under the aggressive environmental conditions of the sewer. The post validation lab experiments showed that all the temperature sensors were operating as desired and no bias was observed. Therefore, it can be concluded that all the sensors performed reasonably well in sewers and their data are legitimate.

5. A method to improve the accuracy of IRR sensor measurements based on the emissivity correction was shown in this work. By determining the emissivity coefficient of the sewer concrete surface, the temperature measurements of IRR sensor was corrected for the summer period of Sydney city.

6. It is believed that the real-time continuous measurements from the developed IRR sensor suite will provide information-rich data to the analytical models for better prediction of corrosion in sewers. Overall, the contributions of this chapter can enhance the waste water utility's present sewer corrosion monitoring capabilities. However, in order to fully utilize the sewer corrosion prediction model, there is a need to measure the surface moisture conditions on the concrete sewers.

From the works presented in this chapter of the dissertation, the following publications resulted as an outcome.

- **K.Thiyagarajan**, S. Kodagoda, R. Ranasinghe, D. Vitanage and G. Iori, "Robust sensing suite for measuring temporal dynamics of surface temperature in sewers," in Nature - Scientific Reports. *(Under Review)*

- **K.Thiyagarajan**, S. Kodagoda and J. K. Alvarez, "An instrumentation system for smart monitoring of surface temperature," 2016 14^{th} International Conference on Control, Automation, Robotics and Vision (ICARCV), Phuket, Thailand, 2016, pp. 1-6.

- S. Kodagoda, R. Ranasinghe, **K.Thiyagarajan**, G. Dissanayake, "Predictive Analytics for Sewer Corrosion - Final Report". Pages: 1-18, 2017.

- S. Kodagoda, R. Ranasinghe, **K.Thiyagarajan**, J. K. Alvarez and G. Dissanayake, "Sensors for Surface Temperature and Surface Moisture Measurements - Scoping Study". Pages: 1-35, 2016.

Chapter 3

Robust Sensor Technology for Measuring Surface Moisture in Sewers

3.1 Introduction

In distinction to the sensor technology developed in the preceding chapter, another sensor technology that has a significant role to play in predicting the microbial induced concrete corrosion throughout the sewer network is the one that can quantify surface moisture conditions of the concrete gravity sewers. However, water utilities often use indirect measures like the relative humidity of the sewer air as an input to predict corrosion. This is primarily due to unavailability of technologies in the state-of-the-art systems and sensing limitations, as it is difficult to reliably measure moisture at the concrete surface, due to the corrosive nature of sewer environment. Hence, this chapter of the dissertation focusses to develop a robust sensing system for measuring moisture on the surface of the concrete sewer. The information from the developed sensing system is expected to be utilized by water utilities for assessing the impacts of sewer corrosion in the networks using predictive modelling for asset maintenance and monitoring programs.

Researchers have mainly focused on monitoring the specific parameters to investigate the ambient conditions of the sewer by using commercially available sensing technologies [70–72]. For instance, few studies have demonstrated the feasibility of monitoring relative humidity levels inside the corrosive sewer pipes in different cities of Australia including Sydney, Melbourne and Perth, where the researchers have reported the daily averages of relative humidity [73]. Humidity sensors were developed by using advanced sensing methods such as fibre optic technology for sewer applications like detecting leakages in sewer tunnels [74]. Recently, humidity measurements near the concrete surface were measured using Fibre Bragg Grating based sensors for in-sewer applications [29]. However, [64] illustrated a functional relationship between moisture content and relative humidity, in which higher humidity levels inside sewers does not necessarily imply higher moisture on sewer walls. Although there are several literatures pertains to monitoring relative humidity in sewers, there are no reports till date on measuring concrete surface moisture conditions inside sewers.

This chapter of the dissertation studies the possibility of measuring surface wall moisture conditions, which is a better proxy that can add value to the current development of corrosion modelling and data analytics. Therefore, it is important to develop a system that can measure the surface moisture conditions at different locations in sewers to correctly estimate the surface moisture distribution of the sewer wall. Since there are no systems available in the market to readily measure surface moisture conditions in sewers, the sewer operators defined several requirements in developing the moisture sensor suite. The main requirements are i) sensing method should not cause any damages to the exposed concrete sewer surface, ii) no flammable substances inside sewers, iii) easy access to sensor data, iv) sensor enclosure should accommodate other sensors like temperature sensor, v) enclosure should possess less-weight and robustness to hostile sewer conditions and vi) easy to carry and mount design of enclosure.

In this chapter, the development and evaluation of the sensor suite for real-time measurements of surface moisture conditions in sewers is elucidated. In the laboratory investigation, the behaviour of concrete moisture with electrical resistance and different pH aqueous solutions were studied by utilizing a data-driven machine learning approach. This study led to utilize the Wenner array method to determine the surface moisture

conditions based on concrete surface electrical resistivity measurements. Once the sensor suite was tested and packaged in the laboratory, it was deployed in the sewer environment for studying the sensing performance. From the field testing campaign, electrical resistivity measurements were obtained from the surface of interest. Then, on-site calibration was carried out to determine the surface moisture conditions of the measured sewer surface. After completing the field testing, the sensing suite was evaluated in the laboratory conditions to examine its sensing capabilities after exposing the sensor suite to aggressive sewer conditions for about three months. Further, in the off-line analysis, temporal variations of moisture and the effects of ambient temperature and surface temperature were investigated. In addition, this chapter investigates the effects of rebar during measurements. This chapter is distinct from those existing in the current literatures in a form that it supplies the needed data about the surface conditions of the concrete sewer rather than the ambient gaseous variable such as relative humidity.

The remainder of this chapter is organised as follows: Section 3.2 presents the scoping study of sensors for surface moisture measurements. Section 3.3 details the experimental evaluation to study the behaviour of concrete moisture with electrical resistance and pH conditions. Section 3.4 describes the specifications of the sensor and pre-deployment evaluations. Section 3.5 details the procedure adopted to deploy sensor in the field for real-time evaluation and data collection. Section 3.6 presents the post-deployment investigations. Section 3.7 studies the effects of rebar during moisture measurements. Section 3.8 presents the experimental results with analyses and finally, Section 3.9 summarises the main contributions resulting from this chapter with research outcomes.

3.2 Scoping Study: Sensors for Surface Moisture Measurements

This scoping study of sensors for surface moisture measurements investigates a wide range of moisture measurement techniques with the aim of selecting a practically feasible moisture sensor that can potentially be used to measure the surface moisture conditions in sewers.

3.2.1 Sensors for Moisture Sensing

Surface moisture is the free water retained on the surface of aggregate particles and considered to be part of the mixing water in concrete [75]. In this context, this section covers the review of relevant literatures about the technologies that are associated with the motivation of this research work for measuring moisture conditions. The sensing techniques are broadly classified into following types:

1. Gravimetric method
2. Gamma densitometry method
3. Electrical resistivity method
4. Capacitance sensor
5. Resonator based methods
6. Time Domain Reflectometry based sensors
7. Frequency Domain Reflectometry based sensors
8. Fibre optic sensors
9. Micro Electro Mechanical Systems Sensors
10. Hyperspectral Sensing

3.2.1.1 Gravimetric Method

Gravimetric methods are the most simple, but reliable technology for measuring moisture presence in concrete.

Technology: Gravimetric methods measure weight differences of the mass of water to dry weight sample. This may also be calculated as the difference of the volume of water to the total volume of the concrete sample [76]. This generally involves taking full-depth core sample using a dry-cut process followed by drying in an oven until a constant weight is reached. Initial and final weights are used to calculate the overall moisture content of

the sample. The measuring technologies [77, 78] may contain infrared lamps as a heat source and can measure the moisture content automatically.

Discussion: The gravimetric methods are the most simplistic, direct and reliable measurements. However, they require a reasonable number of measurements for averaging to improve the reliability of the measurement. This is one of the few methods that can be used in high moisture contents [77]. However, it only can provide water content of the whole sample portion rather than the surface moisture content. The requirement of a core sample for each measurement is also prohibitive in the sewer monitoring application. However, this method may be used for validation purposes.

3.2.1.2 Gamma Densitometry Method

Gamma densitometry is used to measure the local variation of water content in the material.

Technology: The principle of the Gamma densitometry uses a beam of gamma ray passing through concrete. Gamma rays are emitted by a radioactive source. The mass variations of the traversed points can be measured as the relative intensity of the transmitted particles [79]. Assuming that the mass losses due to chemical evolution are negligible but they are solely due to water evaporation, thereby profile of water content can be estimated.

Discussion: One advantage of this method is that the technology can be used to measure moisture at different depths. However, it assumes the same flow interception volume of material at each measurement [79]. This technology is bulky, expensive and most suited for lab environments. The testing material should be in-between the radioactive source and the receiver and hence there are practical limitations in using this technology in sewers.

3.2.1.3 Electrical Resistivity Method

In general, the electrical resistivity of a porous material decreases with an increase of moisture content. This is due to the low resistivity of the pore fluid than that of the

solid material. Therefore, it is well known that the changes in moisture content can be monitored by measuring the changes in the electrical resistivity of the material [80].

Technology: This is a simple technology, where a voltage is applied between two electrodes embedded in concrete and the resulting current is measured. The ratio of voltage to current gives a resistance. In general, calibration procedures are utilized to estimate the moisture content from the measured resistance. The Wenner probe method uses a four electrode system that applies a sinusoidal current of frequencies from 50Hz to 1kHz [81]. The electrodes can be embedded at desired depths for measuring internal concrete moisture or can be kept in contact with the concrete surface to determine surface moisture conditions.

Discussion: This technology can be affected by the variations in the contact between the electrodes and cement. This variation can be due to electrochemical reactions and shrinkage cracks [82]. Further, variations in temperature can affect the measurements. For example, Polder [81] demonstrated that for every degree (Kelvin) of temperature change, there can be a moisture content variation of 3% for saturated and 5% for dry concrete. Therefore, this method could be a feasible option that could be used in sewer environments for determining the moisture conditions based on electrical resistivity measurements.

3.2.1.4 Capacitance Sensor

A dielectric material is an electrical insulator that can be polarized by an applied electric field. While it is placed in an electric field, it creates dielectric polarization. A common application is a capacitor. Change in dielectric material causes a change in the capacitance.

Technology: [83] uses a co-planar structure consisting of multiple parallel fingers as part of the capacitance sensor. It measures the dielectric constant (relative permittivity) of the material by applying fringing electric fields into the material. Two sensors are used for the moisture measurement; a meander sensor and a circular sensor. A change in concrete water content is related to a change in capacitance.

Discussion: In general, capacitive sensors are well suited for moisture measurements in bulk solids [84]. Presence of water alters the dielectric constant of the material of

interest. This change can be used to estimate the moisture content. This method needs a calibration process and can be affected by the chemicals present in the sewers. This method can also be influenced by foreign particles that can deposit on the plates including the water droplets which restricts the use of it in harsh sewer conditions.

3.2.1.5 Resonator Based Methods

Resonators naturally oscillate at resonant frequencies [85]. Radio Frequencies (RFs) can be used in conjunction with resonators to estimate the material properties. The RFs exist in a wide range of frequencies (3kHz to 300GHz) and hence the measurement method needs to be customized based on the material of interest. Microwaves (1GHz to 100GHz) are a popular choice for measuring moisture content. The history of microwave technology goes back to 1950s, however, it was not a popular sensing technology until 1980s when solid state devices were invented [80]. The technology can be used to characterize materials based on permeability and permittivity and hence the quantities such as moisture content. Nuclear resonators are also used in moisture content measurement applications.

Technology: The microwave attenuation technology uses a transmitter on one side and a receiver on the opposite side of the sample. When a microwave beam passes through a porous material, it undergoes an attenuation and a phase change. The presence of moisture affects both attenuation and phase change [80]. Therefore, real and imaginary components are often combined to estimate the moisture content independent of density. It alleviates the need to estimate the density of the material. Microwave resonators are used to measure the interested frequencies.

Discussion: The requirement of a transmitter and a receiver on opposite sides of the sample makes the microwave attenuation type technology very challenging to be used in sewers. Further, it is not desirable to use higher frequencies or higher moisture contents as both leads to drastic attenuation of the signal. It is possible to use transmitter/receiver on one side of a sample, however, it is challenging as the microwave technology finds it difficult to penetrate higher depths while returning high signal back for analysis [80]. Further, the attenuation of microwave signal increases with higher frequencies and moisture contents. Therefore, using this technology for measuring higher

moisture contents is still a challenge. The nuclear resonator based sensors consist of a certain amount of radioactive materials [85] and hence the manufacturers face distribution and export restrictions. Further, nuclear based sensors have a stringent waste disposal process heavily regulated by the government. The users need extra training and safety procedures and the sensors are in general expensive. Therefore, the use of nuclear based resonators are not very attractive.

3.2.1.6 Time Domain Reflectometry based Sensors

Time Domain Reflectometry (TDR) can be used to determine the dielectric constant of an object and hence inferring the volumetric water content of different materials such as soil [86]. This technology has been heavily used in soil moisture measurements. The first reported application of this method was in 1980 and hence a relatively new technology [86].

Technology: This technology is typically used in tele-communication industry to identify the dis-continuities of cables. A pulse generator was used to generate an electromagnetic wave and the propagation time of electromagnetic waves were used to determine the dielectric constant of the material under test [86]. In invasive type, electrodes need to be inserted into the material. The incident electromagnetic wave reflects once it reaches an impedance difference between the cable and the probe. The rest of the wave propagates through the probe and reflects back at the boundary between the probe and the material. The round trip is measured to estimate the dielectric constant of the material under test [86].

Discussion: As the dielectric constant of water is larger (about 81) than that of soil (about 3 - 5), this method is relatively robust to different soil compositions [86]. However, TDR measurements are affected by the temperature variations. This method is invasive and could be affected by the distribution of the moisture content within the probe length. Further, the TDR measurements are affected by the salinity of the pore solutions and hence the naive use of it is challenging.

3.2.1.7 Frequency Domain Reflectometry based Sensors

Frequency Domain Reflectometry (FDR) has similarities with the capacitance based sensor and can be often regarded as the same. FDR is mostly used in soil moisture measurements and there are not reported in sewer applications [87, 88].

Technology: In the FDR technology, an oscillator is used to generate a high frequency signal which is propagated through electrodes. It exploits the standing wave principle and dielectric properties of the water and interested material. The dielectric constant of water is very high (about 80) and that of soil is about 3, air is 1 and concrete is about 4. Therefore, any difference in the volumetric ratio of the water and the material results in a higher dielectric constant. Therefore, once calibrated, moisture content in the material can be estimated.

Discussion: FDR sensors produce reasonably accurate results. However, they need calibration with the material in use. It is an invasive method, meaning the electrodes need to be embedded in the material. However, this could be an option to consider in sewer applications as it is faster when compared with TDR and less complex hardware for data acquisition.

3.2.1.8 Fibre Optic Sensors

Fiber optic technologies are used in many sensing applications and often rely on a change of an optical property of a material. There are several fiber optic sensing technologies that can be used in high relative humid and moisture measurements. Those can be categorized as Fiber Grating (FG) sensors, FBG sensors, long period grating sensors, evanescent wave sensors, interferometric sensors and hybrid (grating and interferometric) sensors and absorbance sensors [89]. The recent approaches which are related to the specific sewer environments are discussed as follows.

FBG Sensors Technology: The FBG technology uses a grating inscribed into the optical fiber to select a particular wavelength of the light from a broadband source. This particular wavelength is reflected back into the light source producing amplified Critical Wavelength (CW) [90]. If the grating spaces are shrunk or expanded by any phenomenon,

there is a shift observed in the CW. This shift in the CW can be qualitatively related to the source of the strain, for example strain, load and temperature. Therefore, humidity can be measured by configuring the FBG sensor by applying hygroscopic polymer coating over a grating inscribed fiber optic cable. Once the polymer coating swells in contact with water, it causes strain and hence shift in the CW. The response is reversible and therefore it can be used to measure humidity [90].

In [74], the FBG consists of a bare and polyimide-coated FBG. The polyimide acts as a hygroscopic coating. It absorbs water molecules and swells causing strains on the FBG. This experienced strain is linearly proportional to the applied relative humidity. It is a useful measurement of ambient relative humidity which can be determined by comparing the shifts in the Bragg's wavelength with prior calibration values [74]. The accuracy can be improved by compensating for the temperature effects. Therefore, an uncoated section is also used in conjunction with the sensor for measuring the temperature and subsequent compensation. Further, in order to minimize the other environmental effects, proper packaging including a PEEK tube with a perforated tip is used. A permeable PTFE membrane is used to protect the permeable tip from dirt and chemicals. Then both the PEEK tube and the PTFE membrane are covered using a perforated PEEK rod with a centrally bore hole [74].

Fiber Optic Swellable Polymeric Sensor Technology: The fiber optic swellable polymeric sensor as reported in [74] consists of hydrogel rod, an optic fiber and a device to cause micro bending of the fiber. Hydrogel swells in presence of water. Considering the sewer applications, PVA is used, which is resistant to grease, oil and solvents. A helically twisted thread is used for micro bending. It covers both the PVA hydrogel and the optical Single Mode fiber. As the PVA swells in the presence of water, it presses the optical single-mode fiber against the helically twisted thread leading to attenuation of light transmitted through fiber. The light attenuation was measured using a power meter. The swellable polymeric fiber optic sensor is covered with felt wick for extending the area of exposure to water.

Discussion: In general, fiber optic sensors have the advantages of electrical passivity, easier in multiplexing and remote operability. There is a considerable amount of research

work carried out relating to this technology including several US patents [91]. The research work by Grattan et al (City University London) is significant in this domain and they have used both the FBG based humidity sensor and a swellable polymer fiber optic sensor in sewerage tunnel leakage detection [74]. FBG humidity sensors are placed at the bottom side of the joints and the swellable polymer fiber optic sensor is laid near the inner side of the sewerage pipe. It is invasive and needs significant infrastructure modifications; may be more suitable for new sewer pipes. The quantity measured is not a direct measure of the surface moisture content and it can be affected by other factors such as shrinkage, thermal strain and diffusivity of the concrete [92]. The response time of the sensor given in the [74] is 30 minutes which may be another concern, although it is mentioned that the sensitivity and the response time can be optimized by changing the coating thickness [93]. In a similar US patented humidity sensor document [91], it is mentioned that the sensor takes longer time for low to high humidity transitions than that of high-to-low transitions.

3.2.1.9 Micro Electro Mechanical Systems Sensors

With the development of MEMS technology, capacitive and cantilever type sensors became a reality. They have a small form factor, cheaper and provide fast responses.

Technology: Both the capacitive type and cantilever type sensors use thermoset polymer coating to detect water vapour [94]. In the former type, polyamide or cellulose acetate polymer thin films are deposited in between conductive electrodes. The absorption of moisture causes the dielectric constant of the material to change providing a measure for exposed humidity. The design may involve a porous top metal sheet for allowing the moisture to reach the polymer. In the latter, polyimide is spin coated on cantilever beams. Once the polyimide is exposed to humidity (water), the film expands introducing strain in the structure. Strain gauges are used to measure it and hence the humidity in the environment can be estimated.

Discussion: The sensors are reasonably priced and provide reliable responses. They are low power devices which have lots of potential in industrial applications. However, they are not tested in sewers. It is anticipated that the sensors have challenges due to the need for exposure of the thin polymer film to the hostile sewer environments. This in

turn causes the sensor degradation due to the deterioration of the polymer and blockage of moisture transmission from reaching to the polymer due to foreign particles those can deposit in sewer environments.

3.2.1.10 Hyperspectral Sensing

Human vision can only see a very limited band (approximately 390nm to 700nm) in the electromagnetic spectrum. Hyperspectral cameras are able to sense a much wider range in the electromagnetic spectrum. Therefore, it has been used in many applications including, remote monitoring, agricultural and biomedical and military applications [95–99].

Technology: This technology works like an advanced camera. A visual camera captures only three wavelength bands (for example, red, green and blue). In contrast, multispectral cameras capture several bands of information [100, 101]. The most advanced version, which is the hyperspectral camera captures both spectral and spatial data. The light entered into the camera is dispersed to different wavelengths by the spectrograph. The dispersed light is then incident on a CCD sensor capturing spatial and spectral information. However, it is to be noted that the input light is only a line as opposed to a scene in a visual camera. Such information is captured by either moving the camera or object movement.

Discussion: The hyperspectral sensors have been used in soil moisture monitoring [102]. However, there are no reported work on the application of them in sewers to detect the amount of surface moisture. The sensor has limitations in sewers due to harsh prevailing conditions such as extremely high humidity. Although this could be used for detecting the presence of moisture, estimating the amount of moisture is a challenging task.

3.2.2 Feasibility

This section indicates the feasibility aspects of the sensing devices to be used to measure surface moisture conditions in the sewer system. The section short lists the potential sensing solutions. The criteria for short-listing includes the technical aspects, cost and non-invasive approach. Table 3.1 presents the feasibility analysis for comparing the previously discussed surface moisture measurement modalities.

Feasibility Analysis: Comparison of surface moisture measurement modalities			
Technology	Non-invasive (Yes/No)	Feasibility (Yes/No)	Comments
Gravimetric methods	-	Yes	Can be used in very high moisture contents. Several measurements and hence several core samples are needed for improving reliability. Provides the moisture content of the whole sample. May be used for validation purposes.
Gamma densitometry	Yes	No	Moisture profile can be obtained. This is bulky and expensive, most suitable for lab environments. Practically challenging in sewers.
Electrical resistivity	Yes	Yes	Non-invasive and contact type. Needs on-site calibration.
Capacitive sensors	Yes	No	Need on-site calibration and can be affected by foreign particles (vapor).
Resonator based sensors	Yes	No	Compromise between the depth of penetration and attenuation. Nuclear reactor based sensors are possible, however, they are very restricted and expensive.
TDR based sensors	No	Yes	Invasive, need calibration and can be affected by the temperature variations and distribution of the moisture.
FDR based sensors	No	Yes	Invasive, need calibration, faster and less complex compared to TDR.
Fiber optic sensors	No	Yes	Invasive and need to be mounted along the infrastructure, could be challenging in sewers due to chemicals and other foreign matter.
MEMS sensors	Yes	No	Challenging to use in sewers due to the need of exposure the thin film to the hostile sewer environments.
Hyperspectral sensing	Yes	No	High humidity can affect the response, presence of moisture may be possible, however estimation of level of moisture may be very challenging.

TABLE 3.1: Feasibility: Comparison of surface moisture measurement modalities.

3.2.3 Concluding Remarks

From the scoping study, it is concluded that electrical resistivity based surface moisture sensing as a potential solution. This measuring technique will be utilized in developing the moisture sensor suite.

3.3 Experimental Evaluation to Study the Behaviour of Concrete Moisture with Electrical Resistance and pH Conditions

In this section, the behaviour of concrete moisture with electrical resistance and the effects of pH concentrations on the concrete are studied.

3.3.1 Experimental Approach

3.3.1.1 Concrete Sample Preparation

A total of 10 concrete samples were used for two sets of experiments. All the concrete samples were dried using a microwave oven and were left to cool for 5 hours at room temperature of 25°C and each sample had dimensions of 20x10x5 cm^3. After cooling, the mass of each concrete sample in dry condition denoted as m_d was recorded and the readings were recorded in Table 3.2. Then, each concrete sample was placed in a 7-litre container and submerged in different aqueous solutions having different pH values and were left for 15 days. The wet concrete samples were removed from the containers and excess liquid on concrete surfaces were soaked out gently using a paper towel before the mass of each concrete sample in wet condition denoted as m_w was recorded. The recorded readings are shown in Table 3.3.

Experimentation-1		**Experimentation-2**	
Concrete Number	m_d **(g)**	**Concrete Number**	m_d **(g)**
1	2211.4	6	2222.8
2	2137.5	7	2207.3
3	2187.7	8	2145.7
4	2163.8	9	2130.4
5	2160.4	10	2150.1

TABLE 3.2: Mass of concrete samples in dry condition.

Experimentation-1		**Experimentation-2**	
Concrete Number	m_w **(g)**	**Concrete Number**	m_w **(g)**
1	2275.8	6	2279.3
2	2219.2	7	2290.7
3	2264.5	8	2216.0
4	2250.2	9	2209.6
5	2241.4	10	2217.4

TABLE 3.3: Mass of concrete samples in wet condition.

3.3.1.2 pH Measurements

It is known that the surface pH is an indication to initiation of the corrosion process. As mentioned in [19], the rate of acidification has been a strong function of pH concentration. In [15], it was specified that the neutrophilic bacterial colonization happens when the concrete surface pH falls approximately to 9 and the activity of acidophilic bacteria lowers

the concrete surface pH to values around 2. The pH indicator strips were used to determine the concentration levels of different solutions. Concrete samples were numbered from 1 to 10 and Table 3.4 summarizes how concrete samples were immersed in solutions having different pH values.

Concrete samples in different pH value of solutions					
pH value of solutions	2	5	7	8	9
Concrete Number	1,6	2,7	3,8	4,9	5,10

TABLE 3.4: Concrete samples in different pH value of solutions.

3.3.1.3 Moisture Measurements

The concrete samples were taken out from the solutions to determine their moisture content. The surfaces of the concrete samples were soaked with a paper towel gently to avoid erroneous readings before the masses of concrete samples were recorded on weighing scale (OHAUS SP-6001), which had a precision of 0.1 gram.

By using the gravimetric method, the determination of wet basis moisture content θ_G of a material can be defined as in Equation 3.1 and the volumetric moisture content θ_V of the material can be determined by using the formula in Equation 3.2 as given by [83]. Both θ_G and θ_V are expressed in terms of %.

$$\theta_G = \frac{m_w - m_d}{m_d} \times 100 \tag{3.1}$$

$$\theta_V = \frac{\rho_d}{\rho_w} \times \theta_G(\%) \tag{3.2}$$

where m_w is the mass of the concrete sample in a wet condition, m_d is the mass of the concrete sample in a dry condition, ρ_w is the density of pH solution and ρ_d is the density of concrete sample in a dry condition, which can be defined as in Equation 3.3. ρ_d is expressed in terms of g/cm^3.

$$\rho_d = \frac{m_d}{volume} \tag{3.3}$$

where the volume of each concrete sample was calculated to be 1000 cm^3. When the bottom surface of a concrete sample was exposed to the solution having neutral pH=7, the time of arrival of moisture at different depths of a concrete sample was measured and the readings were presented in Table 3.5.

Depth profile of moisture penetration inside concrete					
Depth (cm)	0.5	1.0	1.5	2.0	2.5
Time of arrival of moisture (Hours)	24	60	120	216	360

TABLE 3.5: Depth profile of moisture penetration inside concrete.

Since the arrival of moisture from the exposed surface was about 2.5 cm in depth, the new volume of the concrete sample was calculated to be approximately 500 cm^3. Therefore, the ρ_d of concrete samples were calculated using Equation 3.3 and presented in Table 3.6. The ρ_w of concretes are presented in Table 3.7.

Experimentation-1		**Experimentation-2**	
Concrete Number	ρ_d **(g/cm^3)**	**Concrete Number**	ρ_d **(g/cm^3)**
1	4.4228	6	4.4456
2	4.2750	7	4.4146
3	4.3754	8	4.2914
4	4.3276	9	4.2608
5	4.3208	10	4.3002

TABLE 3.6: Density of concrete samples in dry condition.

Experimentation-1		**Experimentation-2**	
Concrete Number	ρ_w **(g/cm^3)**	**Concrete Number**	ρ_w **(g/cm^3)**
1	0.960	6	0.960
2	0.980	7	0.980
3	1.000	8	1.000
4	1.025	9	1.025
5	1.030	10	1.030

TABLE 3.7: Density of pH solution.

3.3.1.4 Electrical Resistance Based Sensor System

A sensor system for moisture sensing application was newly designed and fabricated in this work. The measurement of electrical resistance between two sensing electrodes determines the electrical conductivity, which is a property of concrete material [103]. The newly designed sensor system works on the principle of sensing electrical resistance changes through electrodes that are in contact with the surface of interest. The measured electrical resistance data is used to infer volumetric concrete moisture content and thus, the system behaves as a resistance-based moisture sensor. All the experiments on concrete samples were conducted in CAS Robotics Research Laboratory located at UTS.

The sensor system includes two electrodes that are made up of conductive carbon steel and plated with zinc for corrosion protection, a microcontroller board comprising of ATmega328 microcontroller having 8-bit AVR, a data logger comprising 8GB Ultra HDSC memory and 12V DC power source. The entire system was enclosed in IP65 rated housing allowing only electrodes to be in contact with the concrete as in Figure 3.1.

The resistance sensor circuit used by the sensor system consists of a voltage divider with non-inverting operational amplifier (op-amp) and Analog to Digital Converter (ADC). Figure 3.2 shows the resistance sensor circuit.

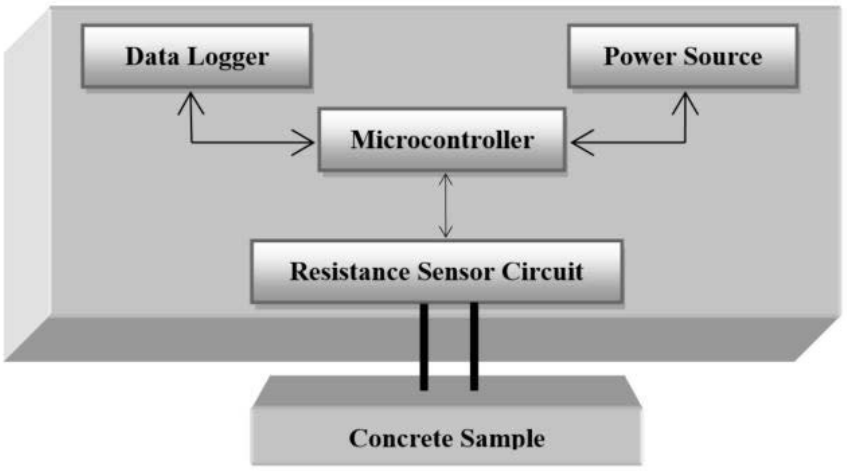

FIGURE 3.1: Functional block diagram of the sensor system.

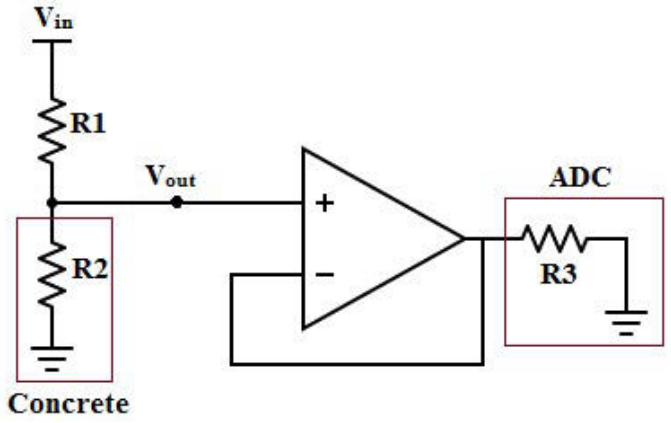

FIGURE 3.2: Resistance sensor circuit.

The resistance sensor has an input DC voltage V_{in}=3.3V. The resistance R1 was analytically estimated as R1=510 kΩ. The resistor R2 gives the measure of electrical resistance changes of the concrete sample. Due to the low impedance of ADC compared to the resistance of concrete, a non-inverting op-amp under unity gain was used to buffer the voltage between the circuit and ADC. The output voltage V_{out} of the circuit as shown in Figure 3.2 was computed by using Equation 3.4. Upon simplifying and rearranging Equation 3.4, the unknown resistance R2 that gives the measure of concrete resistance was obtained by using Equation 3.5.

$$V_{out} = V_{in} \times \frac{R2}{R1 + R2} \tag{3.4}$$

$$R2 = R1 \times \frac{1}{\left(\frac{V_{in}}{V_{out}} - 1\right)} \tag{3.5}$$

The alternative sensor circuit can be Wheatstone bridge circuit for determining the unknown resistance (concrete resistance). For a given concrete, the changes of moisture content can be monitored by sensing electrical resistance variations of the material. However, the resistivity is usually affected by the type of cement and water-cement ratio [104]. Higher the porosity of the material, the resistivity measurements will be lower mainly because of less material interfering with current passing through it [81]. Due to ion transport through the pore solution, the electrical conduction occurs and it is dependent on both pore solution conductivity and porosity [105]. Likewise, when the concrete material is more porous, it can hold more water content, i.e., it can increase the volumetric measure with more moisture. The porosity also reflects on the surface of a material as it interferes with current passing through a material. Therefore, it can hold more water content when the surface is more porous and so it reflects on low surface resistivity measurements.

3.3.2 Data-driven Approach for Predicting Moisture Content

This section describes the data-driven approach for predicting the volumetric moisture content of concrete using Gaussian Process Regression (GPR). Estimating volumetric moisture content from electrical resistance and pH measurements can be formulated as a non-linear regression problem. Gaussian Process (GP) models are an effective tool to resolve such regression problems. GP modelling approach [106] was used in this work to train a non-parametric model, which obtains resistance (R) and pH (ph) values as inputs and predicts the percentage volumetric moisture content (mc). The intention is to learn a function f in the form of

$$mc = f(R, ph) + \xi \tag{3.6}$$

where ξ is the uncertainty, adapting the GP approach used in [107] learn a similar function. The adaptation of the GP approach is described from here on in.

Let $[X, Y]$ be the training data set where $X = [x_1, x_2, x_3, ..., x_m]^T$, $x_i = [R_i \ ph_i]^T$, and $i(1 \leq i \leq m)$ is an integer and m is the number of captured data pairs. $Y = [y_1, y_2, y_3, ..., y_m]^T$ is a vector containing corresponding training targets where $y_i = mc_i$. Similarly, $[X^*, Y^*]$ will be testing data where $X^* = [x_1^*, x_2^*, x_3^*, ..., x_n^*]^T$ is a matrix containing testing inputs and $Y = [y_1^*, y_2^*, y_3^*, ..., y_n^*]^T$ is a vector containing predicted outputs corresponding to X^*. Once f has been learned using $[X, Y]$, f can be used to predict Y^* for a given X^* as shown in Equation 3.7

$$mc^* = f(R^*, ph^*) + \xi^* \tag{3.7}$$

To apply the GP framework to this non-linear regression problem, a kernel $K(X, X)$ having elements given by $k_{i,j} = k(x_i, x_j)$ has to be selected. This specifies the kind of functions that are expected before any data have been seen. Technically, the kernel places a prior likelihood on all possible functions. After evaluating a number of commonly used kernels, the squared exponential kernel was chosen for this work. It is defined as in Equation 3.8.

$$k(x_i, x_j) = \alpha^2 exp\left\{ -\frac{1}{2\beta^2} \left\| x_i - x_j \right\|^2 \right\} \tag{3.8}$$

where the α and β represent the hyper-parameters. The GPR model was trained by minimizing the negative log marginal likelihood in Equation 3.9 with respect to $\theta = \{\alpha, \beta, \sigma_n\}$. The covariance function denoted by $\sum$ in Equation 3.9 is expressed in Equation 3.10.

$$-\log p(Y|X, \theta) = \frac{1}{2} Y^T \Big(\sum \Big)^{-1} Y + \frac{1}{2} \Big| \sum \Big| + \frac{m}{2} \log(2\pi) \tag{3.9}$$

$$\sum = K(X, X) + \sigma_n^2 I \tag{3.10}$$

The basic Gaussian Process Regression model equations are given by Equation 3.11 and Equation 3.12.

$$(\mu)^* = K(X^*, X)\big\{K(X, X) + \sigma_n^2 I\big\}^{-1} y \tag{3.11}$$

$$\Big(\sum\Big)^* = K(X^*, X^*) + \sigma_n^2 I - \big\{K(X^*, X)K(X, X) + \sigma_n^2 I\big\}^{-1} K(X, X^*) \tag{3.12}$$

The predicted volumetric moisture content (Y^*) for the testing input vector (X^*) thus will be given by the mean of the posterior distribution $(\mu)^*$ and the associated uncertainty will be given by the covariance $(\sum)^*$.

3.4 Sensor Development and Pre-deployment Evaluation

The experimental evaluation conducted in the previous section demonstrated the variations of electrical resistance based on the concrete moisture. Following that, this section describes the sensor development for real-time measurements inside sewer pipes under hostile conditions. The surface resistivity of the concrete material can be measured by placing the resistivity meter on the surface of interest. In this work, commercially available resistivity meter is utilized (Resipod, Proceq), which is shown in Figure 3.3A.

The sensing principle of the resistivity meter used in the sensor development is based on the Wenner method. This technique uses four electrodes positioned in a straight line with an equidistant space between the electrodes as shown in Figure 3.3B. A current is applied to the outer two electrodes that are in contact with the concrete surface and the resultant potential difference is measured across the two inner electrodes. Based on the ratio of the injected current and the measured voltage, electrical surface resistivity can be determined. However, the measured resistivity is dependent on the distance between the electrodes. Mathematically, the resistivity can be computed by using Equation 3.13:

$$\rho = 2\pi a\Big(\frac{V}{I}\Big) \tag{3.13}$$

(A) [108]

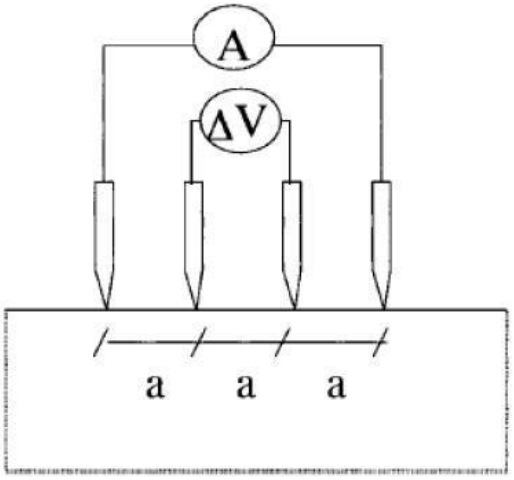

(B)

FIGURE 3.3: Surface resistivity measurement. (A) Commercial resistivity meter from Proceq (B) Wenner method to measure surface resistivity.

where ρ is the resistivity of the concrete material expressed in terms of kΩcm, $a = 50$mm is the distance between the electrodes, V is the electrical potential difference measured by the inner two electrodes and I is the current injected by the outer two electrodes.

Based on the resistance of the concrete material, the resistivity meter automatically changes its current injection mode through outer electrodes. In general, the device tries to inject full 200μA current into the concrete. However, if the concrete material has high resistance, it injects 50μA or if that is not likely to happen because of very high resistance, it injects less than 50μA.

The resistivity meter has an in-built non-volatile memory unit, where 500 measurement values can be stored. In order to utilize the sensor for long-term operations, it is required to have more memory for storing the real-time measurements. For this reason, an ODROID based data logger was developed by establishing the data connectivity between the resistivity meter and storage unit.

A sensing unit was designed to allow only the electrodes of the resistivity meter outside the sensor enclosure in order to be in contact with the concrete surface. The electrodes of the resistivity meter uses spring mechanism, so that the electrodes can be on contact with the concrete surface even in case of concrete surface being not flat (rough). The key specifications of the resistivity meter is shown in Table 3.8.

Key Specifications: Resistivity Meter	
Range	0-2000 kΩcm
Frequency	40 Hertz
Resolution (nominal current 200μA)	±0.2 kΩcm
Resolution (nominal current 50μA)	±2 kΩcm
Resolution (nominal current <50μA)	±2 kΩcm
Operating temperature	0°C to 50°C
Storage temperature	-10°C to 70°C
Input power	5V, 100mA

TABLE 3.8: Specifications of the resistivity meter.

Although, the resistivity meter has its application for infrastructure monitoring, it is not proclaimed to use in confined sewer systems. Therefore, pre-deployment evaluation was conducted before deploying it in sewer systems. This evaluation focusses on the measurement capabilities of the resistivity meter to determine the reproducibility and limit of detection. The evaluation was carried out by placing the resistivity meter on the benchmark and taking repeated measurements.

3.5 Field Application for Real-time Measurements of Surface Moisture Conditions

This section describes the sensor suite deployment in sewer pipe for real-time measurements of surface moisture conditions. Then, the section elucidates the sensor data collection and on-site calibration procedure.

3.5.1 Sensor Suite Deployment

After developing the sensor suite in the laboratory, it was deployed at Sydney Water based sewer at Thornleigh suburb of Sydney city, Australia during the summer season. The sensor suite consists of sensing unit and monitoring unit. The sensing unit was installed near the crown of the confined concrete sewer pipe on 3rd November 2017 and the monitoring unit was constructed outside the sewer pipe to set up the access station. Figure 3.4 shows the installation of the sensing unit inside sewers and the access station set up outside the sewer pipe.

Besides the electrical resistivity based moisture sensor, the sensing unit accommodates an infrared radiometer and a thermistor sensor for measuring the surface temperature variations on the concrete sewer. The moisture sensor was activated to measure the surface resistivity of concrete sewer on 10th November 2017. The sensing unit was mounted on the sewer pipe in a way such that the electrodes are in contact with the concrete surface, so that surface measurements are attained. From the sensing unit, the signals from the moisture sensor were transmitted to the access station by using an Ethernet cable.

In the access station, the transmitted signal from the moisture sensor was processed and data logged by using an ODROID based Single Board Computer (SBC). The SBC used in the proposed application was ODROID-XU4. It is a 16GB embedded multimedia controller module with pre-installed Linux computing and small form factor having a dimension of 82x58x22 mm^3. The incoming digitalized signals from the moisture sensor were decoded from binary format to hexadecimal format. The on-board operating system of the SBC in the access station was programmed using Python programming language to perform

(A)

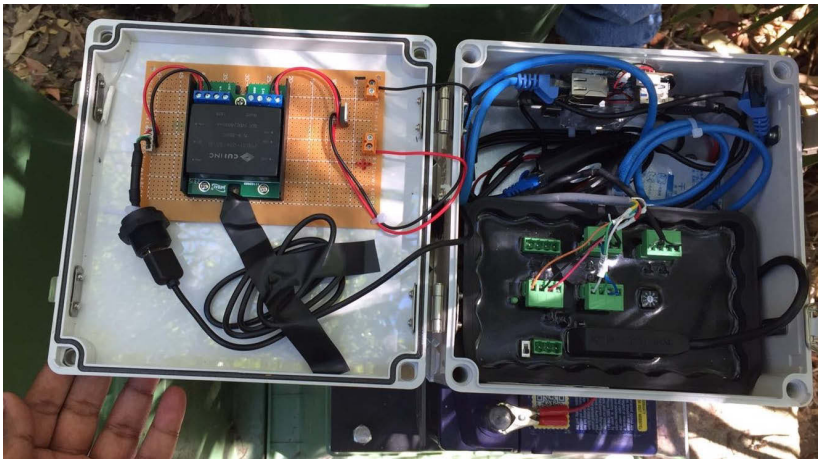

(B)

FIGURE 3.4: Moisture sensor deployment. (A) Sensing unit near the crown of the concrete sewer pipe (B) Monitoring unit of the access station constructed outside the sewer pipe.

surface resistivity measurements at an interval of one hour in hour boundaries. From the SBC at the access station, the logged surface resistivity measurements with the time-stamp can be downloaded in the form of a text file (.txt).

The field site used for sensor evaluation was located in a remote area, where there is no access to electrical mains. In order to overcome this issue, the access station was designed to operate by using battery power. The SBC in the access station was powered by using a 12V 100Ah rechargeable heavy duty battery. The constructed access station was not equipped to communicate the measured data remotely and so, once in a week an operator goes to the access station to check the operating conditions of the sensor and data logging facilities whilst swapping the batteries with fully charged ones. Every time, the operator swaps the batteries, the SBC was rebooted and restarted to perform data acquisition at

desired time intervals.

Other sensors that measure the surface temperature of the concrete sewer pipe and ambient temperature of the sewer atmosphere were also powered by the batteries in the access station. The data from those sensors were stored by using a data logger (TSM-1, ICT International). All the sensors were monitored from the assess station and were programmed to perform measurements at hour boundaries. All the cables transmitting measured data signals were protected from the sewer vermins by enclosing with electrical conduit from the sensing unit to access station. This field deployment application was carried out for about three months and both the sensing unit and monitoring unit in the access station were removed from the site on 7^{th} February 2017. The H_2S levels during the field evaluation were approximately ranging between 2-5ppm.

3.5.2 Field Data Collection and On-site Calibration

The free water retained on the surface of the aggregate particles and considered to be part of mixing water in concrete is known as surface moisture [109]. Depending on the moisture content, the concrete material behaves either as an insulator or a conductor. From various studies including [40, 41, 110, 111], it has been proven that the electrical resistivity of the concrete decreases when the moisture increases and vice-versa. Therefore, the surface electrical resistivity measurement is said to have a strong function of surface moisture. In this study, we aim to indicate the moisture on the concrete surface of the sewer pipe. The electrical resistivity sensor employed in this study was calibrated on the field site by placing the sensor and taking resistivity measurements in dry and wet surface areas. The measurement from the dry surface area was 360 kΩcm and from the wet surface area, the measurement was 16 kΩcm. The surface electrical resistivity measurements range from 360 kΩcm to 16 kΩcm was considered to be 0% to 100% surface moisture range. Besides surface resistivity data measurements, the surface temperature of the concrete sewer pipe and ambient temperature of the sewer atmosphere was synchronously measured.

3.6 Post-deployment Validations of the Moisture Sensor After Long Exposure to Hostile Sewer Condition

A post-deployment validation study was conducted in the laboratory conditions following the three months of field evaluation in hostile sewer environment. In this study, the sensing capabilities of the moisture sensor and the robustness of the enclosure were investigated. By using the benchmark, the sensing capabilities of the moisture sensor were evaluated by taking repetitive measurements. Then, MAPD was used as a statistical metrics to compute the percentage error between the sensor measurements and benchmark. Further, the sensor enclosure and the sensor electrodes were examined through careful visual inspection to identify any deteriorations occurred during the field evaluation.

3.7 Locating the Rebar Orientation using Electrical Resistivity Measurements

This section presents a machine learning model for locating orientation of the reinforcing bar (rebar) inside the concrete in order to optimally place the sensor for surface moisture measurements.

3.7.1 Data Collection

In this section, data was collected by using a resistivity meter that was developed in the laboratory. This device performs measurements based on the Wenner method similar to the one deployed inside sewers. This device is compact and works on the open-source electronic prototyping platform (Arduino Nano). The main difference between the developed unit and sewer deployed unit is the distance between the electrodes. The new unit has a distance of 4 cm and whereas the other has 5 cm. The newly developed resistivity meter was evaluated on the benchmark scale and it produced measurements as desired. More information on the development of this resistivity meter is available in [112]. A concrete of thickness: 10 cm, width: 35 cm and length: 35 cm was made with a rebar width: 1.2

cm, height: 1.2 cm and length: 30 cm was embedded into the concrete material at a 2 cm depth from the top surface of the concrete. This concrete was divided into several cells to perform measurements in those cells. Totally, the concrete was partitioned into 49 cells and each cell have a dimension of 4cm^2. The rebar runs through the column 4 of the (7×7) partitions.

Electrical resistivity measurements in each cell were obtained by placing the inner two electrodes of the sensor at different angles such as 0°, 30°, 45°, 60° and 90°. The 0° position is perpendicular to the rebar and 90° position is parallel to rebar. For each angle, two sets of data was taken in each cell, which makes two datasets for each angle. From the 49 cells, only 20 random cells data were used to implement the GMRF for spatial estimation and remaining 29 cells were used for testing purpose.

3.7.2 Spatial Estimation using Gaussian Markov Random Fields

This subsection presents the Gaussian Markov Random Fields (GMRF) for spatial estimation and thereby determine the orientation of the embedded rebar inside the concrete. The proposed machine learning method is a computationally efficient alternative to the non-parametric Gaussian Process (GP) based models. The computational advantages coming from the sparsity of the precision matrix, an inverse of a dense covariance matrix, whose zero elements relate directly to conditional independence assumptions. This salient feature of the precision matrix motivates this work to employ GMRF model [113].

3.7.2.1 Gaussian Markov Random Fields

GMRF is a discretely indexed Gaussian Field, which is achieved through the observations of random variables in the spatial process [106, 113]. It incorporates Gaussian Processes and also satisfies Markovian property [114]. This makes GMRF a computationally efficient alternative to Gaussian Processes [115].

Let $s = (s_1, s_2, s_3, ..., s_n)^T$ with $s \sim \mathcal{N}(\mu, Q^{-1})$ referring to GMRF given by the mean μ and a symmetric and positive definite precision matrix Q that represents the convex

polytope in $\mathbb{R}^d$ ($\mathbb{R}$ denotes real numbers and d is the polytope), and an inverse of the Gaussian Process covariance matrix, $\sum$ [113, 116]. So, the density of s will be of the mathematical form given in Equation 3.14:

$$p(s) = (2\pi)^{-\frac{n}{2}} \Big(det(Q)\Big)^{\frac{1}{2}} exp\Bigg\{ -\frac{1}{2}(s-\mu)^T Q(s-\mu) \Bigg\} \tag{3.14}$$

The salient feature of the Markovian property is that the full conditional distribution of s_i ($i \leq i \leq n$) is only dependent on the elements set of the neighbourhood structure of the process and it is given by Equation 3.15

$$p(s_i|s_{-i}) = p(s_i|s_{Ni}) \tag{3.15}$$

where s_{-i} represents the elements in s apart from the element s_i, and s_{Ni} denotes the neighbourhood elements of s_i. Therefore, it is established that in the case of given neighbourhood elements, s_i element is independent on all other elements in s with the exception of the element s_{Ni}, which defines the conditional independence as $s_i \perp s_{-i,Ni}|s_{Ni}$ ($\perp$ denotes the independence of two variables) for $i \leq i \leq n$. According to [114], μ is not related to pairwise conditional independence properties of s and therefore, afore stated characteristic is limited to the precision matrix Q. Generally, if s_i and s_j are conditionally independent, $s_i \perp s_{-j}|s_{-i,j}$ is equivalent to $Q_{ij} = 0$. This condition give rise to $Q_{ij} \neq 0$ when $j \in \{i, N_i\}$ and deduce the sparsity of Q that results significantly in computation performance.

3.7.2.2 Spatial Field Model by way of Gaussian Markov Random Fields

Let the finite set of spatially observed locations be $\psi = (\psi_1^T, \psi_2^T, \psi_3^T, ..., \psi_n^T)^T$. Each spatially observed location in ψ comprise of one electrical resistivity measurement data and consider $x(\psi) = (x(\psi_1), x(\psi_2), x(\psi_3), ..., x(\psi_n))^T$ as the vector of measurements in the spatial field [113]. In this work, the model utilized is similar to [115, 116], which is a summation of a large scale component, a random field and an identically distributed noise. The model is mathematically defined in Equation 3.16:

$$x(\psi) = \zeta(\psi)\beta + s(\psi) + \epsilon(\psi) \tag{3.16}$$

where $\zeta(\psi)\beta = \mathbb{E}(x(\psi))$ is the expectation of $(x(\psi))$ and $\mathbb{E}(\cdot)$ defines the expectation operator. $\zeta(\psi)$ is the covariates determined at spatial location ψ and β is the vector of mean parameters. s is a GMRF with a n zero mean vector and a $n \times n$ precision matrix Q. $\epsilon(\psi)$ is the measurement noise with $\mu = 0$ and a known covariance matrix $\sigma_\epsilon^2 I_\epsilon$ at spatial locations ψ_i $(1 \leq i \leq n)$, where σ_ϵ^2 is assumed to be known and I_ϵ is the identity matrix, $n \times n$.

As in [117], the GMRF can precisely work as a Gaussian Process when the continuous domain Stochastic Partial Differential Equations (SPDE) possess a solution with Matern covariance function [113], which is mathematically given by 3.17.

$$cov(\gamma) = \frac{\sigma^2}{\Gamma(v)2^{v-1}}(\kappa\gamma)^v K_v(\kappa\gamma) \tag{3.17}$$

where γ indicates the Euclidean distance between the spatial locations, $\gamma = \|v_i - v_j\|$. The term σ^2 denotes the marginal variance and the term κ implies spatial parameters with v as the Matern smoothness and K_v represents the modified Bessel function [113]. The term $\zeta(\psi)\beta$, in this case denotes the mean function in the context of Gaussian Process [118, 119].

3.7.2.3 Sensor Data Modelled by GMRF Using SPDE Approach

The SPDE approach formulated by [120] demonstrates computational effectiveness while used in the spatial process. This approach incorporates finite element method [121] to focus the SPDE onto a basis representation, which includes piece-wise linear basis functions described by a triangulation that pertains to the interested regions [113]. Assuming that the spatial process $s(p)$ is observed at N locations where $p = (p_1^T, p_2^T, p_3^T, ..., p_n^T)^T$, then the initial vertices of the triangle are set at those spatial locations. Further, in order to achieve spatial prediction, more vertices of the triangles are added to realize a large triangulation.

The GMRF model is developed on the basis function representation for the given triangulation of the domain Q [113]. Therefore, $s(p)$ is given as in Equation 3.18:

$$s(p) = \sum_{i=1}^{n} f_i(p) w_i \tag{3.18}$$

where $\{f_i(p)\}$ denotes the basis functions that are piece-wise linear on each triangle [113]. In the i^{th} vertex of the mesh, $f_i(p)$ of the functions $\{f_i(p)\}$ is 1 and 0 for all other vertices. The term $\{w_i\}$ denotes the Gaussian distributed weight. At each triangle vertex i, the value of the spatial field is given by $\{w_i\}$ [113]. Thus, the SPDE approach incorporating finite element method establishes the link between the Gaussian Process and GMRF with feasible computation efficacy. The precision matrix Q of size $n \times n$ is determined by computing Equation 3.19:

$$Q = \tau^2(\kappa^4 D + 2\kappa^2 H + H D^{-1} H) \tag{3.19}$$

where τ controls the variance, D and H are the $n \times n$ matrices with $D_{ij} = \langle f_i, f_j \rangle$ and $H_{ij} = \langle \Delta f_i, \Delta f_j \rangle$. The total number of triangulation vertices defines the dimension of Q in the interested region. Thus, Q can be seen as a function of κ and τ. Lets define the hyper-parameter vector as $\Phi = (\log(\tau), \log(\kappa))$. Now, it can be said that the sparse property of Q is embraced by the GMRF representation built by the linear basis functions. The inherent random field at the n vertices of the triangulation is defined by GMRF with μ as

$$s|\Phi \sim \mathcal{N}(\mu, Q^{-1}) \tag{3.20}$$

In the interest of mapping between the basis function representation located at n vertex of the triangulation and random field at resistivity meter locations having N dimension, let us consider the projector matrix as B, whose size is $N \times n$. B projects the modelled inherent random field at the vertices of the triangulation to the data locations.

In reference to the spatial field model presented in the preceding section, the measurements at N locations of the spatial field can be given by Equation 3.21:

$$x|s, \Phi, \beta, \sigma_\epsilon^2 \sim \mathcal{N}(\zeta(p)\beta + Bs, \sigma_\epsilon^2 I_N) \tag{3.21}$$

where $\zeta(p)$ refers to $N \times q$ matrix of covariates, β and Φ are the estimated parameters of the maximum likelihood approach [119], I_N refers the identity matrix $N \times N$. If all the model parameters are learned, the joint distributions of x and s are calculated by adopting the technique in [113, 122], which is given by Equation 3.22:

$$s|x, \Phi, \beta, \sigma_\epsilon^2, B \sim \mathcal{N}\left(\begin{bmatrix} 0 \\ \zeta(p)\beta \end{bmatrix}, \begin{bmatrix} Q^{-1} & Q^{-1}B^T \\ B^T Q^{-1} & \sigma_\epsilon^2 I + BQ^{-1}B^T \end{bmatrix} \right) \tag{3.22}$$

The full conditional distribution of s given by x is also Gaussian with respective to probabilistic theory [113]. By suing block-wise inversion approach [123] and the Schur complement, the Gaussian expressed in Equation 3.22 can be mathematically written as in Equation 3.23:

$$s|x, \Phi, \beta, \sigma_\epsilon^2, B \sim \mathcal{N}\left(\mu_{s|x}, Q_{s|x}^{-1}\right) \tag{3.23}$$

where $\mu_{s|x}$ denotes the vector of posterior means and the term $Q_{s|x}$ denotes the posterior Q. They are given as follows:

$$\mu_{s|x} = \zeta(\psi)\beta + Q_{s|x}^{-1}(\sigma_\epsilon^2 I_N)^{-1}(x - \zeta(p)\beta) \tag{3.24}$$

$$Q_{s|x} = Q + B^T(\sigma_\epsilon^2 I_N)^{-1}B \tag{3.25}$$

Equation 3.24 factorizes the sparse matrix $Q_{s|x}$. However, $Q_{s|x}$ is not dependent on the collection of sensor measurements [113, 116].

3.8 Experimental Results

3.8.1 Experimental Evaluation to Study the Effects of Concrete Moisture with Electrical Resistance and pH

The electrical resistance on the concrete surfaces that were soaked in various pH solutions was measured. The measured resistance data was interpreted with respective volumetric moisture content data for the particular pH solution. It can be observed and clearly evident from the experimental results shown in Figure 3.5 that the electrical resistance measurements increase with a decrease in volumetric moisture content for all the concrete samples and pH solutions from Experimentation-1. The concrete samples that were immersed in pH solutions (pH = 5, 7, 8, 9) tend to show similar trends in moisture content measurements. However, the concrete samples which were under the influence of high acidic solution (pH = 2) show less increase in volumetric moisture content. It may be due to the fact that concrete surface degradation resulting in loss of concrete mass, which was visible from the residues that were present inside the solution container.

The experimental data obtained from all the concrete samples that were used in Experimentation-1 was combined together as the training data input feature for GP modelling. Figure 3.6 shows the input training data in 3D for GP modelling and Figure 3.7 shows the GP predictions in 3D along with the training data from Experimentation-1.

The behaviour of predicted values corresponding to training data is shown in Figure 3.8 along with uncertainties. Data from Experimentation-2 were taken as testing data and the comparison of prediction relative to measured values (testing data) is shown in Figure 3.9. RMSE between prediction and measured volumetric moisture content is 1.44% while the Mean Absolute Error (MAE) is 1.19%.

It can be observed that the GP predicted data and training data fits within the 2σ uncertainty bounds for the Experimentation-1 as it reasonably learns the moisture prediction model. Once the model was evaluated with the testing data from

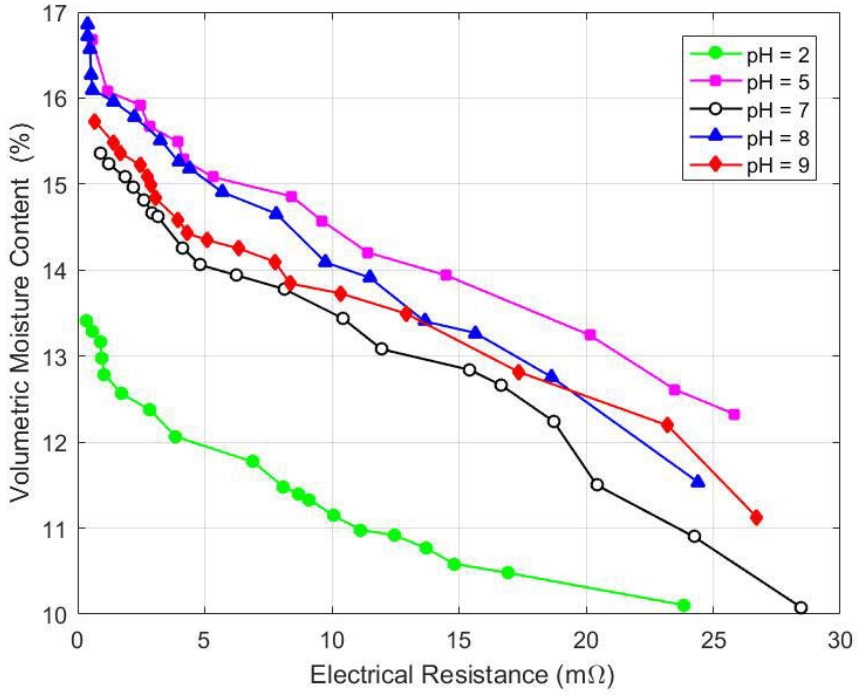

FIGURE 3.5: Electrical Resistance vs. Volumetric Moisture Content.

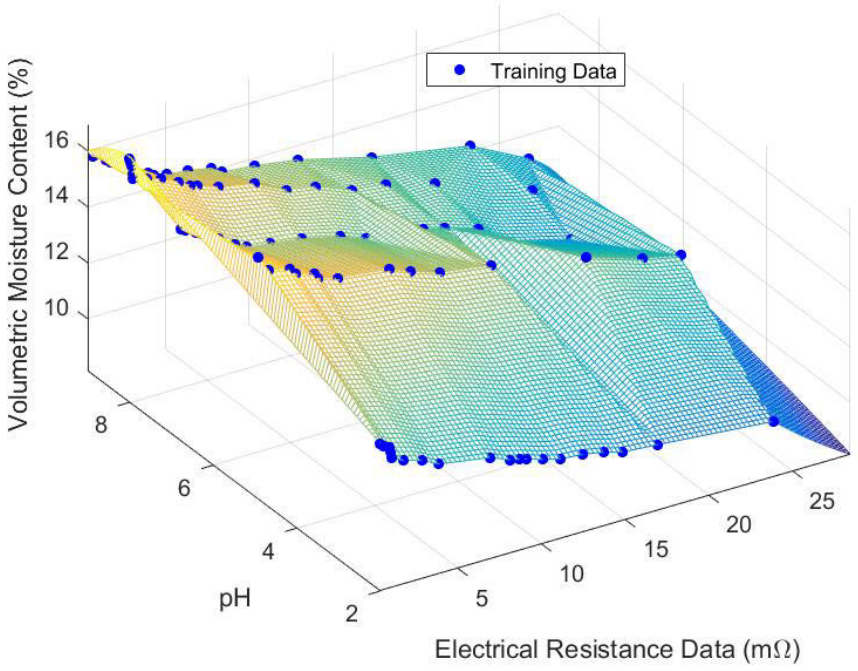

FIGURE 3.6: Learned GP model with training data.

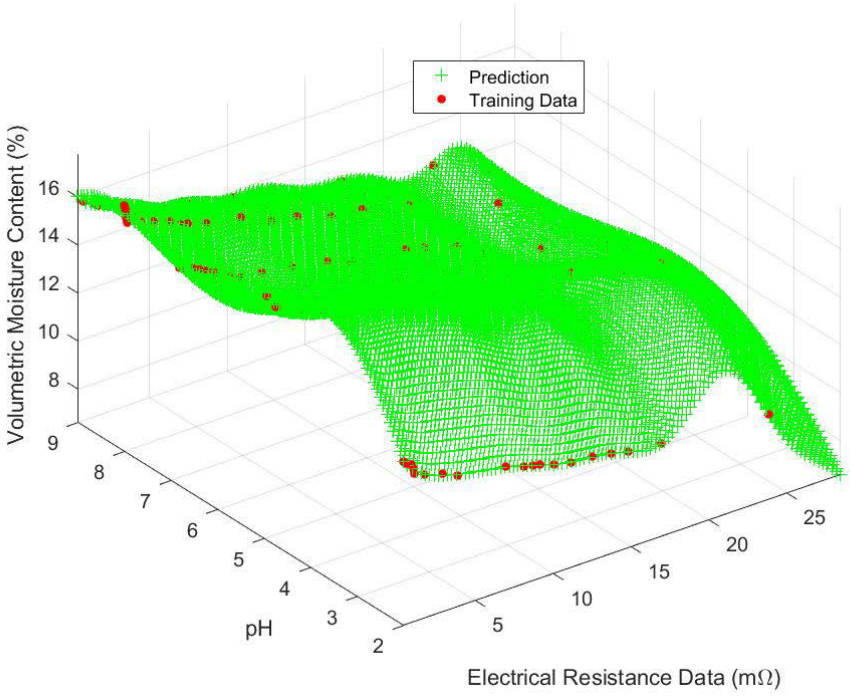

FIGURE 3.7: GP predictions in 3D.

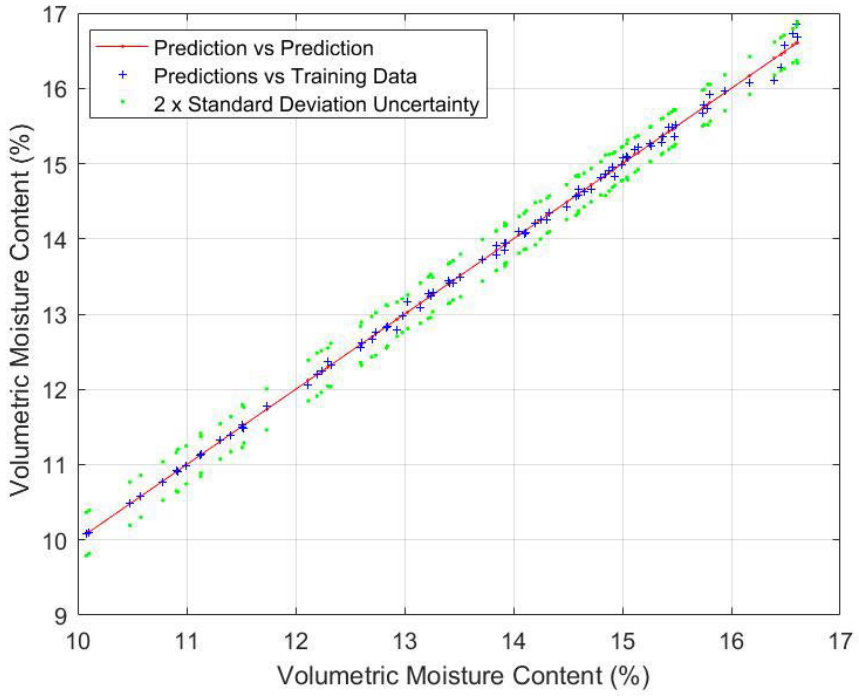

FIGURE 3.8: The behaviour of predicted values corresponding to training data.

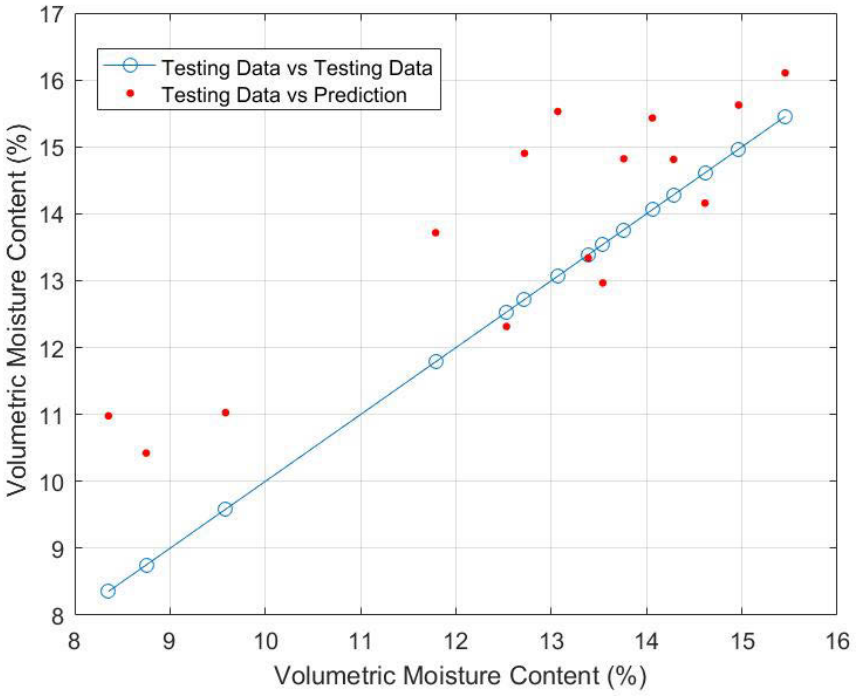

FIGURE 3.9: The behaviour of predictions vs. measured values (testing data).

Experimentation-2, the performance is given in Figure 3.9. There is an RMSE of 1.44% in prediction, which can be due to many reasons. For example, it may be due to the precision of the measuring equipment and also due to human error.

3.8.2 Sensor Development and Pre-deployment Evaluation

By using the electrical resistivity meter, a sensor for sewer deployment was developed and packaged in a PVC material enclosure along with other temperature sensors. The sensor enclosure was designed in a way such that the electrodes of the resistivity meter is in contact with the concrete surface when placed near the crown of the sewer pipe. The accommodation of resistivity meter inside the sensor enclosure is shown in Figure 3.10A and Figure 3.10B displays the electrodes of the resistivity meter for performing measurements on the concrete surface. In order to establish the data transfer between the resistivity meter and the specially made data logger, a USB type B to Ethernet cable was placed inside the sensor enclosure used for transferring measurement data.

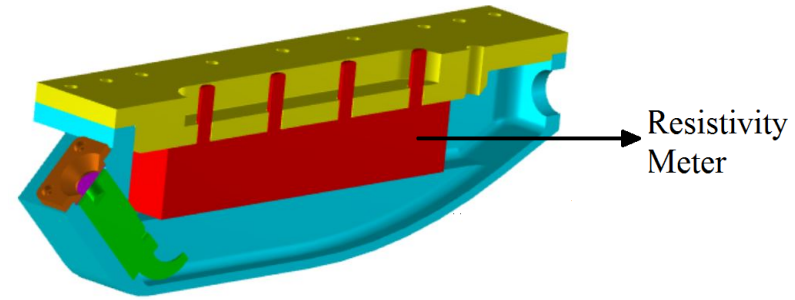

(A)

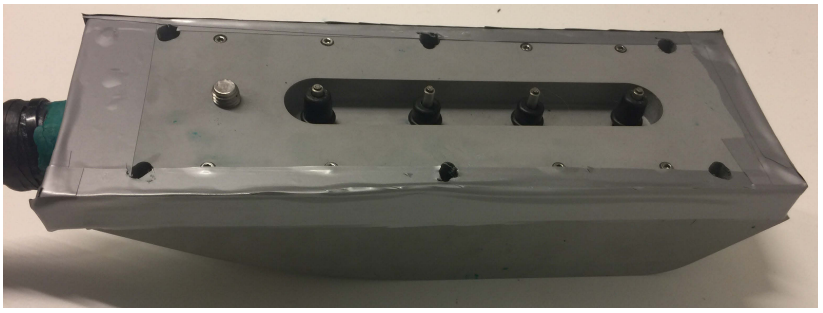

(B)

FIGURE 3.10: (A) Accommodation of resistivity meter inside sensor enclosure CAD model and (B) Sensor enclosure displaying the electrodes of the resistivity meter.

After developing the sensor, pre-deployment evaluation was conducted in laboratory conditions. In this evaluation, the sensor was placed on the benchmark measures of 120 kΩcm and 16 kΩcm to determine the reproducibility. As an outcome of this evaluation, all the measurements were identical to the benchmark measures and therefore, the data reproducibility was 100%. However, if any of the electrodes are not properly in contact with the concrete surface, the measurements showed the value as 0 kΩcm or error. In addition, the resistivity meter has the limit of detection, which is between 0 kΩcm to 2000 kΩcm. Overall, from the pre-deployment evaluation, it can be concluded that the resistivity meter can be deployed inside sewer pipes for measuring the surface resistivity variations of the concrete with the manufacturer settings.

3.8.3 Field Deployment Application

This section presents the experimental results of the field evaluation conducted inside real sewer system.

3.8.3.1 Real-time Sensor Data Showing Temporal Dynamics of Surface Resistivity Measurements from the Sewer Pipe

The surface resistivity variations measured by using the electrical resistivity meter inside the concrete sewer pipe is presented in Figure 3.11. The measurement data was obtained from 10^{th} November 2016 to 20^{th} December 2016 and from 28^{th} December 2016 to 7^{th} February 2017. From Figure 3.11, it can be observed that there are no significant differences of surface resistivity measurements between the days. However, it can be noticed that the diurnal variation pattern relatively varies less than 2 kΩcm. Overall, the surface resistivity data from the resistivity meter displayed a decreasing pattern from the month of November 2016 to February 2017.

3.8.3.2 Effects of Concrete Surface Temperature and Sewer Ambient Temperature Conditions

Figure 3.12 presents the profiles of surface resistivity measurements, surface temperature of the concrete sewer pipe and ambient temperature of the sewer atmosphere for comparative analysis. It can be noticed from Figure 3.12 that the surface resistivity profile in general is having a decreasing trend while the surface temperature profile is showing an increasing trend. This factor is attributed to the reason that increasing temperature of the concrete material increases ion mobility, which results in decreasing the electrical resistivity of the material [124]. In addition, the surface resistivity also showed a decreasing trend while the ambient temperature of the sewer atmosphere showed an increasing trend. This is due to the reason that ambient temperature of the sewer has its influence on the concrete surface temperature. Although both the temperature variables showed a similar trend, there are slight differences in their pattern.

3.8.3.3 On-site Calibration and Surface Moisture Interpretations

In order to determine the surface moisture conditions of the concrete sewer pipe, an on-site calibration was conducted at the end of the field trial evaluation by placing the resistivity

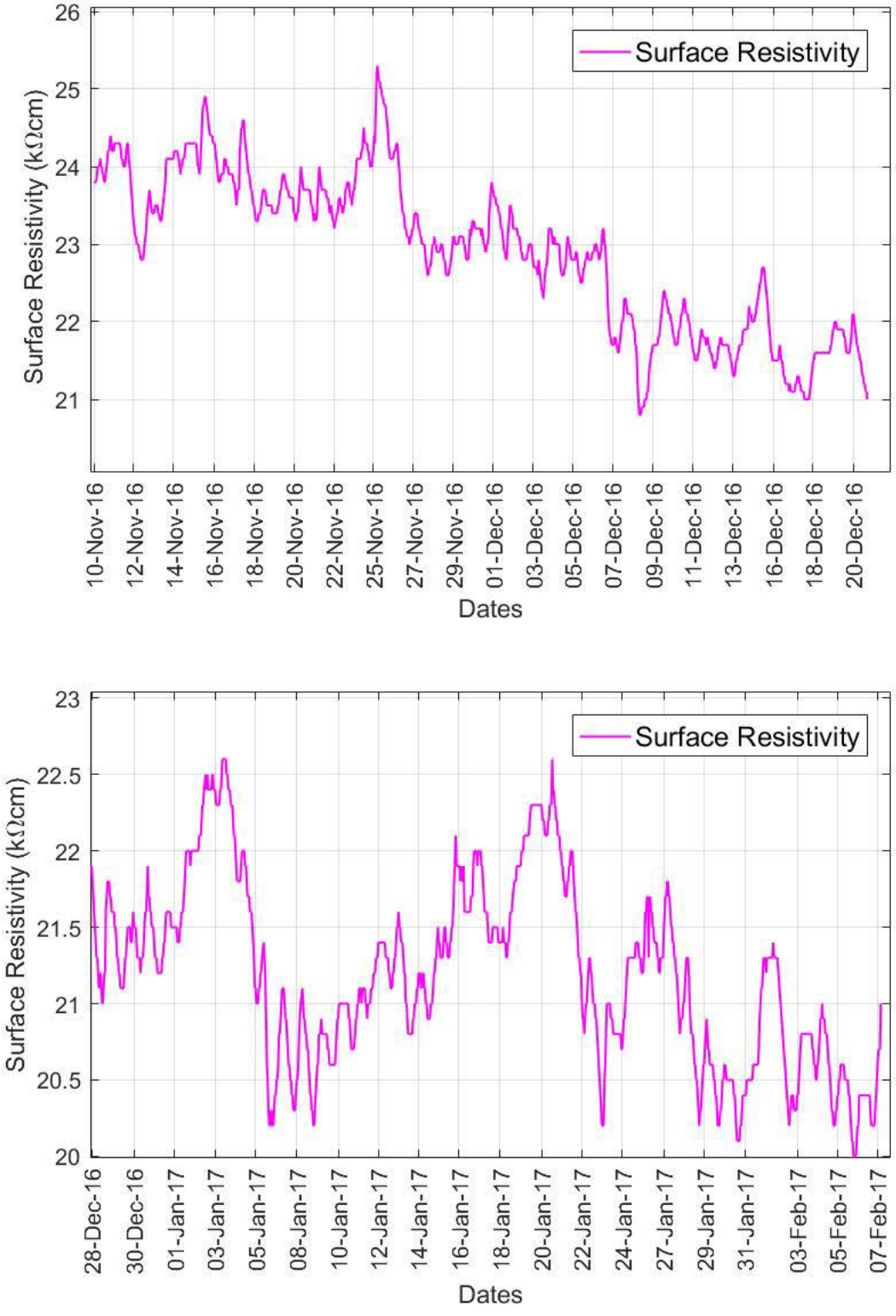

FIGURE 3.11: Surface resistivity profiles obtained from the concrete sewer pipe.

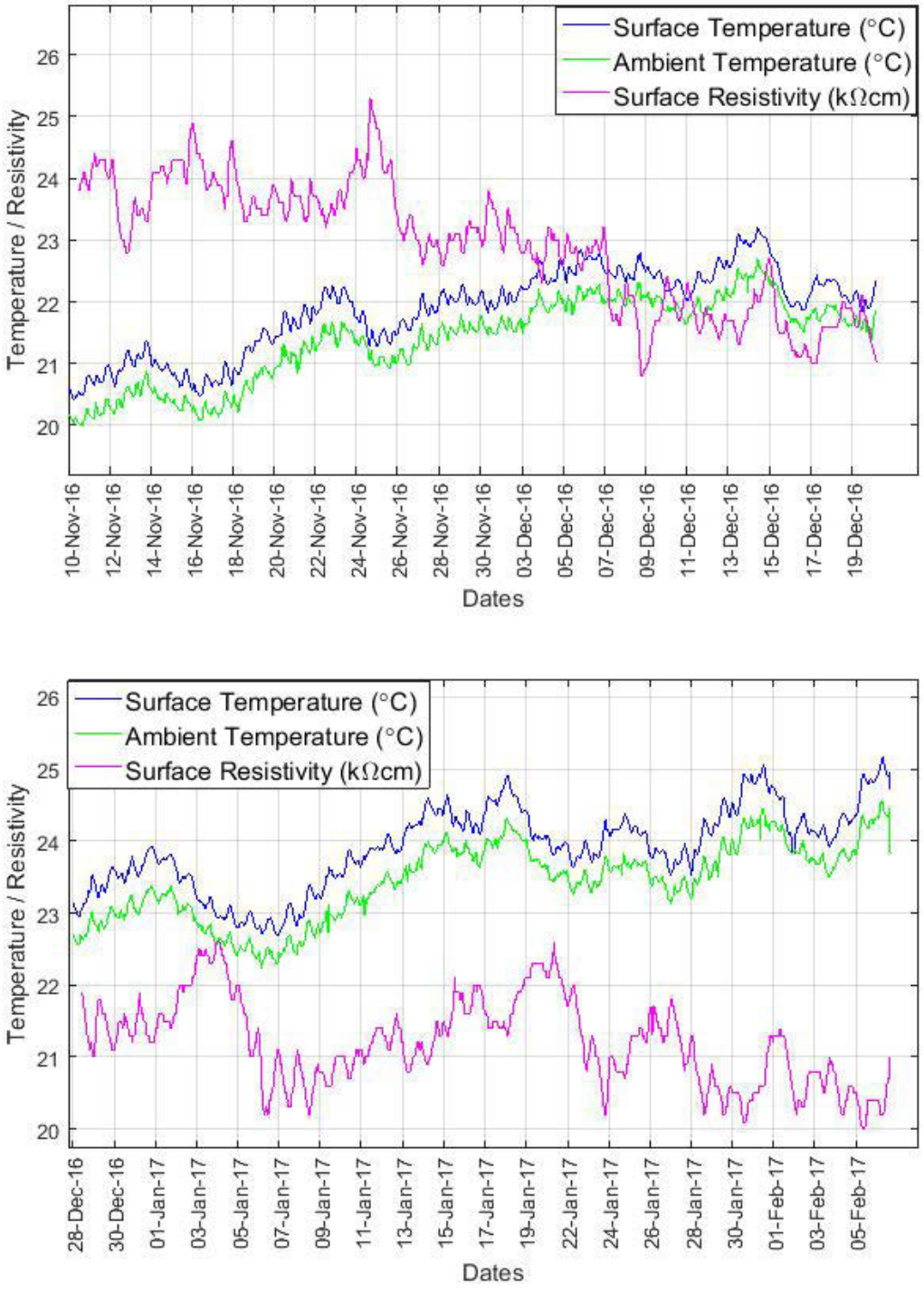

FIGURE 3.12: Profiles of surface resistivity, surface temperature and ambient temperature.

meter in wet and dry areas of the concrete sewer pipe and measuring the concrete surface resistivity.

By using the surface resistivity measurements, the surface moisture conditions can be mathematically determined by using the equation in 3.26

$$SM = 100 - \left(\frac{SR_S - SR_W}{SR_D} \right) \times 100 \tag{3.26}$$

where SM is the surface moisture condition of the concrete sewer pipe, SR_S is the surface resistivity value measured from the resistivity meter, SR_W is the surface resistivity value measured at wet area of the concrete sewer pipe and SR_D is the surface resistivity value measured at dry area of the concrete sewer pipe. All the surface resistivity measurements are expressed in terms of kΩcm and the surface moisture conditions are expressed in terms of %. From the on-site calibration, SR_D and SR_W were measured to be 364 kΩcm and 16 kΩcm respectively.

The surface moisture conditions determined by using Equation 3.26 is shown in Figure 3.13, where it can be observed that the surface moisture condition of the concrete sewer pipe is showing an increasing trend from November 2016 to February 2017, which is the summer season of the Sydney city of Australia. Overall, it can be concluded that the surface moisture conditions of the concrete sewer pipe were high during the field evaluation.

3.8.4 Post-deployment Validations

In this post-deployment validation study, the sensing performance of the moisture sensor was evaluated along with careful visual inspection of sensor enclosure. Figure 3.14 shows the sensor measurements taken after the field evaluation, where it can be seen from the plot that sensor has produced continuously 16 kΩcm and 120 kΩcm against the benchmark measure of 16 kΩcm and 120 kΩcm. This demonstrates that the measurements from the moisture sensor are produced without any bias. Therefore, the statistical metric MAPD for the sensing evaluation will have zero value, implying the measurements obtained from the sewer were reliable. Figure 3.15 shows the condition of the sensor enclosure post-exposure

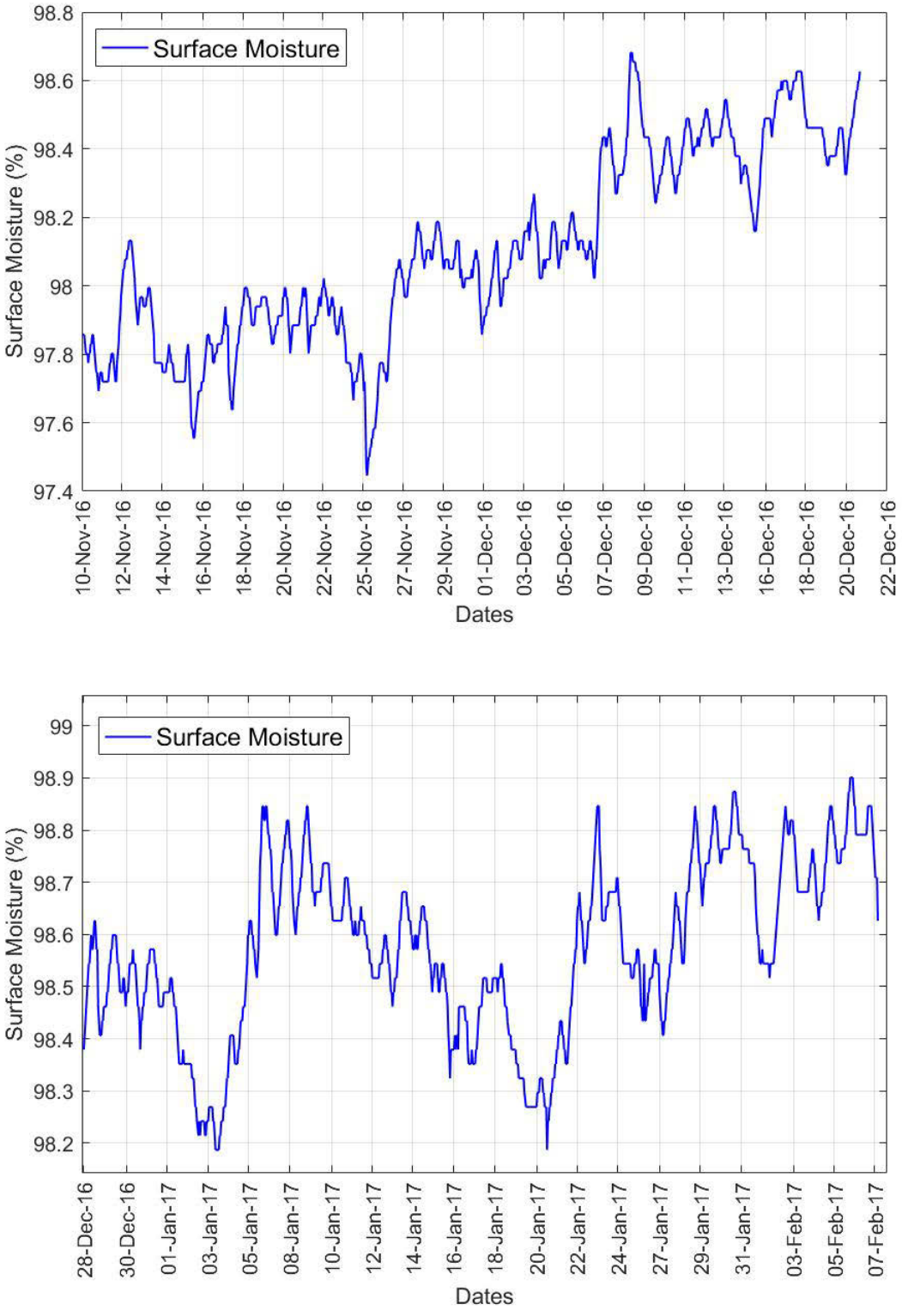

FIGURE 3.13: Surface moisture profiles obtained from the concrete sewer pipe.

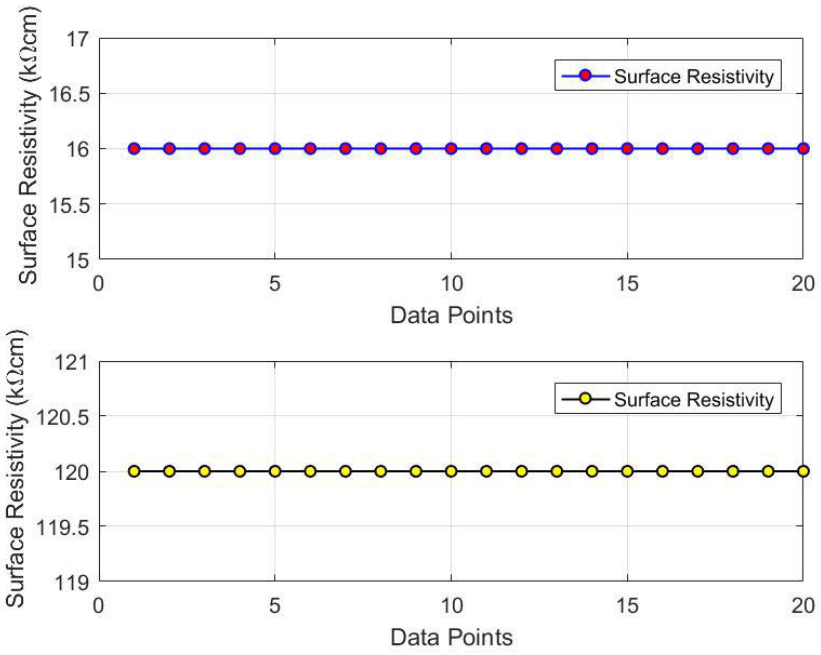

FIGURE 3.14: Moisture sensor measurements after long exposure to sewer conditions

to hostile sewer environment, where no visual degradation barring slight de-colouration the enclosure material was observed. From this post-deployment validation study, it can be concluded that the moisture sensor operates as desired without any apparent bias and the tailor-made sensor enclosure demonstrated robustness to sewer conditions after three months of exposure.

3.8.4.1 Spatial Estimation of Rebar Using GMRF

This section presents the results of the GMRF estimation of the rebar orientation based on non-invasive electrical resistivity measurements. The measurements were taken by placing the resistivity meter at different angles such as 0°, 30°, 45°, 60° and 90°. The angle 0° is perpendicular to the rebar whereas the angle 90° is parallel to the rebar.

Figure 3.16 shows the spatial estimation for the measurements taken at and angle 0°, Figure 3.17 shows the spatial estimation for the measurements taken at and angle 30°, Figure 3.18 shows the spatial estimation for the measurements taken at and angle 45°, Figure 3.19 shows the spatial estimation for the measurements taken at and angle 60° and Figure 3.20 shows the spatial estimation for the measurements taken at and angle 90°.

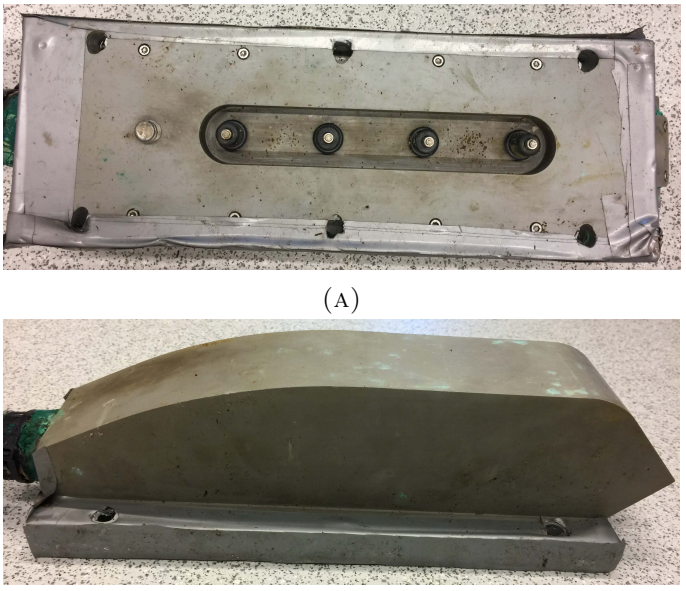

(A)

(B)

FIGURE 3.15: Sensor enclosure after exposure to hostile sewer conditions for about three months. (A) Top view of the sensor enclosure displaying the sensor electrodes and (B) Side view of the enclosure displaying the de-colouration occurred during the field evaluation.

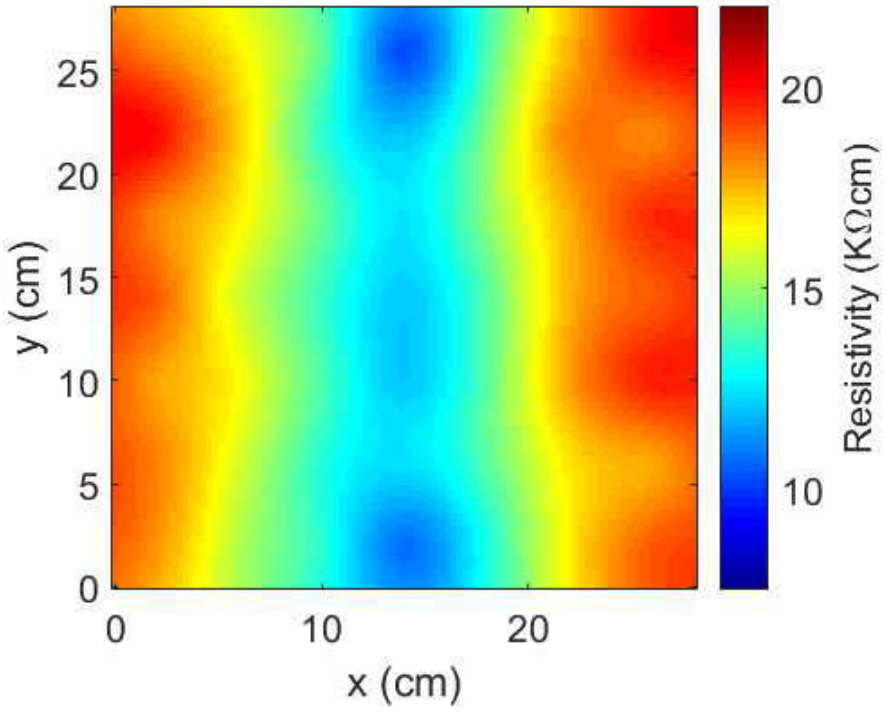

FIGURE 3.16: Spatial estimation using GMRF by taking resistivity measurements at 0°.

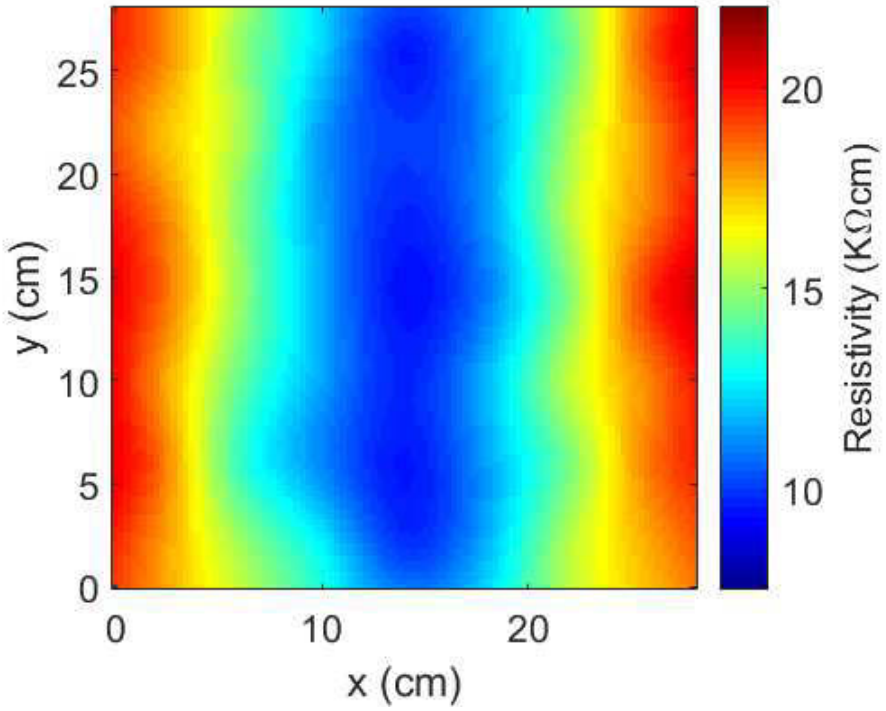

FIGURE 3.17: Spatial estimation using GMRF by taking resistivity measurements at 30°.

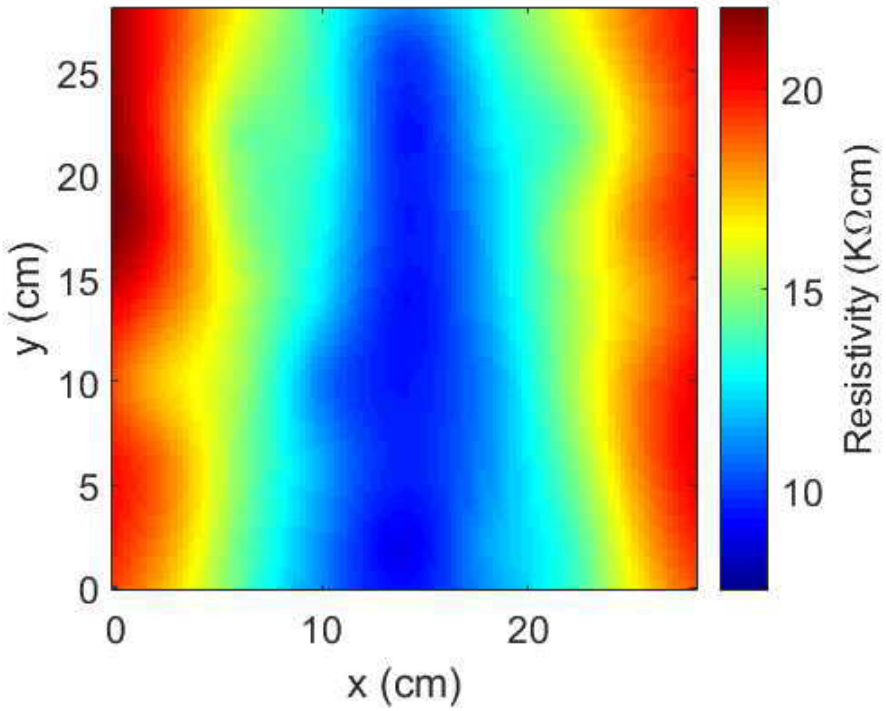

FIGURE 3.18: Spatial estimation using GMRF by taking resistivity measurements at 45°.

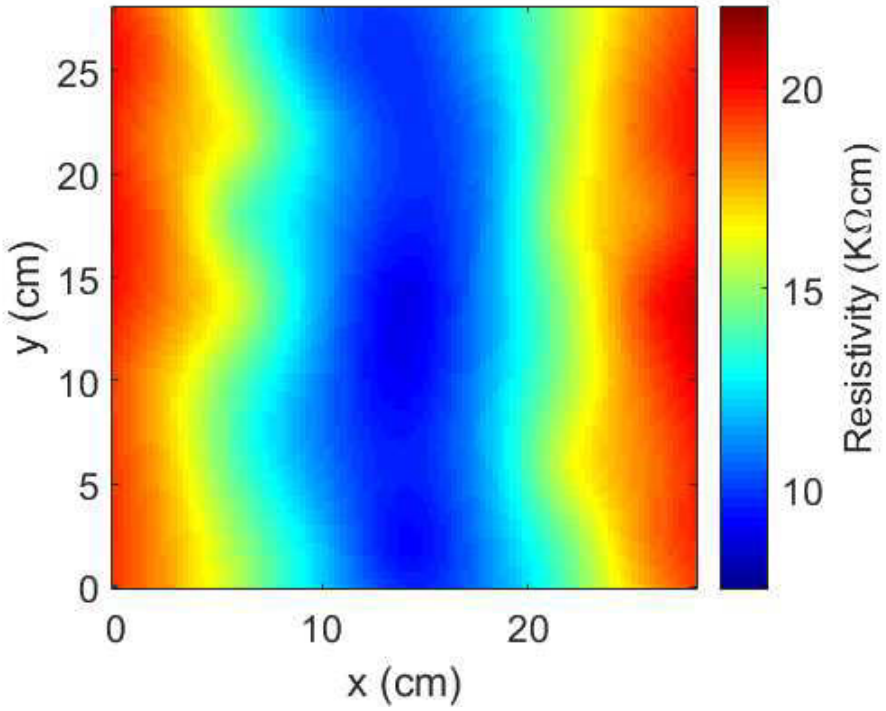

FIGURE 3.19: Spatial estimation using GMRF by taking resistivity measurements at 60°.

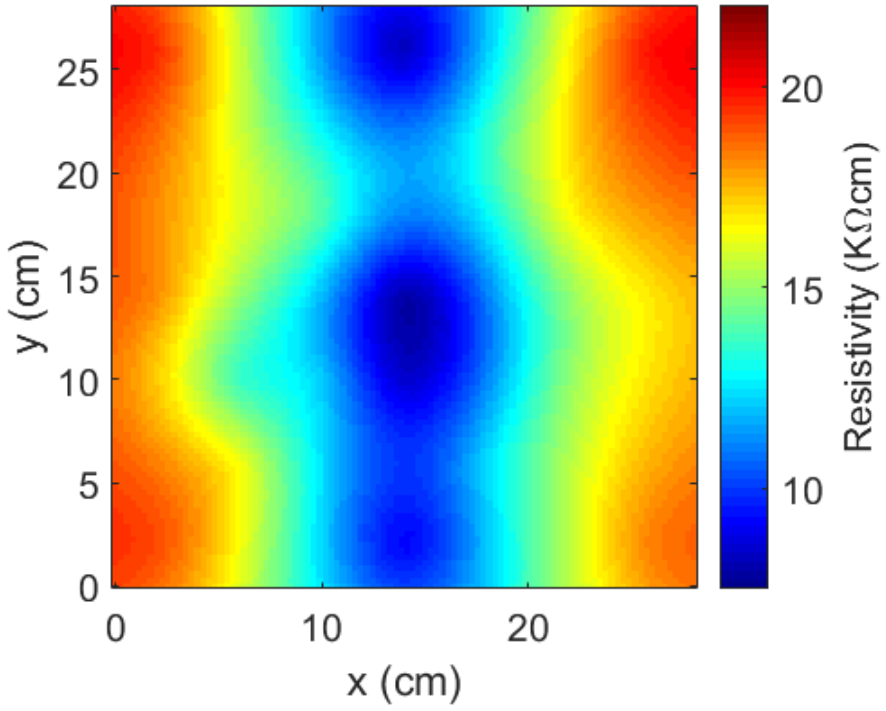

FIGURE 3.20: Spatial estimation using GMRF by taking resistivity measurements at 90°.

In order to evaluate the estimation performance of the GMRF model, MAE and RMSE were used as metrics, which computes based on the data of measured value and estimated value. This evaluation was carried out by placing the resistivity meter at an angle 90° and 3 sets of data were taken in the 49 partitions. Among the 49, 20 were used for training and 29 were used for testing. The Dataset-1 was computed to have MAE of 0.50 kΩcm and RMSE of 1.69 kΩcm, Dataset-2 was computed to have MAE of 0.61 kΩcm and RMSE of 1.60 kΩcm and Dataset-3 was computed to have MAE of 0.28 kΩcm and RMSE of 1.37 kΩcm. From these result, it can said that the estimation performance of the GMRF is satisfactory and this model can be used for spatially locating the rebar.

In the figures showing the spatial estimation using GMRF, the low resistivity area represents the orientation of the rebar. Therefore, it can be concluded that the measurements taken at different angles such as 0°, 30°, 45°, 60° and 90° showed that the rebar orientation can be estimated for optimal sensor placement. However, it can be observed from the Figure 3.16 that the measurements taken at the angle 0° has less rebar influence compared to other angles. Given the unknown conditions of the rebar at sewer pipes, the electrical resistivity measurements taken at different angles through GMRF spatial estimation model can shed light on the rebar location. Therefore, this information is vital to place the electrical resistivity meter for surface moisture estimation in sewer systems.

3.9 Summary

The research study presented in this chapter has developed a robust sensor technology for determining temporal dynamics of the surface moisture conditions in hostile sewer environments. The author believes that this is the first study to prove non-invasive type of surface moisture determinations in sewer system. In this regard, this chapter has led to the following key contributions:

- A scoping study was conducted to review the currently available surface moisture determining techniques indicating the suitability of using them in sewers. Almost all

the sensors have their applications in non-sewer conditions, but the scoping study has short-listed electrical resistivity based devices as the potential sensing solutions.

- A comprehensive evaluation was conducted in the laboratory condition to study the behaviour of concrete moisture with electrical resistance and pH conditions. Experimental results show that resistance measurements decrease with increase in moisture content for all the concrete samples that were influenced by solutions of different pH concentration levels. By using Gaussian Process regression modelling technique, the volumetric moisture content of concrete was predicted based on the resistance data and pH values as inputs. The prediction results indicated that the resistance sensor measurements are susceptible for different concretes.

- The resistivity meter was deployed inside the sewer system under the aggressive environmental conditions. The device was fixed near the crown of the concrete sewer pipe for measurements. This field evaluation was conducted for about three months and the data was obtained from the monitoring station constructed out side the sewer pipe. Then, the device was calibrated by taking measurements in sewer pipe to determine the surface moisture conditions. It can be concluded that the determination of surface moisture conditions through non-invasive electrical resistivity measurements is feasible and during the field experimentation, the surface moisture conditions were high throughout. However, further work need to be done on this.

- The post-deployment investigations showed the physical robustness of the resistivity meter and enclosure under the aggressive environmental conditions of the sewer. In addition, the post-deployment validation lab experiments showed that the electrical resistivity based moisture sensor was operating as desired and no bias was observed. Therefore, it can be concluded that the sensor performed reasonably well in sewers and their data are legitimate.

- GMRF based machine leaning model was proposed in this chapter for optimally placing the sensor on concrete surface to mitigate the effects of rebar. In this study, the GMRF model estimates the spatial orientation of the rebar using the measurements of electrical resistivity meter. The results demonstrated that the

electrical resistivity measurements taken at different angles such as 0°, 30°, 45°, 60° and 90° to the rebar shows the feasibility to locate the rebar through cost-effective and non-invasive techniques. However, it is recommended to take measurement at 90° for locating the rebar, since this angle has maximum influence of the rebar during measurements.

- It is believed that the real-time continuous measurements from the electrical resistivity based surface moisture sensor will provide information-rich data to the analytical models for better prediction of corrosion in sewers. Overall, the contributions of this chapter can enhance the waste water utilities present sewer corrosion monitoring capabilities. However, in order to fully utilize the sewer corrosion prediction model, there is a need to examine the reliability of the sensor measurements, i.e. whether the sensor provides meaningful legitimate data.

From the works presented in this chapter of the dissertation, the following publications resulted as an outcome.

- **K.Thiyagarajan**, S. Kodagoda, R. Ranasinghe, D. Vitanage and G. Iori, "Robust sensing system for non-invasive estimation of surface moisture conditions in concrete sewers," Nature - Scientific Reports. *(Under Review)*

- **K.Thiyagarajan**, S. Kodagoda, L.V. Nguyen, and S. Wickramanayake, "Gaussian Markov Random Fields for Localizing the Reinforcing Bars in Concrete Infrastructures," 35th International Symposium on Automation and Robotics in Construction (ISARC), Berlin, Germany, 2018. pp. 1035-1041.

- **K.Thiyagarajan**, S. Kodagoda and N. Ulapane, "Data-driven machine learning approach for predicting volumetric moisture content of concrete using resistance sensor measurements," 2016 IEEE 11th Conference on Industrial Electronics and Applications (ICIEA), Hefei, China, 2016, pp. 1288-1293.

Chapter 4

Smart Predictive Analytics for Detecting Sensor Failure

4.1 Introduction

Smart predictive analytics integrated with cutting-edge sensor technology is an imperative component of smart monitoring systems mainly due to the reason that it enables the practitioners to foresee the future trends and more squarely to answer "What is likely to happen?" based on the historical or past sensor data. Recently, the relevance of predictive analytics to tackle real-world problems that are emerging from the sophisticated mainstream utilities is a paradigm of "How the advancement in data analytics has taken the ascendency in delivering better solutions?".

Sensors play a vital role in providing information to predictive models for analysis and decision-making. They are essential constituents of any critical infrastructure monitoring system as they are responsible for maintaining the system safety and reliability [125]. However, in real-time systems, sensors can behave differently over time and provide spurious data owing to different erratic factors including the exposure of the sensor to a harsh environment and inherent sensing malfunctions [126]. Spurious data emanating from the sensors can be momentary or long-lasting. Momentary faulty data are likely to happen randomly due to changes in sensor characteristics over time. Those temporary

data should not be attributed to sensor failures. Instead, they need to be isolated as anomalies. However, the continuous spurious data could probably lead to sensor failure and result in downgrading the performance of an entire monitoring system, especially in critical infrastructures.

An urban sewerage system is a paradigm of a critical underground infrastructure system. The sewer environment conditions are harsh and notoriously capable of spoiling the sensors. Given the sensor units cannot be manually monitored all the time and they only can be remotely monitored through communication infrastructure, a mechanism to monitor and estimate sensor failure is an important aspect. With the increase of the number of the sensor units in the infrastructure, the need of an automatic sensor failure detection system becomes paramount. Therefore, early sensor failure detection is highly important for pertinent intervention strategies while monitoring the environmental phenomena of critical infrastructure assets like the sewer system.

Currently, there is no sensor system available in the state-of-the-art to monitor the temporal dynamics of surface temperature and surface moisture in the aggressively corrosive environmental conditions of the sewer. For that reason, a sensor suite was developed and deployed in sewers for a little over three months between 3rd November 2016 and 7th February 2017 in the municipal sewer of the Sydney city of Australia. The field testing campaign has demonstrated that the sensor suite is robust and capable of monitoring for long-term in sewer conditions. However, the confined sewer systems are a hostile environment to both sensor monitoring and human inspections. Since the sensor system cannot be physically monitored every time, Sensor Failure Detection and Accommodation (SFDA) algorithm can potentially become a salient feature in ameliorating the present sewer monitoring system.

This chapter of the dissertation focuses on developing a machine learning based diagnostic toolkit by presenting the SFDA algorithm for sewer monitoring application. The work motivates the development of a SFDA algorithm that possesses the following three properties.

- **Forecasting**: Forecasting is a process of predicting the future trends of data based on the collected historical data trends by using a mathematical model [127]. The

surface temperature data measured by the IRR sensor deployed inside the sewers along with the moisture sensor measuring surface resistivity are represented as a time-series data. By using the past temporal dynamics of the measured variable, the future trends will be foreseen by using a mathematical model. The forecast data will be acting as a virtual sensor to compare against the actual upcoming sensor data from the sewers for detecting anomalies and sensor failure. Also, in the event of scheduled sensor maintenance, the forecast data will be used to provide information to the analytical models that predict the rate of sewer concrete corrosion.

- **Anomalies detection and isolation** : Anomalies are unexpected patterns in the data that do not comply with the normal behavioural trends [128]. In this work, every single data that comes from the surface temperature sensor and moisture sensor are vital. So, the sensor data that deviates from the normal pattern is flagged as an anomaly. The presence of anomalies will downgrade the prediction performance of the forecast model. Therefore, it is important to detect the anomalies and isolate them before supplying the data for training the forecast model.

- **Sensor failure detection and accommodation** : Sensors are prone to fail over time. Detecting early sensor failure will enhance the present sewer monitoring capabilities for effective management of sewer assets. Also, it prevents the faulty data to train the forecasting model. Once the sensor failure has been detected, the faulty sensor data needs to be accommodated with the predicted data [129, 130]. The IRR sensor used in the field study for monitoring the surface temperature dynamics in sewers will fail only once and the failure is permanent. On the contrary, the moisture sensor may not fail permanently. It may produce continuous spurious data when there is any physical degradation in the sensor probes.

The remainder of this chapter is organized as follows: Section 4.2 presents the review of related work to the SFDA scheme. Section 4.3 presents the methodology for forecasting temporal dynamics of sensor variable using the SARIMA model. Section 4.4 illustrates the methodology for the proposed SFDA scheme. Section 4.5 presents the experimental evaluation results of the SFDA scheme. Finally, Section 4.6 summarizes the main contributions resulting from the proposed work with research outcomes.

4.2 Related Works

The state-of-the-art method for implementing the SFDA scheme is through hardware redundancy, where the particular variable is measured by using several identical sensors [131, 132]. Then, a voting logic is used to detect and identify the faulty sensor [133, 134]. For example, in a monitoring system with three redundant sensors as illustrated in Figure 4.1, if the measurement from one sensor varies significantly from the remaining sensors, then that particular sensor is asserted as the faulty sensor. In this approach, the sensor failure accommodation process is achieved by replacing the faulty sensor with a properly working one [131].

In the sensing applications where the sensors are expensive, analytical redundancy approaches are popular. In this approach, the signal between the sensor model and sensor is compared to generate the residual error. Then, the sensor failure is detected by setting a threshold logic for the generated residual error values [131, 133]. Figure 4.2 illustrates the block diagram for analytical redundancy approach. In the event of

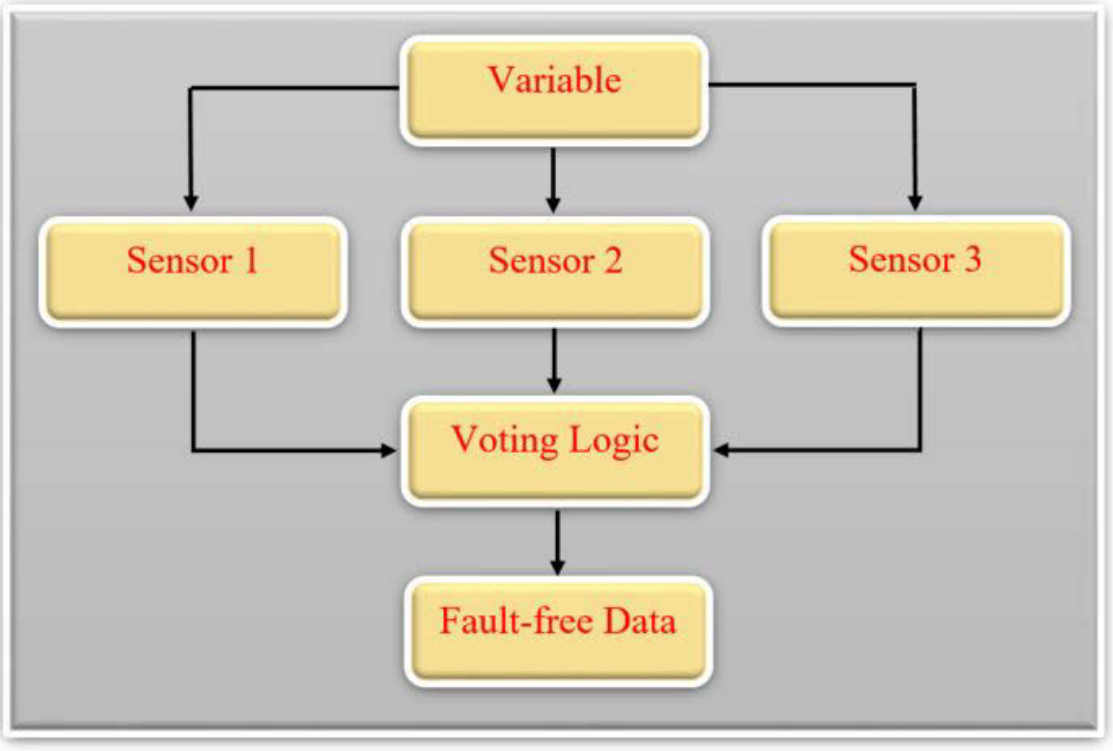

FIGURE 4.1: Block diagram of hardware redundancy.

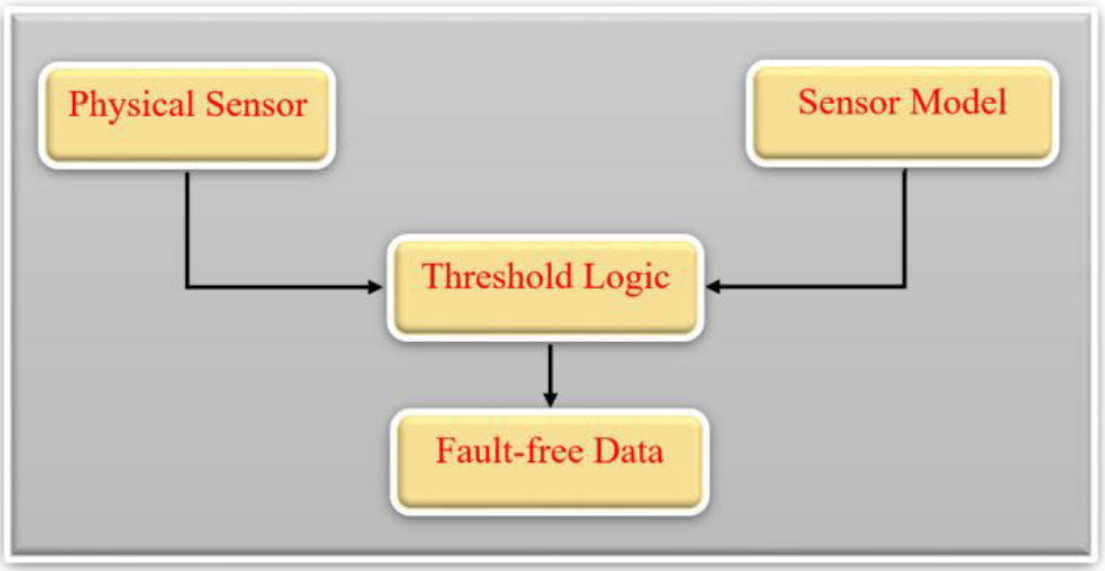

FIGURE 4.2: Block diagram of analytical redundancy.

detecting the sensor failure, the predicted data is used for sensor failure accommodation [131].

Computational modelling using artificial neural networks is widely used for detecting sensor failures mainly because of its adaptability to dynamic environments [131, 135, 136]. This method works by training the neurons and develop a structure based on the training data for comparing with the sensor measurements to detect the sensor failure [131]. On the other hand, time series forecasting models representing sensor data for linear time series is used for detecting early sensor failure [137]. There are several time series forecasting techniques available in the literature like Random Walk (RW) method, Simple Exponential Smoothing (SES) method and Autoregressive Moving Average (ARMA) model [138]. In the RW model, the variable value takes the independent random step. This method takes an assumption that past data is not informative and only the present observation is useful [139]. The SES model is used in applications of forecasting seasonal data. However, it is not an appropriate model in applications where the data has trends [140]. The ARMA method is an important method in time series forecasting [141]. This method is a stationary stochastic process, which combines the Autoregressive (AR) model and Moving Average (MA) model.

G.E.P. Box and G.M. Jenkins extended the ARMA model to Autoregressive Integrated Moving Average (ARIMA) model, which integrates the AR and MA parts of the model with differencing [142, 143]. Among the time series forecasting methods, ARIMA model has been widely used over the last two decades for forecasting applications [144]. The difference between the ARMA and ARIMA model is that the ARIMA model converts the non-stationary data into stationary data for predicting the linear time series [141]. For the data that shows seasonal trends, the ARIMA model is extended to SARIMA model [145–147]. Although ARIMA and SARIMA model has been used for forecasting applications in different sectors [148–152], their application in forecasting variables in sewers has not been reported.

Another forecasting model, which is used for time series forecasting is the Exponential Smoothing (ETS) model. This model is classified into linear exponential smoothing model and non-linear exponential smoothing model. The linear exponential smoothing model is a special case of the ARIMA model. However, the non-linear exponential smoothing models are not similar to the ARIMA models. Specifically, every ETS model possess a non-stationary trend whereas the ARIMA models can possess stationary trends [153]. This implies that the ETS model has a property that is dependent upon the time at which the data series value is noticed. Therefore, the seasonality will have an influence on the value of the time series data at different time periods.

In order to make the ETS models stationary, they need different stages of differencing. The differencing method computes the relative variations between the two consecutive observed data. Transformations like logarithms can aid to balance the variance of a time series. Differencing can assist to steady the mean of a time series by eliminating variations in the different stages of a time series, and therefore eradicating patterns and seasonality. The ETS models having seasonality trend or non-damped trend or both the trends will have two unit roots. This means that the ETS model needs two stages of differencing to make the time series as stationary. All other ETS models will have one unit root implying that the model needs only one stage of differencing to make the stationary trend [153].

By using the state space model combining with Box-Cox transformation, fourier series with time changing coefficients and ARMA error minimization another forecasting model

named TBATS model was introduced in 2011 [154]. The TBATS is an acronym describing the distinct features of the model, where 'T' stands for trignometric regressors to the model, 'B' stands for Box-Cox transformations, 'A' denotes the ARMA errors, 'T' implies the trend and 'S' denotes the seasonality. This model utilizes the state space model, which is the generalization of those underpinning ETS model. The TBATS model allows for automatic Box-Cox transformation and ARMA errors.

In order to achieve better forecasting results, the forecast model needs to be provided with anomalies-free data for training the model. Therefore, anomaly detection is vital for the application motivated in this work. Methods based on clustering, support vector machine and kernel functions are used for anomalies detection [155–157]. However, those approaches are dependent on static routing trees or assigning threshold values to the data streams [126]. In contrast, the work presented in this chapter focuses on detecting anomalies through statistical techniques for each sensor measurements. By using the stochastic time series models like SARIMA, anomalies can be detected in the data streams [158, 159]. Once the anomaly is detected, the faulty sensor reading is isolated. Then, the faulty information needs to be accommodated with the reliable value [160].

4.3 Forecasting Temporal Dynamics of Quantified Variables from the Sensing Suite

This section of the chapter delineates the methodology adopted to forecast the temporal dynamics of quantified variables such as surface temperature and surface resistivity. These variables are forecasted based upon the measurements of IRR sensor and moisture sensor data sourced from the instrumented sewer infrastructure.

4.3.1 Surface Temperature and Surface Resistivity Data From the Sensing Suite

The sensor data coming from the instrumented sewer infrastructure can be observed as a time series S_t, where the values of the data are at equally spaced times $t, t-1, t-2, ...$

by $S_t, S_{t-1}, S_{t-2}, ...$ The Dt is the time interval between the two sensor measurements.

4.3.2 Formulation of SARIMA Model

The ARIMA model is a combination of two independent models namely AR model and MA model with finite differencing of data points. Mathematically, the AR part of the ARIMA model can be defined as in Equation 4.1, which is an autoregressive process of order p. It can be succinctly expressed as $AR(p)$. This $AR(p)$ regresses the evolving variable against its prior values in the series.

$$AR(p)_t = c + \phi_1 \widetilde{S}_{t-1} + \phi_2 \widetilde{S}_{t-2} + ... + \phi_p \widetilde{S}_{t-p} + \varepsilon_t \tag{4.1}$$

where $AR(p)_t$ is the actual value of $AR(p)$ at time period t, $\phi_1, \phi_2, ..., \phi_p$ are the finite set of weight parameters of the $AR(p)$ with c as a constant and p as the order of the model $AR(p)$ with $\widetilde{S}_{t-1}, \widetilde{S}_{t-2}, .., \widetilde{S}_{t-p}$ as previous deviations from the mean value. The ε_t is the random shock and it is assumed to be a white noise process [161]. The ε_t is identically distributed i.e. $\varepsilon_t \sim IN(\mu, \sigma^2)$, where the mean $\mu = 0$ and a constant variance σ^2 [162].

The MA part of the ARIMA model is mathematically defined in Equation 4.2 and it can be called as a moving average process of order q or more succinctly $MA(q)$. This $MA(q)$ model uses its past errors as the explanatory variables.

$$MA(q)_t = c + \varepsilon_t + \theta_1 \varepsilon_{t-1} + \theta_2 \varepsilon_{t-2} + ... + \theta_q \varepsilon_{t-q} \tag{4.2}$$

where $MA(q)_t$ is the actual value of $MA(q)$ at time period t, $\theta_1, \theta_2, ..., \theta_q$ are the finite set of weight parameters of the $MA(q)$ with c as a constant and q as the order of the model $MA(q)$. Similar to $AR(p)$, the ε_t of $MA(q)$ is assumed to be a white noise process with identically distributed random variables with zero mean and constant variance.

By combining both $AR(p)$ and $MA(q)$ models together, the ARMA model is formed. It is mathematically defined in Equation 4.3 and it can be expressed as $ARMA(p, q)$.

$$AR(p)_t + MA(q)_t = c + \phi_1 \widetilde{S}_{t-1} + \phi_2 \widetilde{S}_{t-2} + ... + \phi_p \widetilde{S}_{t-p} + \\ \theta_1 \varepsilon_{t-1} + \theta_2 \varepsilon_{t-2} + ... + \theta_q \varepsilon_{t-q} + \varepsilon_t \tag{4.3}$$

where the predictor is $AR(p)_t + MA(q)_t$ of the $ARMA(p, q)$ as it includes the prior values of $AR(p)$ and past errors of $MA(q)$. The $AR(p)_t + MA(q)_t$ can be denoted as $\widetilde{S}_t$. In $ARMA(p, q)$, the order value p of $AR(p)$ model and q of $MA(q)$ model are not greater than 2 [163]. Upon simplification, Equation 4.3 can reduced to Equation 4.4. The constant term c is omitted for simplicity [164] and Equation 4.4 is rearranged to Equation 4.5, where the order of the models p and q denotes the p autoregressive term and q denotes the moving average term.

$$\widetilde{S}_t = c + \varepsilon_t + \sum_{n=1}^{p} \phi_n \widetilde{S}_{t-n} + \sum_{m=1}^{q} \theta_m \varepsilon_{t-m} \tag{4.4}$$

$$\widetilde{S}_t - \sum_{n=1}^{p} \phi_n \widetilde{S}_{t-n} = \varepsilon_t + \sum_{m=1}^{q} \theta_m \varepsilon_{t-m} \tag{4.5}$$

In time series data, the backshift operator (B) governs a value in the series to produce its prior value [165]. Mathematically, it is defined in Equation 4.6, where k is the time series backward observation of the time period.

$$B^k \widetilde{S}_t = \widetilde{S}_{t-k} \tag{4.6}$$

Generally, the $ARMA(p, q)$ model is manipulated by using Equation 4.6. By using the lag operator, the $ARMA(p, q)$ model Equation in 4.5 can be expressed as Equation 4.7.

$$\left(1 - \sum_{n=1}^{p} \phi_n B^n\right) \widetilde{S}_t = \left(1 + \sum_{m=1}^{q} \theta_m B^m\right) \varepsilon_t \tag{4.7}$$

The $ARMA(p, q)$ model is suitable only for stationary time series data. However, the sensor data emerging from the instrumented sewer infrastructure possess non-stationary behaviour. In order to process the non-stationary nature of sewer data, the ARIMA model

is utilized for the application reported in this work to forecast the quantified variables of the sensing suite. This model obtains homogeneous non-stationary behaviour by supposing a suitable d^{th} difference value of the process to the stationary $ARMA(p,q)$. The differencing is mathematically defined in Equation 4.8, where the $(1-B)^d = \Delta^d$.

$$\widetilde{S}_t = \Delta^d \widetilde{S}_t \tag{4.8}$$

Mathematically, the general form of ARIMA model can be defined as in Equation 4.9 and it can expressed as $ARIMA(p,d,q)$.

$$\left(1 - \sum_{n=1}^{p} \phi_n B^n\right) \Delta^d \widetilde{S}_t = \left(1 + \sum_{m=1}^{q} \theta_m B^m\right) \varepsilon_t \tag{4.9}$$

where the p, d and q are the integers referring to the order of autoregressive, integrated and moving average parts of the $ARIMA(p,d,q)$ model. The integer d governs the level of differencing.

The SARIMA model is employed in applications where the time series data presents seasonal changes [165]. The SARIMA is denoted as $SARIMA(p,d,q)(P,D,Q)_{S_p}$, where P is the seasonal autoregressive parameter, D is the degree of seasonal differencing parameter, Q is the seasonal moving average parameter and the subscript S_p denotes the seasonal period of this stochastic model.

The forecasts of sewer sensing suite variable by using the $SARIMA(p,d,q)(P,D,Q)_{Sp}$ is given by Equation 4.10, where the Φ and Θ are the weight parameters of seasonal autoregressive term and seasonal moving average term respectively.

$$\begin{aligned} &\left(1 - \sum_{n=1}^{p} \phi_n B^n\right)\left(1 - \sum_{n=1}^{P} \Phi_n B^{S_p}\right)(\Delta)^d (\Delta^{S_p})^D \widetilde{S}_t \\ &\qquad = \left(1 + \sum_{m=1}^{q} \theta_m B^m\right)\left(1 + \sum_{m=1}^{Q} \Theta_m B^{S_p}\right)\varepsilon_t \end{aligned} \tag{4.10}$$

4.3.3 Automatic Selection of SARIMA Model Parameters

For $SARIMA(p,d,q)(P,D,Q)_{S_p}$ model, the order parameters p,d,q,P,D and Q are automatically determined by using Hyndman and Khandakar algorithm [153, 166]. The differencing terms d and D are computed by performing the unit root test such as Kwiatkowski Phillips Schmidt Shin (KPSS) test. The KPSS test is generally used for evaluating a null hypothesis, where an observable time series is stationary around a deterministic trend (i.e. trend-stationary) against the alternative of a unit root [167].

If the values of differencing parameters d and D are known, then the Hyndman and Khandakar algorithm [166] selects the values for p,q,P and Q through minimization of an Akaike Information Criterion (AIC). The AIC is mathematically expressed as given in Equation 4.11.

$$AIC = -2\log(L) + 2(p+q+P+Q+K_n) \tag{4.11}$$

where L is the maximized likelihood of the $SARIMA(p,d,q)(P,D,Q)_{S_p}$ model fitted to the differenced data $(\Delta)^d(\Delta^{S_p})^D\widetilde{S}_t$ and K_n is the number of parameters estimated to compute one-step ahead forecasts.

4.3.4 Computing Prediction Intervals of the Forecasts at Any Lead Time

A prediction interval of the forecast is an estimate of an upper and lower bound of an interval in which the observable sensing suite variable of the future is expected to lie with a specified probability based on the past observed values [153, 168]. Considering that $g's$ are Gaussian distribution with standard deviation σ_g and weights ψ, then the probability distribution $(S_{t+f}|S_t, S_{t-1}, S_{t-2}, ...)$ of a future observable value S_{t+f} of the process will be normal with mean $\hat{S}_t(f)$ and standard deviation $\sigma(f)$. The $\sigma(f)$ is given in Equation 4.12 [163].

$$\sigma(f) = \left(1 + \sum_{j=1}^{f-1} \psi_j^2\right)^{1/2} \sigma_g \tag{4.12}$$

The variate $\Big[\big[S_{t+f} - \hat{S}_t(f)\big] / \big[\sigma(f)\big]\Big]$ will posses a unit normal distribution. Therefore, for S_{t+f}, $\hat{S}_f \pm \mu_{\lambda/2}\sigma(f)$ will provide the bounds of the prediction interval with probability $1-\lambda$. $\mu_{\lambda/2}$ is the deviate transcended by a proportion of $\lambda/2$ of the unit normal distribution. Mathematically, the prediction interval for the $SARIMA(p,d,q)(P,D,Q)_{S_p}$ model can be computed by using Equation 4.13 [163].

$$\hat{S}_{t+f}(\pm) = \hat{S}_t(f) \pm \mu_{\lambda/2}\left(1 + \sum_{j=1}^{f-1}\psi_j^2\right)^{1/2}\sigma_g \tag{4.13}$$

where $\mu_{\lambda/2}$ are the percentiles of the standard normal distribution. In this section, $\mu_{\lambda/2} = 95\%$. The forecast value $\hat{S}_{t+f}$ coming from the $SARIMA(p,d,q)(P,D,Q)_{S_p}$ model with the probability of $1-\lambda$ will lie between the upper interval $\hat{S}_{t+f}(+)$ and lower interval $\hat{S}_{t+f}(-)$, i.e. Probability $\big\{\hat{S}_{t+f}(-) < \hat{S}_{t+f} < \hat{S}_{t+f}(+)\big\}$.

4.4 SFDA Algorithm

The SFDA algorithm proposed in this chapter presents a smart predictive analytic framework by combining predictive analytics and statistical diagnostic method. The predictive analytics component of the SFDA algorithm features $SARIMA(p,d,q)(P,D,Q)_{S_p}$ model for forecasting the temporal dynamics of the sensing suite variable. By utilizing the readings from the IRR sensor and moisture sensor, the $SARIMA(p,d,q)(P,D,Q)_{S_p}$ model provides a viable alternative to physical sensor measurements by means of the forecast data $\hat{S}_{t+f}$. This $\hat{S}_{t+f}$ will function as a virtual sensor. Algorithm 1 presents the pseudocode for the SARIMA forecast.

Algorithm 1 Pseudocode for the SARIMA Forecast

for all $i \in 1 : length[R(t)_i]$ **do**

Computing p, d, q, P, D and Q

Forecasting $[\hat{S}_{t+f}]_i$

Computing $[\hat{S}_{t+f}(-)]_i$ and $[\hat{S}_{t+f}(+)]_i$

$i = i + 24$

end for

The forecasting process of the $SARIMA(p,d,q)(P,D,Q)_{S_p}$ model involves three main steps. They are as follows:

- The first step of the forecasting model is to visualize the time-series data and to provide the sensor data for training the forecast model.
- In the second step, the $SARIMA(p,d,q)(P,D,Q)_{S_p}$ model parameters are determined by invoking Hyndman and Khandakar algorithm for automatic selection of p, d, q, P, D and Q, and eventually building a forecast model using the determined parameters.
- Finally in the third step, the model forecasts the sensor variable data $\hat{S}_{t+f}$ for the next day containing 24 data points with $\hat{S}_{t+f}(-)$ and $\hat{S}_{t+f}(+)$ values. The 24 data points are from the time 00:00 to 23:00 with an interval of one hour of that respective day.

The diagnostic component of the SFDA algorithm presents statistical techniques for detecting sensor failure and anomalies by using the data from the instrumented sewer infrastructure and $SARIMA(p,d,q)(P,D,Q)_{S_p}$ model forecasts. This component employs statistical hypothesis testing for computing probability value (p-value) to detect anomalies and sensor failure in the stream of upcoming data from the IRR sensor. In hypothesis testing, the p-value is the probability for a given statistical model that, when the null hypothesis is true, the statistical summary (such as the sample mean difference between two compared groups) would be the same as or of greater magnitude than the actual observed results [169].

In SFDA algorithm, the p-value is obtained by performing Pearson's chi-squared test, which is usually denoted as χ^2. This statistical test is applied to the sets of categorical data to examine the divergence between the data sets. The χ^2 determines the divergence of the observed sensor data from the values that would be forecasted using the $SARIMA(p,d,q)(P,D,Q)_{S_p}$ model under the null hypothesis of no association. The distribution of sum of the squares of a set of independent standard normal random variables in probability theory is known as chi-squared distribution. It is denoted as χ^2_{df}

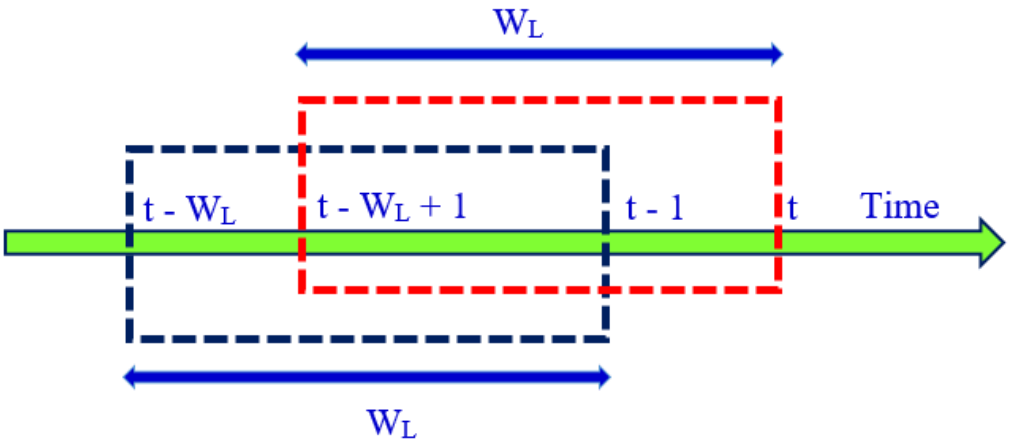

FIGURE 4.3: Illustration of the sliding window mechanism at time period t.

and used in the χ^2 for goodness of fit of the observed sensor data distribution to a distribution of $SARIMA(p,d,q)(P,D,Q)_{S_p}$ model data. The χ^2_{df} is characterized by degrees of freedom df, which is the number of values that are free to vary in a dynamic system without violating any constraint foisted to the system. The df value is one less than the number of total data points in the data set used to compute one χ^2 measure.

A technique is adopted in the SFDA algorithm to partition the sequence of the sensor data and forecasted data with a finite array size. After partitioning, the fixed array is slided by a position over the stream of data sequence. This event is known as sliding window mechanism [131, 133]. It is incorporated within the SFDA algorithm framework to provide a set of data for computing p-value. This mechanism is illustrated in Figure 4.3, where the sliding window of size W_L data points keeps moving as the time t progresses. In the proposed SFDA algorithm, $W_L = 6$. So, the χ^2_{df} of observed IRR sensor data and the $SARIMA(p,d,q)(P,D,Q)_{S_p}$ model data takes 6 data points for computing χ^2. Therefore, the df of that χ^2 will be $W_L - 1$ for all sliding windows.

The χ^2 measure for the testing dataset $\sum$ of size W_L is measured by using Equation 4.14.

$$\chi^2 = \sum_{i=1}^{i=W_L} \frac{\left[(R_t)_i - (\hat{S}_{t+f})_i\right]^2}{(\hat{S}_{t+f})_i} \tag{4.14}$$

where i is the instantaneous time, χ^2 is the cumulative statistic of Pearson's chi-squared test, R_t is the observed sensor data used for detecting anomalies and sensor failure, $\hat{S}_{t+f}$ is the expected data resulting from the forecast model, $SARIMA(p,d,q)(P,D,Q)_{S_p}$. Algorithm 2 presents the pseudocode for the function calculating the χ^2 value by incorporating sliding window mechanism.

Algorithm 2 Pseudocode - Function CHI CALCULATOR

/* FUNCTION PARAMETERS */

$[R(t)]_i$, $[\hat{S}_{t+f}]_i$, W_L

/* INITIALIZATION OF VARIABLES */

$Total = 0$

---

for all $i \in 1 : (1 + W_L)$ **do**

$Total = Total + \Big([R(t)]_i - [\hat{S}_{t+f}]_i\Big)^2 / [\hat{S}_{t+f}]_i$

end for

$return(Total)$

Since the value of W_L is static for all the computations, df will be same for all the computations as well, with the value of $df = 5$. After computing χ^2 and df, it is therefore important to set a critical significance level to determine the p-value for each sliding window. The critical significance level is the probability of rejecting the null hypothesis when it is true. They are typical threshold values that define the regions of the χ^2_{df}, where the test statistic is unlikely to lie. The critical significance level is usually denoted as α, which defines the sensitivity of the hypothesis testing. The α is an arbitrary value chosen depending on the application. The χ^2_{df} is an asymmetric distribution. It is typically skewed with a long tail to the right. This implies that the χ^2_{df} has only positive values. For instance, Figure 4.4 shows the probability density function curve to the right, where the shaded area represents the critical region. In that region, the values of the test statistic is rejected if it is larger than α .

In the proposed SFDA algorithm α is 5% i.e., $\alpha = 0.05$. This implies that the null hypothesis is rejected 5% of the time when it is in fact true. Given the α and df, the contingency table that shows multivariate frequency distribution of the variables will be

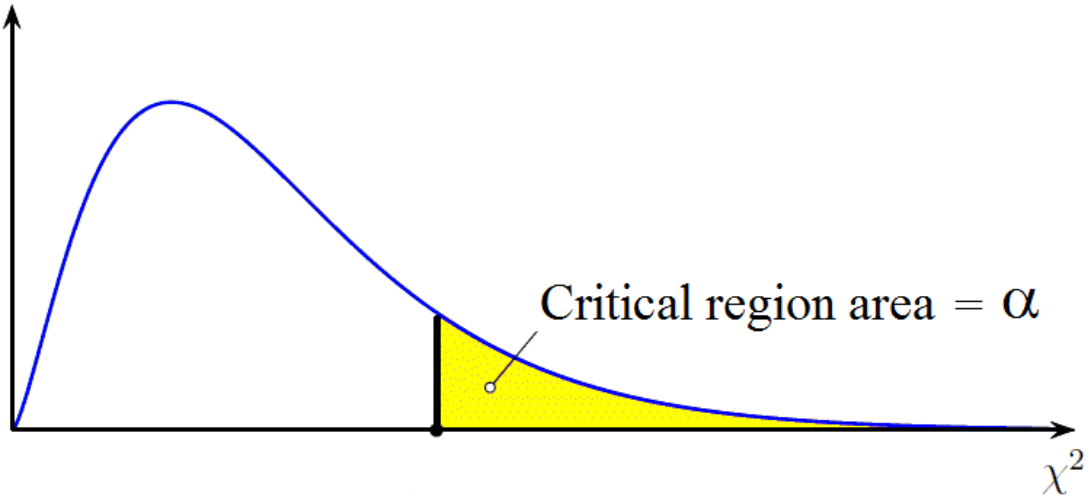

FIGURE 4.4: Illustration of the chi square.

referred. This table provides values with respect to df and α. Then, by comparing the measures of χ^2 with χ^2_{df}, p-value is given by Equation 4.15.

$$P - value = P(\chi^2_{df,\alpha} \geq \chi^2) \tag{4.15}$$

Algorithm 3 presents the pseudocode for calculating the p-value after determining the χ^2 value for the given sliding window frame.

Algorithm 3 Psuedocode - Function P-value CALCULATOR

/* FUNCTION PARAMETERS */

$[R(t)]_i$, $[\hat{S}_{t+f}]_i$, W_L

/* INITIALIZATION OF VARIABLES */

$df = W_L - 1$

$\chi^2 = chiCalculator(R(t)]_i, [\hat{S}_{t+f}]_i, W_L)$

$P - value = 1 - chi2Cdf(\chi^2, df)$

$return(P - value)$

For the critical level of α, the statistical hypothesis testing provides significant value only if the is $\chi^2_{df,\alpha}$ greater than the χ^2. In case of χ^2 being greater than the $\chi^2_{df,\alpha}$, the statistical hypothesis testing provides a non-significant value. The determination of significant and non-significant value plays a paramount role in the SFDA algorithm for detecting the

anomalies and sensor failure. The procedural characteristic of SFDA algorithm to the significant and non-significant value is enumerated as follows:

- In a sliding window, if the p-value is a significant value i.e., p-value > 0.95, then the sensor data measurements of that particular sliding window will be pushed to the training dataset of the $SARIMA(p,d,q)(P,D,Q)_{S_p}$ model for forecasting the future values. Consequently, the sliding window progresses to the next window for performing statistical testing. This process iterates as long as the sensor provides measurements from the instrumented sewer infrastructure.
- In the case of sliding window producing a non-significant p-value i.e., p-value < 0.95, then the sensor data measurements of that particular window is examined to check the presence of anomalies or any indications of early sensor failure. Each data of the sensor measurements within that sliding window is evaluated with respect to the corresponding prediction intervals.

The condition to examine the sensor data of the sliding window that has produced a non-significant value is defined in Equation 4.16.

$$\left[\left(\hat{S}_{t+f}(-)\right)_i\right] < \left[\left(R_t\right)_i\right] < \left[\left(\hat{S}_{t+f}(+)\right)_i\right] \tag{4.16}$$

where i is the instantaneous time. If the condition in Equation 4.16 is not satisfied, then there arises three scenarios. In all the scenarios, the SFDA algorithm will look for continuity of individual data of sensor measurements present outside of $\hat{S}_{t+f}(-)$ or $\hat{S}_{t+f}(+)$.

- In the first scenario where one or two $(R_t)_i$ are present outside of $\hat{S}_{t+f}(-)$ or $\hat{S}_{t+f}(+)$, then that respective sensor data is regarded as an anomaly. Subsequently, the SFDA algorithm performs data accommodation process, where the value of $(R_t)_i$ is accommodated by $\left(\hat{S}_{t+f}\right)_i$.
- In the second scenario where there are three or more $(R_t)_i$ present outside of $\hat{S}_{t+f}(-)$ or $\hat{S}_{t+f}(+)$ and their continuity is less than three successive times, the

Algorithm 4 Psuedocode - Detecting Sensor Failure and Anomalies, Data Accommodation Process

/* FUNCTION PARAMETERS */
$P - value, [R(t)]_i, [\hat{S}_{t+f}(-)]_i, [\hat{S}_{t+f}]_i, [\hat{S}_{t+f}(+)]_i, W_L$
$Timestamp$
/* INITIALIZATION OF VARIABLES */
$COUNTERS : Total = 0; Warning\_Count = 0;$
$Failure\_Count = 0; Previous\_ID = 0;$
$FLAG : Failed = FALSE$

---

if $(!(P - value > \alpha))$ **then**
  for all $i \in 1 : (1 + W_L)$ **do**
    if $(![R(t)]_i \geq [\hat{S}_{t+f}(-)]_i \&\& [R(t)]_i \leq [\hat{S}_{t+f}(+)]_i)$ **then**
      /* Evaluating Sensor Failure Condition*/
      if $(i == Previous\_ID + 1)$ **then**
        $(Failure\_Count = Failure\_Count + 1)$
        if $(Failure\_Count >= 3)$ **then**
          Message: $Sensor\_Failure\_(Timestamp)$
          $(Failed = TRUE)$
        end if
      end if
      $Previous\_ID = i$
      /* Evaluating Sensor Warning Condition */
      if $(!Failed)$ **then**
        $(Warning\_Count = Warning\_Count + 1)$
        if $(Warning\_Count >= 3)$ **then**
          Message: $Sensor\_Warning\_(Timestamp)$
        end if
      end if
      /* Anomaly Detection & Data Accommodation */
      Message: $Anomaly\_Detected\_(Timestamp)$
      Data Accommodation: $[R(t)]_i = [\hat{S}_{t+f}]_i$
    end if
  end for
end if
$return([R(t)]_i)$

$(R_t)_i$ is still flagged as an anomaly. However, sensor failure warning will be issued for inspection. In addition to the warning signal, the SFDA algorithm undergoes data accommodation process to replace the faulty $(R_t)_i$ with respective $\left(\hat{S}_{t+f}\right)_i$.

- Finally, in the third scenario where there are more than one $(R_t)_i$ present outside of $\hat{S}_{t+f}(-)$ or $\hat{S}_{t+f}(+)$ and their continuity is three or more successive times in one sliding window, then a signal of early sensor failure is issued. Even in this scenario, the SFDA algorithm will invoke data accommodation process to replace the faulty $(R_t)_i$ with respective $\left(\hat{S}_{t+f}\right)_i$.

The SFDA algorithm iterates the data accommodation process until $(R_t)_i$ is present within the $\hat{S}_{t+f}(-)$ and $\hat{S}_{t+f}(+)$. Algorithm 4 presents the pseudocode for detection of anomalies, sensor failure and data accommodation process.

4.5 Experimental Evaluation Results

This section of the chapter presents the experimental evaluation results of the SFDA algorithm. Firstly, this section investigates the forecasting performance of the SARIMA model by comparing it with the other two popular forecasting models. Secondly, this section evaluates the application of the SFDA algorithm to the surface temperature data and surface resistivity data sourced from the sewer monitoring system for short-time and long-term detection capabilities. Thirdly, the section evaluates the forecasting performance of the SFDA algorithm. Finally, this section evaluates the data accommodation process.

4.5.1 Comparative Analysis of Forecasting Models

The performance of sensor data forecasting using SARIMA model is examined by comparing with ETS and TBATS models by utilizing surface temperature measurements from the sewer system. The IRR sensor data of 30 days between 4$^{\text{th}}$ November 2016 and 3$^{\text{rd}}$ December 2016 is used in this evaluation. The total length of data points is $DP_{total} = 720$ and the data points of the first 24 days containing $DP_{training} = 576$ will be

used as the training dataset. Remaining data points $DP_{testing} = 144$ will be used for evaluating the performance of sensor data prediction.

Figure 4.5 shows the profile of input training data that were supplied to the different forecasting models. The training data was from the IRR sensor measurements sourced from the sewer monitoring campaign from 00:00 hours of 4th November 2016 to 23:00 hours of 28th November 2016. By using the training data, the SARIMA, TBATS and ETS models were trained to forecast data from 00:00 hours of 28th November 2016 to 23:00 hours of 3rd December 2016. Figure 4.6 presents the forecast data profile for the ETS model and Figure 4.7 shows the forecast trends determined by using TBATS model along with the actual sensor measurements. In addition, Figure 4.8 shows the forecast pattern profile which resulted from the SARIMA model. Figure 4.9 displays the profile comparison of time series forecasting of sensor variable from 00:00 hours of 28th November 2016 to 23:00 hours of 3rd December 2016 between SARIMA, TBATS and ETS models with the measured sensor data profile.

To evaluate the performance of the forecast models and to choose a suitable model for the

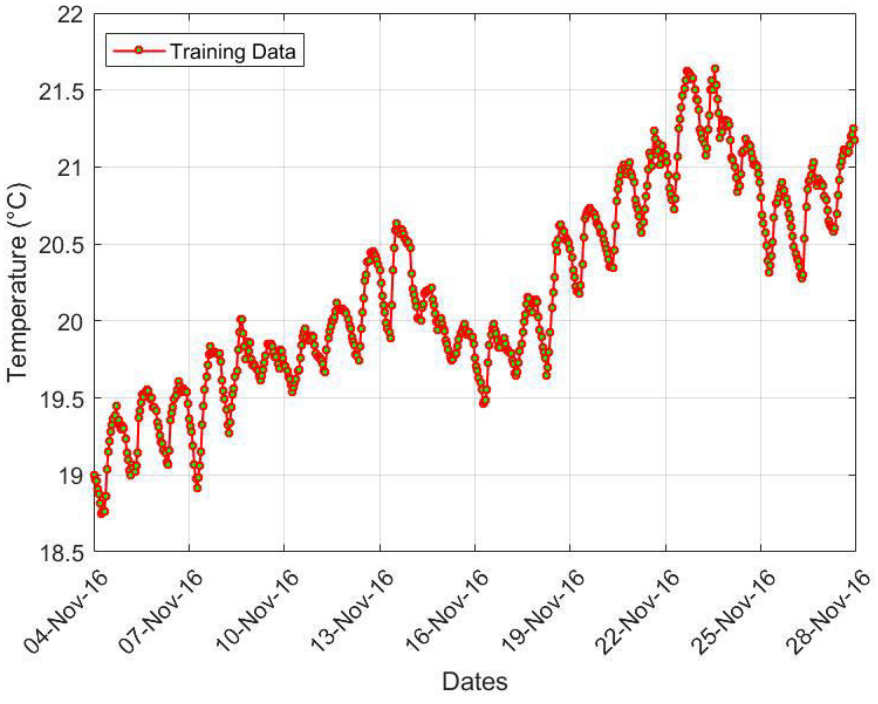

FIGURE 4.5: Profile of the training data.

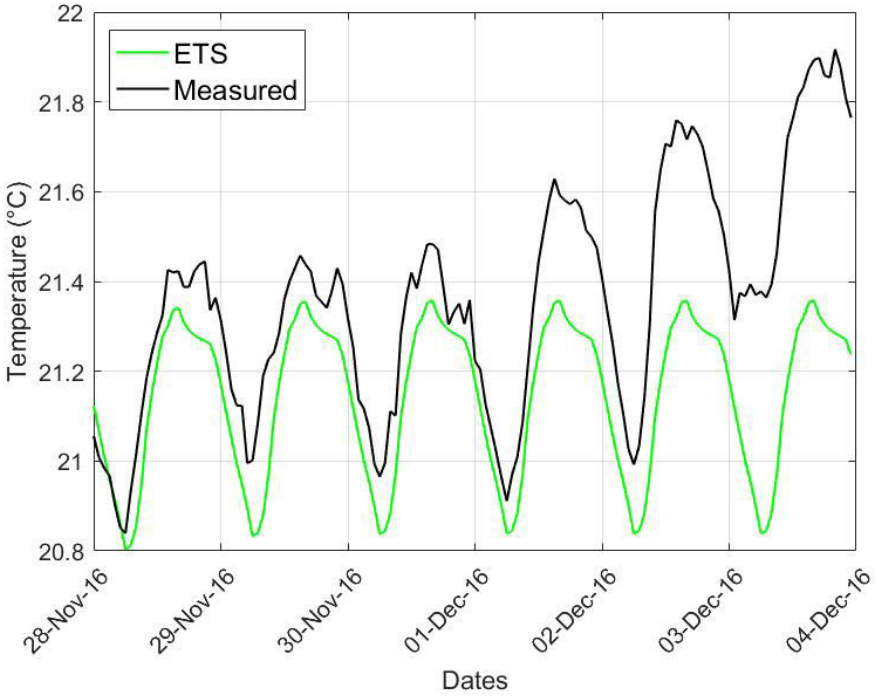

FIGURE 4.6: Forecast data profile resulting from the ETS model.

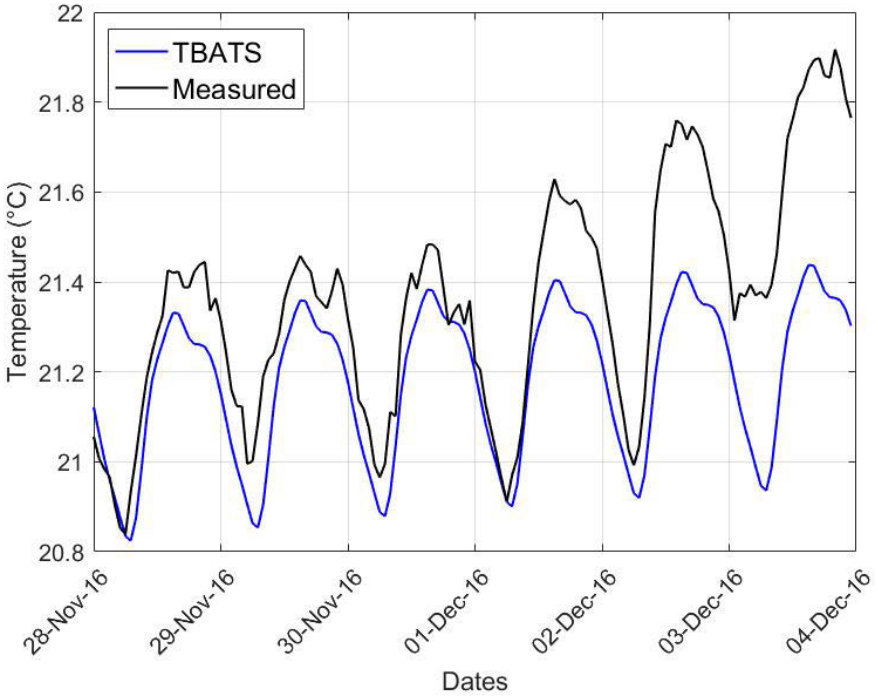

FIGURE 4.7: Forecast data profile resulting from the TBATS model.

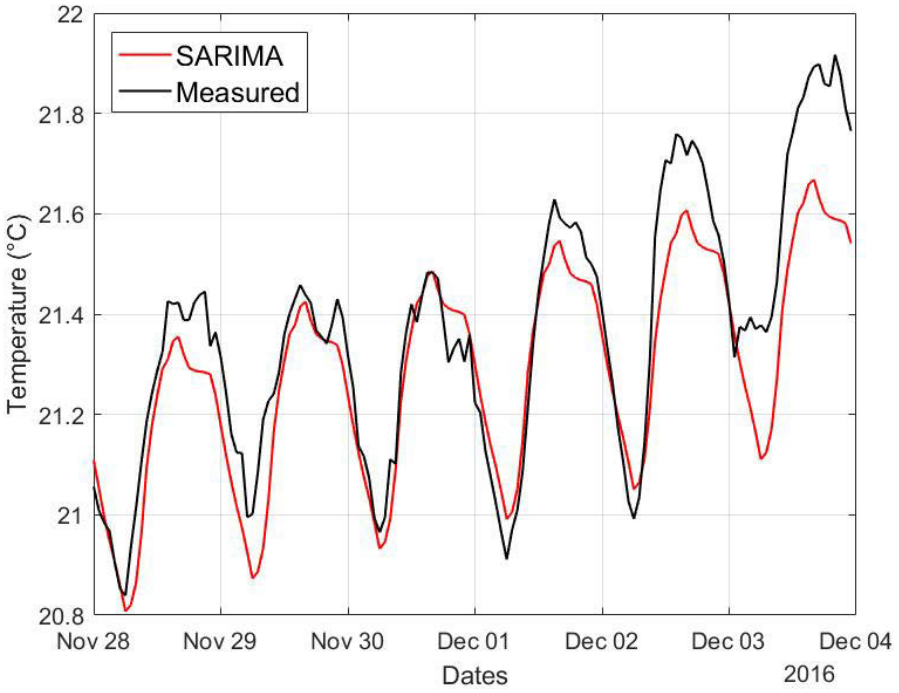

FIGURE 4.8: Forecast data profile resulting from the SARIMA model.

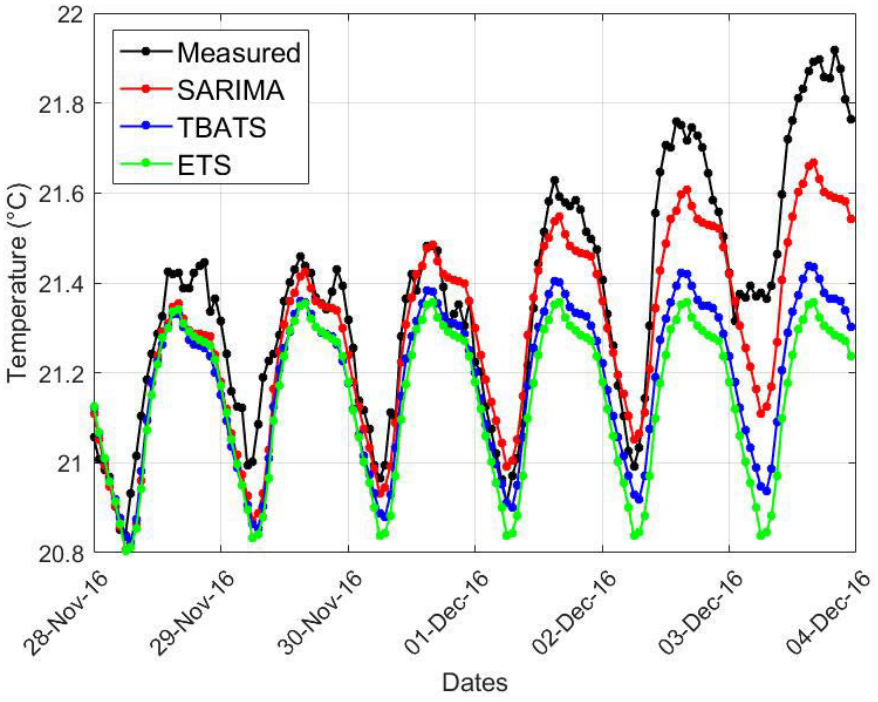

FIGURE 4.9: Comparison of time series forecasting of sensor data using SARIMA, TBATS and ETS models with the measured sensor data profile.

sparse data from sewers, statistical performance metrics such as MAE, Mean Percentage Error (MPE), Mean Absolute Percentage Deviation (MAPD) and RMSE were used to compute the forecast errors. The statistical metrics used for this evaluation are defined as follows:

$$MAE = \frac{1}{n}\sum_{t=1}^{t=n} |Forecast\_Value - Sensor\_Value| \tag{4.17}$$

$$MPE = \frac{100\%}{n}\sum_{t=1}^{t=n} \frac{Forecast\_Value - Sensor\_Value}{Sensor\_Value} \tag{4.18}$$

$$MAPD = \frac{100\%}{n}\sum_{t=1}^{t=n} \left|\frac{Forecast\_Value - Sensor\_Value}{Sensor\_Value}\right| \tag{4.19}$$

$$RMSE = \sqrt{\frac{1}{n}\sum_{t=1}^{t=n} (Forecast\_Value - Sensor\_Value)^2} \tag{4.20}$$

where the $Forecast\_Value$ is the data forecast from SARIMA, ETS and TBATS model respectively, $Sensor\_Value$ is the data obtained from the sensor measurements, t is the instantaneous time and n is the number of forecast values.

It can be observed from Table 4.1 that the MAE and RMSE of TBATS model were smaller than those of ETS model. Thence, the prediction performance of TBATS was better than ETS. However, the MAE and RMSE of TBATS model were higher than those of SARIMA model. So, based on MAE and RMSE the prediction performance of SARIMA model was better than the other two models. Like aforementioned statistical performance metrics, the MPE and MAPD of TBATS model were smaller than those of ETS model and higher than those of SARIMA model. To put it in a nutshell, based on the four different performance metrics for forecasting the sensor data sourced from sewers, SARIMA model had better performance and it is used as a forecasting model to detect the sensor failure application.

Statistical Performance Evaluation of Time Series Models			
Statistical Metrics	SARIMA	ETS	TBATS
MAE (°C)	0.0962	0.2194	0.1801
MPE (%)	0.3491	1.0087	0.8247
MAPD (%)	0.4481	1.0203	0.8374
RMSE (°C)	0.1228	0.2722	0.2263

TABLE 4.1: Statistical Performance Evaluation of Time Series Models.

4.5.2 SFDA Algorithm Evaluation: Anomalies and Sensor Failure Detection

This section evaluates the SFDA algorithm by using the surface temperature and surface resistivity sensor data sourced from the instrumented sewer infrastructure. During the course of the sewer monitoring campaign, the surface temperature sensor and moisture sensor demonstrated robust behaviour and did not generate prolonged spurious data. However, the sensor has produced continuous stream of spurious data in the interim of laboratory evaluation. So, for evaluating the SFDA algorithm, we have injected random anomalies to the time series data along with the observed anomalies during the field testing. In addition, we have implanted continuous stream of spurious data on two different time periods of the field experimentation. For detecting the IRR sensor failure, the SFDA algorithm was trained by using the surface temperature data from 4^{th} to 10^{th} November 2016 and for detecting the moisture sensor failure, the SFDA algorithm was trained from 11^{th} to 20^{th} November 2016. For the IRR sensor, the first period is from 22^{nd} to 23^{rd} December 2016 and the second period is from 5^{th} to 6^{th} February 2017 to simulate sensor failure. Likewise, for the moisture sensor, the first period is from 16^{th} to 17^{th} December 2016 and the second period is from 5^{th} to 6^{th} February 2017.

Figures 4.10 and 4.11 illustrates the implementation of SFDA algorithm to demonstrate sensor failure detection, anomaly detection and isolation, and data accommodation process from 11^{th} November 2016 to 23^{rd} December 2016 and from 24^{th} December 2016 to 6^{th}

February 2017 respectively for the IRR sensor. In this regard, the first plot displays the SARIMA model forecast within the prediction interval and the second plot shows the sensor data with some random and continuous spurious measurements. By using the forecast and sensor data, the p-value is determined and presented in the third plot along with the critical value of 0.95. For the random and continuous spurious data, the p-value was observed to be lower than the critical value and finally in the last plot, the data accommodation process illustrating the replacement of faulty data is shown. The long-term monitoring performance of sensor data for detecting sensor failure is evaluated. Figure 4.12 displays the implementation of SFDA algorithm for long-term detection process between 11^{th} November 2016 and 6^{th} February 2017. Figures 4.13 and 4.14 illustrate the implementation of SFDA algorithm to demonstrate sensor failure detection, anomaly detection and isolation, and data accommodation process from 21^{st} November 2016 to 17^{th} December 2016 and from 29^{th} December 2016 to 6^{th} February 2017 respectively for the moisture sensor. During the field monitoring period on 2^{nd} February 2017 from 1:00 am to 12:00 pm, the moisture sensor data logging system was turned off. So, the sensor values cannot be recorded. Due to this reason, the SFDA algorithm gives probability value less than 0.95 in 4.13 on 2^{nd} February 2017. This issue should not be attributed to sensor failure. However, on evaluation, the SFDA algorithm reported the sensor failure warning and invoked data accommodation process. The forecasted data during that period was supplied to the training model of the SFDA algorithm to forecast the values for 3^{rd} February 2017.

To measure the detection performance of random and continuous spurious data, we use Successful Detection Rate (SDR) [126] as metrics. The SDR is expressed in terms of % and it is defined as follows:

$$SDR = \left[\frac{SD}{AM}\right] \times 100 \tag{4.21}$$

where SD is the number of successful detections and AM is the number of anomalous measurements. For IRR sensor, the SDR for the injected and observed anomalies of the periods from 11^{th} November 2016 to 23^{rd} December 2016 and from 24^{th} December 2016 to 6^{th} February 2017 were 100% and 93.34% respectively. The reason for the slightly

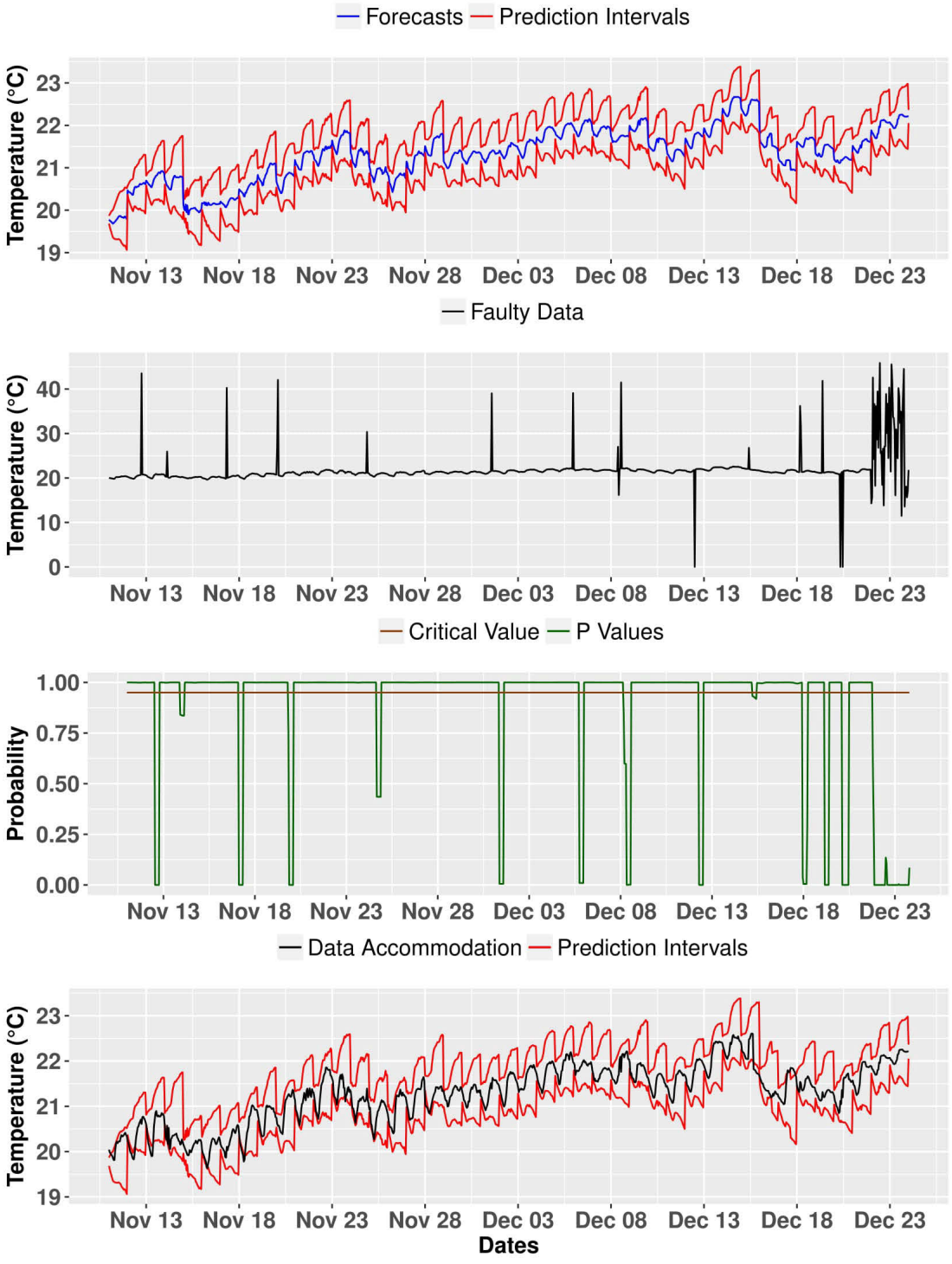

FIGURE 4.10: IRR Sensor: Short-term Evaluation-1 of SFDA algorithm.

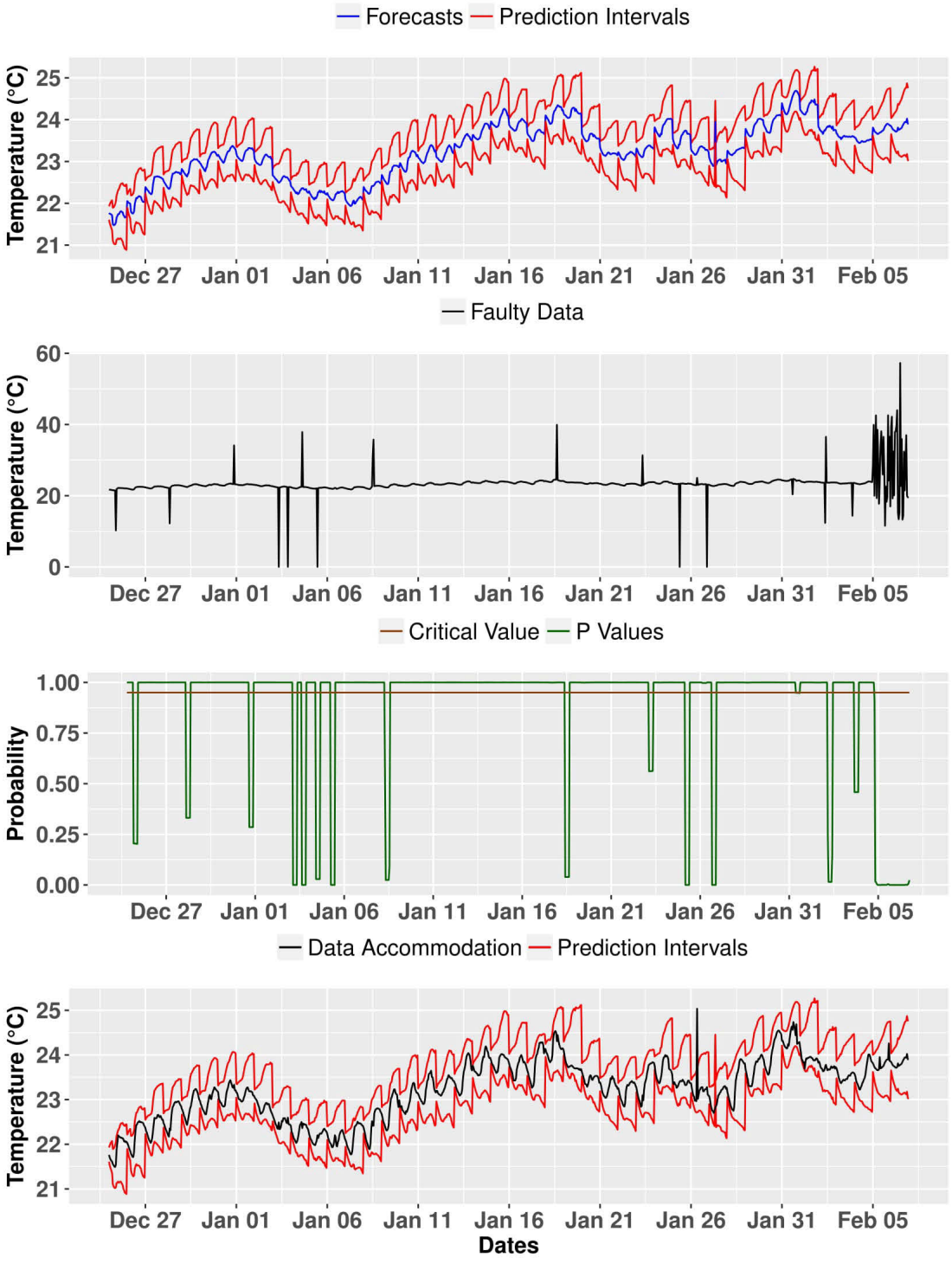

FIGURE 4.11: IRR Sensor: Short-term Evaluation-2 of SFDA algorithm.

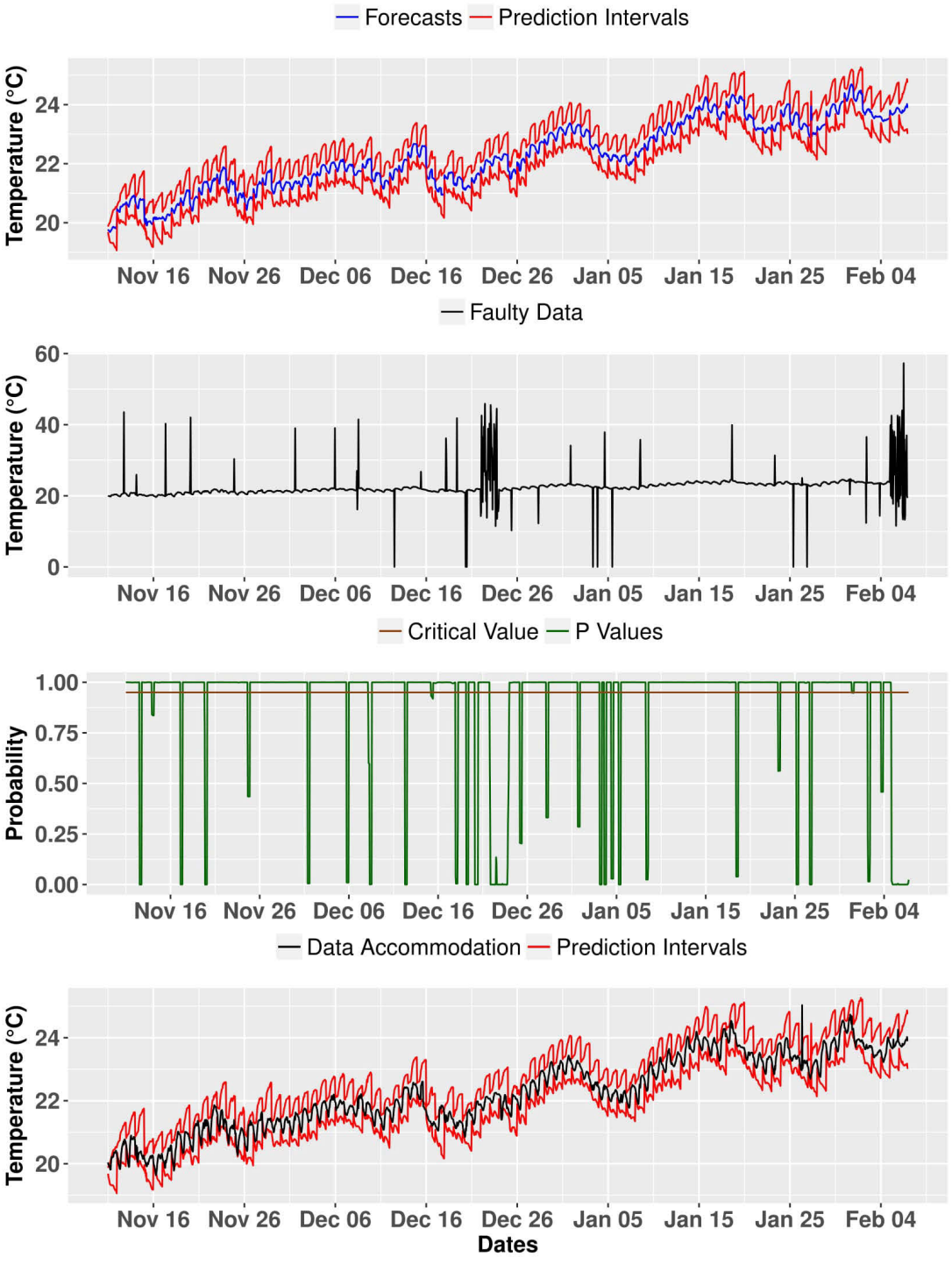

FIGURE 4.12: Long-term evaluation of SFDA algorithm.

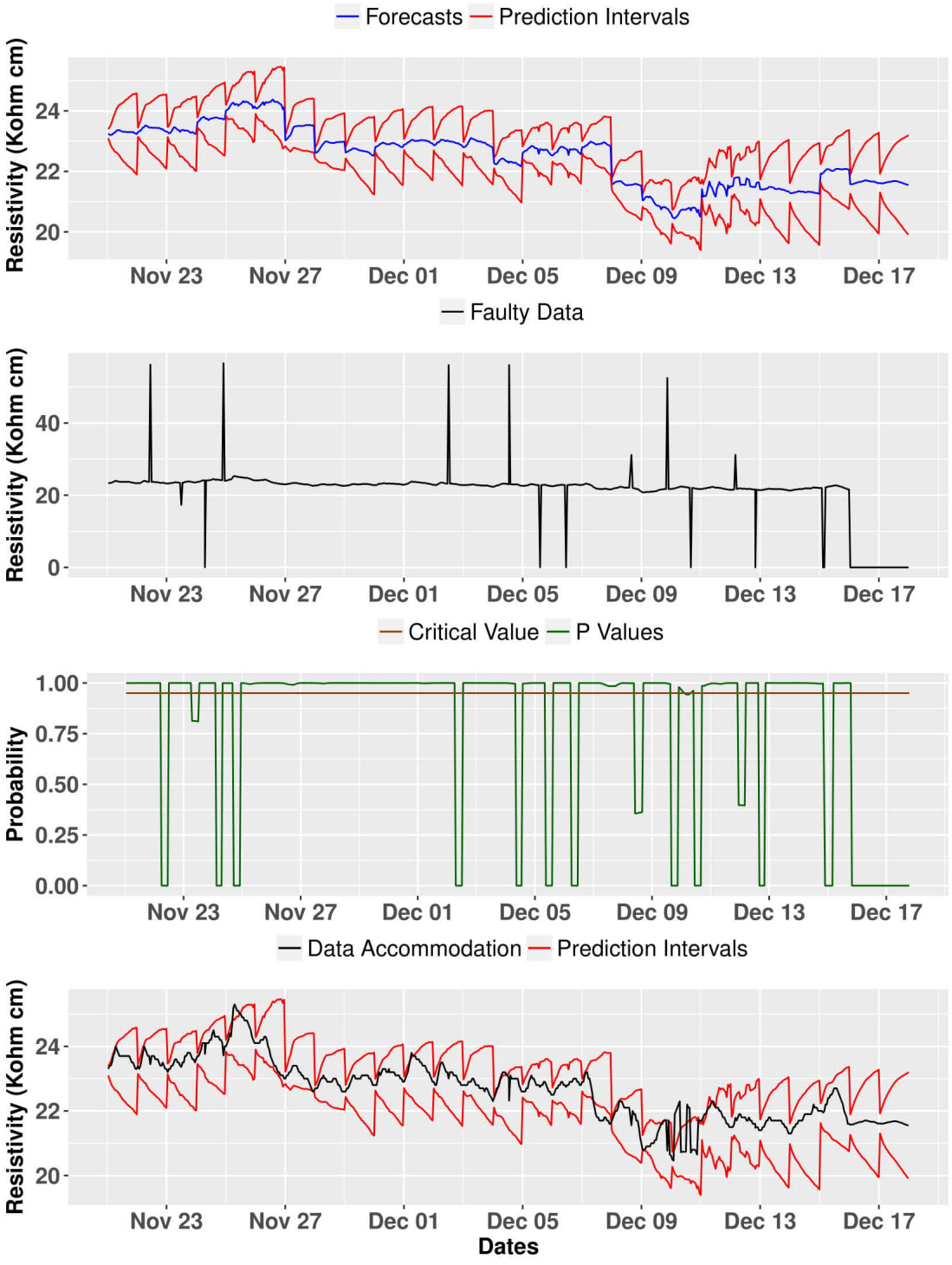

FIGURE 4.13: Moisture Sensor: Short-term Evaluation-1 of SFDA algorithm.

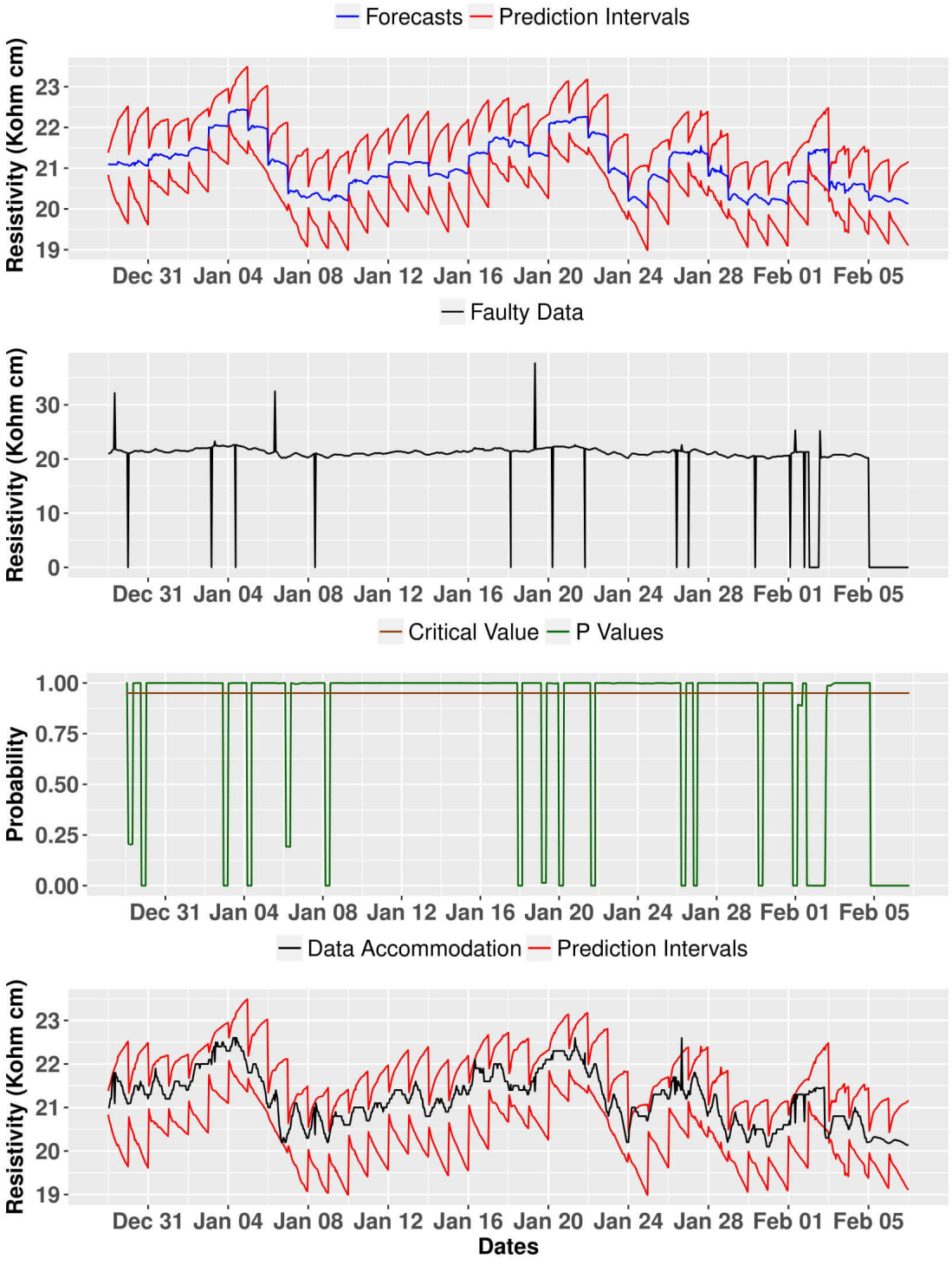

FIGURE 4.14: Moisture Sensor: Short-term Evaluation-2 of SFDA algorithm.

lower value of SDR in the latter period is due to the closeness of anomaly to the forecast value. In this case, the p-value remains to be higher than the critical value. The SFDA algorithm successfully detected anomalies including the two successive ones and thereby reported the anomalies with time-stamp and accommodated the corresponding forecast data. In the case of more than three anomalies present in a single window frame with no three successive spurious data, the SFDA algorithm issues sensor failure warning for early operator intervention. Further, the sensor failure detection was reported after the detection of three successive spurious data in a single window frame. Overall for the entire time period, the SDR is 97.06%. For the continuous spurious data on 22^{nd} to 23^{rd} December 2016 and 5^{th} to 6^{th} February 2017, the SDR were 100% for each period, indicating the SFDA performance efficacy of IRR sensor failure detection. Similarly, for the moisture sensor, the SDR for the periods from 21^{st} November 2016 to 17^{th} December 2016 and from 29^{th} December 2016 to 6^{th} February 2017 are 100% and 94.44% respectively. For the continuous spurious data on 16^{th} to 17^{th} December 2016 and 5^{th} to 6^{th} February 2017, the SDR were 100% for each period, indicating the SFDA performance efficacy of moisture sensor failure detection.

4.5.3 SFDA Algorithm Evaluation: Forecasting Performance

In order to evaluate the forecasting performance of the SARIMA model, we compared the forecasting data of two different periods with the anomalies-free sensor measurements of those respective periods. This evaluation was carried out on both surface temperature and resistivity data obtained from the sensor suite. For the surface temperature data, the first period is from 25^{th} to 30^{th} November 2016 and the second period is from 11^{th} to 16^{th} January 2017. Figure 4.15 presents the temporal profile of forecasted and IRR sensor measurements data. For the resistivity data, the first period is from 26^{th} November 2016 to 1^{st} December 2016 and the second period is from 12^{th} to 17^{th} January 2017. Figure 4.16 presents the temporal profile of forecasted and moisture sensor measurements data. From Figure 4.15 and Figure 4.16, it can be observed that the profile tends to follow a similar pattern to each other and this implies that the forecasted data generates a reasonable alternative to the sensor data.

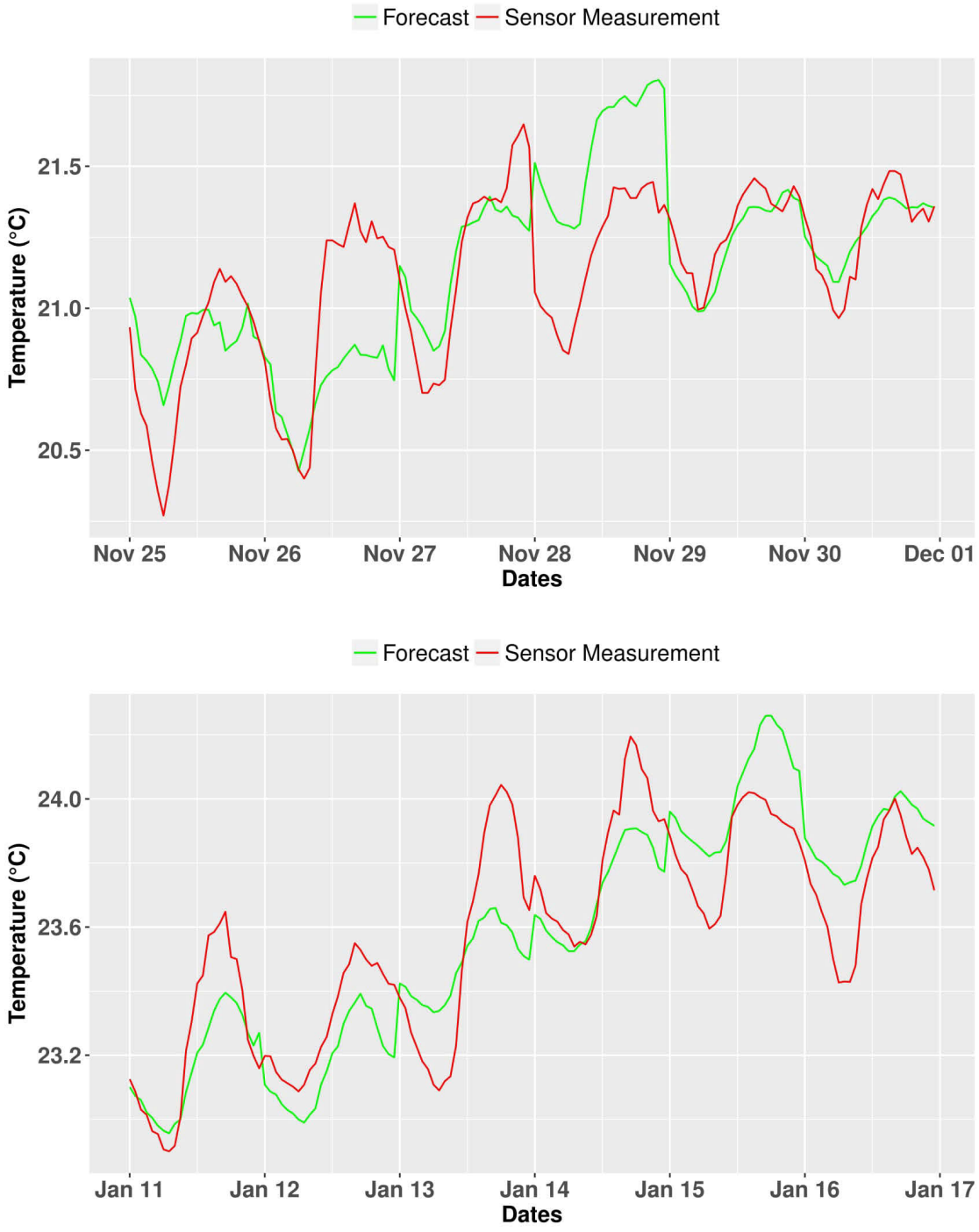

FIGURE 4.15: Illustration of SARIMA model forecasting performance of surface temperature data.

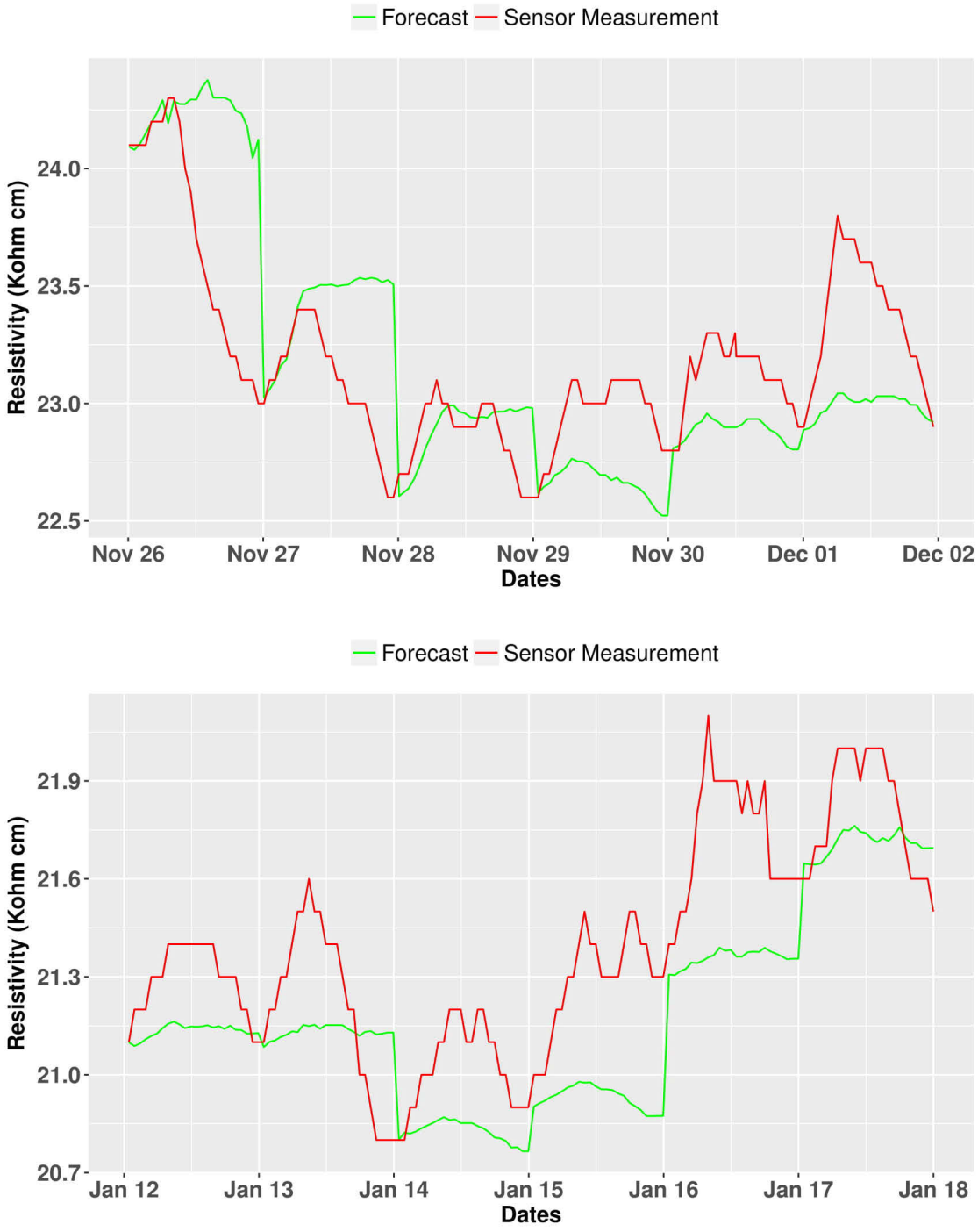

FIGURE 4.16: Illustration of SARIMA model forecasting performance of surface resistivity data.

The MAE, MAPE and RMSE were used as a statistical metric to evaluate the forecasting performance of the SARIMA model. The employed statistical metrics are computed by using the mathematical formula defined as follows:

$$MAE = \frac{1}{n}\sum_{t=1}^{n}\left|[R(t)]_i - [\hat{S}_{t+f}]_i\right| \tag{4.22}$$

$$MAPD = \frac{100\%}{n}\sum_{t=1}^{n}\left|\frac{[R(t)]_i - [\hat{S}_{t+f}]_i}{[R(t)]_i}\right| \tag{4.23}$$

$$RMSE = \sqrt{\frac{1}{N}\sum_{i=1}^{N}\left([R(t)]_i - [\hat{S}_{t+f}]_i\right)^2} \tag{4.24}$$

where $[\hat{S}_{t+f}]_i$ is the forecast value, $[R(t)]_i$ is the sensor value. Table 4.2 tabulates the computed statistical metrics for the period evaluated by using IRR sensor measurements and Table 4.3 tabulates the computed statistical metrics for the period evaluated by using moisture sensor measurements. This statistical evaluation presented in Table 4.2 and Table 4.3 demonstrates the higher accuracy of the SARIMA forecast model employed in this work.

IRR Sensor: Statistical Evaluation of SFDA Model's Forecasting Performance			
Period	MAE(°C)	MAPE(%)	RMSE(°C)
25^{th} to 30^{th} November 2016	0.1828	0.0086	0.2376
11^{th} to 16^{th} January 2017	0.1475	0.0062	0.1744

TABLE 4.2: IRR Sensor: Statistical Evaluation of SFDA Model's Forecasting Performance.

Moisture Sensor: Statistical Evaluation of SFDA Model's Forecasting Performance			
Period	MAE(kΩ cm)	MAPE(%)	RMSE(kΩ cm)
26th November 2016 to 1st December 2016	0.3188	0.0137	0.4247
12th to 17th January 2017	0.2476	0.0115	0.2901

TABLE 4.3: Moisture Sensor: Statistical Evaluation of SFDA Model's Forecasting Performance.

4.5.4 SFDA Algorithm Evaluation: Data Accommodation Process

Once the sensor failure is detected, the corresponding forecast data is utilized to replace the continuous spurious data. Figure 4.17 illustrates the data accommodation process once the IRR sensor failure has occurred and Figure 4.18 shows the data accommodation process after the detection of moisture sensor failure. Performance analysis on data accommodation process was carried out to determine MAE, MAPE and RMSE on the sensor failure period. The computed values for the IRR sensor and moisture sensor are tabulated in the Table 4.4 and 4.5 respectively.

From the Tables 4.4 and 4.5, the statistical performance analysis shows that the data accommodation process is providing reasonable data when the sensor generates spurious data. However, it can be observed from Figure 4.17 and Figure 4.18 that the difference between the sensor measurements and estimated values after sensor failure increases over time. This is mainly due to the reason that the SFDA algorithm is not supplied with the recent data to capture the daily temporal trends. Hence, the data accommodation process is recommended only for short-term period.

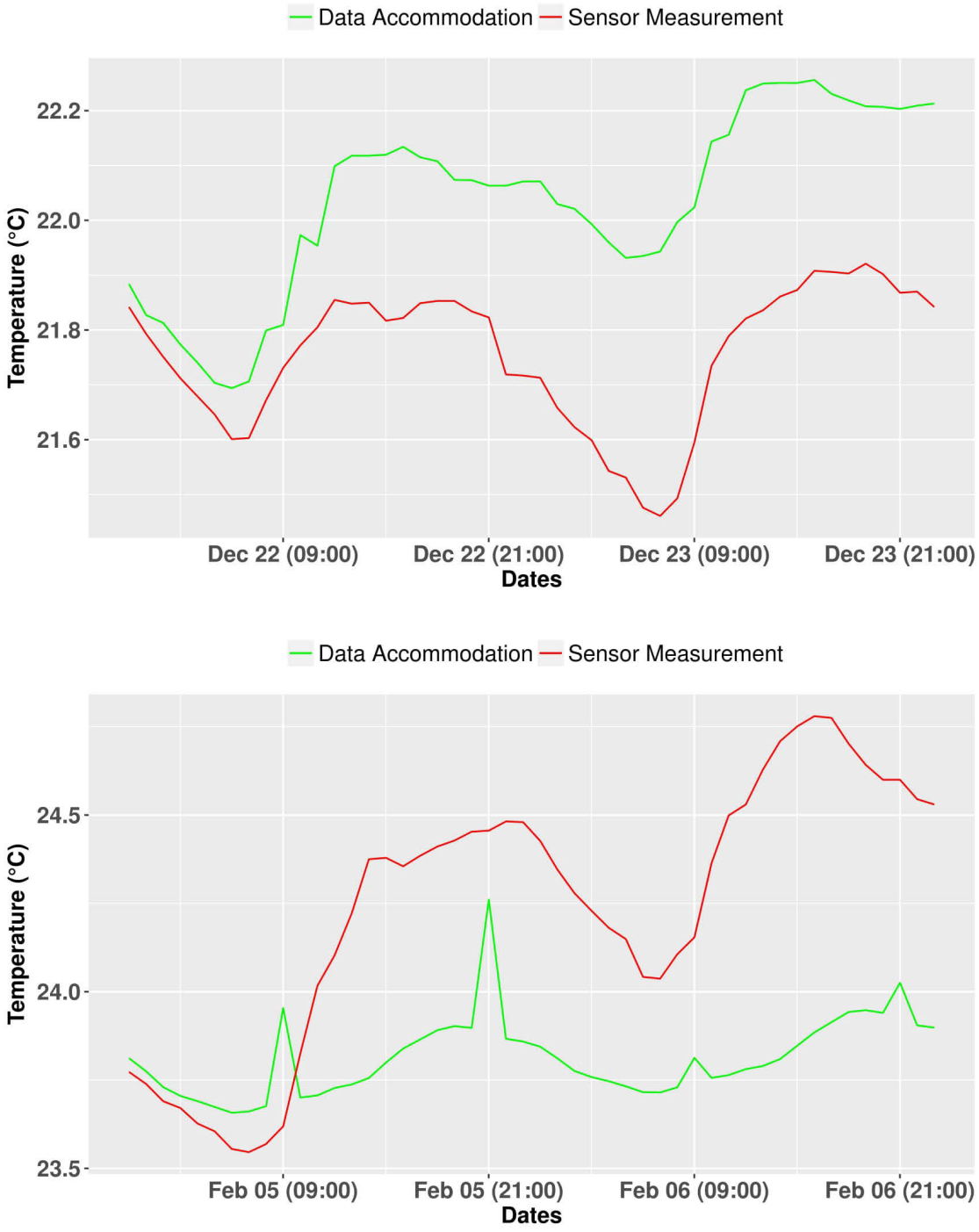

FIGURE 4.17: Illustration of the data accommodation during IRR sensor failure

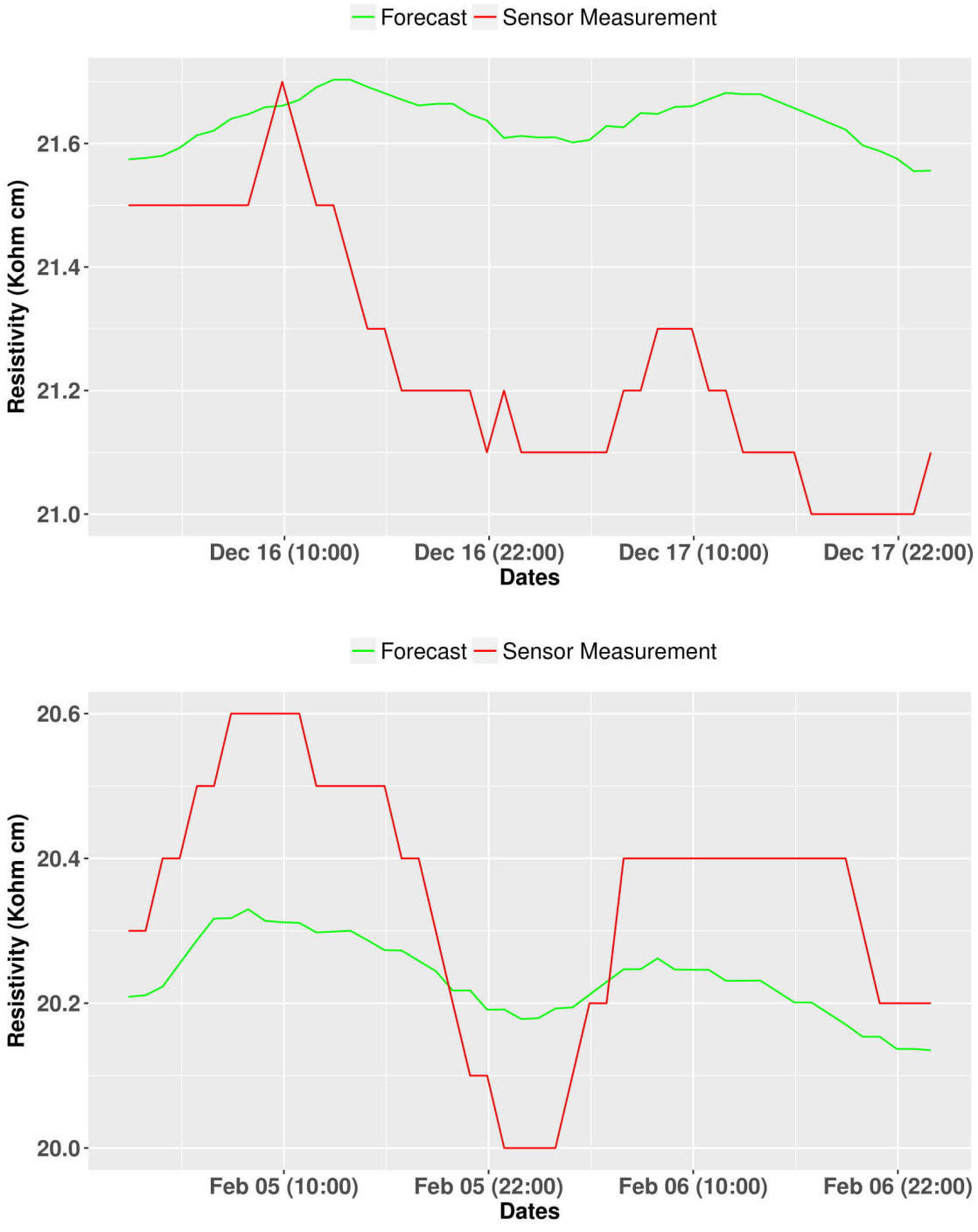

FIGURE 4.18: Illustration of the data accommodation during moisture sensor failure.

Evaluation of SFDA Model's Data Accommodation Process for IRR Sensor			
Sensor Failure Period	MAE(°C)	MAPE(%)	RMSE(°C)
19^{th} to 20^{th} December 2016	0.2832	0.0130	0.3115
5^{th} to 6^{th} February 2017	0.4637	0.0189	0.5297

TABLE 4.4: Evaluation of SFDA Model's Data Accommodation Process for IRR Sensor.

Evaluation of SFDA Model's Data Accommodation Process for Moisture Sensor			
Sensor Failure Period	MAE(kΩ cm)	MAPE(%)	RMSE(kΩ cm)
22^{nd} to 23^{rd} December 2016	0.3887	0.0183	0.4316
5^{th} to 6^{th} February 2017	0.1584	0.0077	0.1752

TABLE 4.5: Evaluation of SFDA Model's Data Accommodation Process for Moisture Sensor.

4.6 Summary

This chapter presented a smart predictive analytics framework for detecting the sensor failure based upon the real-time operational data sourced from an urban sewer system. In this context, the SFDA scheme using SARIMA model is proposed with sewer monitoring system as the application domain. The major contributions of the proposed scheme are enumerated as follows:

- The SARIMA model based forecasting of quantified sensing suite variable for sewer application was achieved to comprehend the temporal dynamics of the measured variable. This forecasting mechanism is used as a framework to provide an alternate measure to physical sensor measurements. The forecast data from the SARIMA

model was used as a reference measure in the SFDA algorithm to perform anomalies detection, early sensor failure detection and data accommodation.

- The early sensor failure detection through SFDA algorithm was implemented by utilizing smart predictive analytics approach through forecasting mechanism and statistical diagnostic method. While examining each sensor data, the SFDA algorithm checks for the presence of anomalies. In the event of detecting the anomalies, the algorithms isolate the spurious data and accommodate with the corresponding forecast data. Further, based on the continuity of faulty data, the early sensor failure is detected and data accommodation process is invoked to provide an alternate measure for computational model predicting sewer concrete corrosion.

- The SFDA algorithm was evaluated with the surface temperature and surface resistivity data sourced from the instrumented sewer infrastructure. The experimental evaluation demonstrates that the SFDA algorithm can detect anomalies and early sensor failure with high detection accuracy and efficiency. Also, on the event of sensor failure, the SFDA algorithm provides reliable estimates. The forecasting performance of the SFDA algorithm was investigated by comparing the estimates against the actual sensor measurements. From this investigation, it can be said that the forecasting performance is deemed satisfactory. Thus, the SFDA algorithm is applicable to the developed robust sensing suite for smart sewer monitoring application.

From the works presented in this chapter of the dissertation, the following publications resulted as an outcome.

- **K.Thiyagarajan**, S. Kodagoda, L.V. Nguyen, and R. Ranasinghe, "Sensor Failure Detection and Faulty Data Accommodation Approach for Instrumented Wastewater Infrastructures", IEEE Access. *(Under Review)*

- **K.Thiyagarajan**, S. Kodagoda, and L.V. Nguyen, "Predictive Analytics for Detecting Sensor Failure Using Autoregressive Integrated Moving Average Model,"

2017 IEEE 12th Conference on Industrial Electronics and Applications (ICIEA), Siem Reap, Cambodia, 2017, pp. 1923-1928.

Chapter 5

Conclusions

The objective of this dissertation is to develop robust sensor technologies to provide reliable measures of surface temperature and surface moisture conditions inside the concrete sewer pipes. In this context, the research work reported in this dissertation is the first study to prove the feasibility of measuring surface temperature in a non-contact way and surface moisture levels in a non-invasive way for an extended period inside the concrete sewer pipes with the motive of improving the current sewer monitoring capabilities.

This chapter presents the conclusions of this dissertation. The remainder of this chapter is structured as follows: Section 5.1 summarises the key contributions of this dissertation. Section 5.2 discusses the limitations of the proposed work. Section 5.3 presents the implications of this dissertation for water industry and finally, Section 5.4 addresses the future research prospects.

5.1 Summary of Contributions

This section highlights the key contributions in the field of sensor technologies presented in this dissertation. They are enumerated as follows:

1. Chapter 2 has developed a robust sensor technology for monitoring temporal dynamics of the surface temperature inside the sewer pipes. From the field testing

experiments, the study has revealed that the IRR sensor with an anti-fog coated germanium optical window can be used for non-contact surface temperature measurements in sewer systems. This sensor is more suited for deployments of about three months period continuously or can be used on moving platforms during human traversing. For long-term sensing operations using IRR sensor, it is recommended to replace or coat the optical window with anti-fog material after three months of use. On the other hand, the thermistor used was also reliable and was sufficiently robust to be deployed in a sewer environment. It is a contact type surface temperature measurement sensor, which can be used for long-term monitoring operations at the hot-spots areas.

2. Chapter 3 has developed a robust sensor technology for determining the temporal dynamics of the surface moisture conditions of the concrete sewer pipes. As an outcome of the field experiments conducted inside the sewer pipe, the study has demonstrated the feasibility of non-invasive determination of surface moisture conditions based on surface electrical resistivity measurements. The sensor survived three months of exposure to sewer conditions and the electrodes of the sensor exposed to sewer atmosphere have shown physical robustness to the deployed sewer conditions. The developed sensor technology measures through contact type sensing without damaging the surface conditions. This type of sensing is suited for both short-term and long-term monitoring applications.

3. Chapter 4 has developed a machine learning based diagnostic toolkit for instrumented sewer infrastructures. This toolkit has proposed an SFDA algorithm for an early detection of sensor failure by utilizing smart predictive analytics. The predictive algorithm of the diagnostic toolkit performs reliable forecasting of sensor variables, efficient detection of anomalies in the continuous stream of sensor data and subsequent isolation, effective detection of early sensor failure and finally, supplies reliable estimates of sensor data to prediction models in the event of sensor failure. The SFDA algorithm demonstrated its efficient performance when the toolkit was evaluated with the surface temperature and surface moisture data sourced from sewers by using the sensor technologies developed in Chapter 2 and Chapter 3.

5.2 Discussion of Limitations

Although there are several sensors commercially available to measure surface temperature variations, their suitability for in-sewer environment has not been investigated until now. This research study used two different types of temperature sensors: contact and non-contact. The IRR sensor with anti-fog coated germanium optical window was used for non-contact type measurements. There was a slight visual degradation observed on the anti-fog coated optical window after 96 days of exposure to the aggressively corrosive environmental conditions of the sewer. The degradations were in the initial stages around the edges of the optics and the central part remains unaffected. As a part of preventive maintenance, it is recommended to replace the lens once in three months for accurate measurements. Degradations on the lens may lead to factual measurement (temperature of the fog on lens) and error. On the other hand, the contact-type sensing using thermistors can be a cheaper option to measure surface temperature in sewer pipes.

From the post-deployment validation study on temperature sensors, it can be concluded that all the temperature sensors performed reasonably well in the sewer and the measurements generated by them were legitimate. However, there were few anomalies found during the trials. The surface temperature data from the IRR sensor contained 0.35% of anomalies whereas the data from the reference instrument thermistor contained 0.3%. The sewer air temperature variable measured from the thermistor sensor comprises of 0.3% of anomalies. All the anomalies were removed manually for computation and analysis in Chapter 2. Further, the IRR sensor data was improved by correcting the surface temperature measures through the determination of the emissivity coefficient. It can be further improved by determining the emissivity coefficient at regular intervals rather than at the seasonal periods. This study has only shown an approach to improve the surface temperature measure. Further study on determining the properties that determine emissivity will open the possibilities of improving the surface temperature measurement automatically.

In spite of the fact that there are various sensor technologies available off-the-shelf for quantifying concrete moisture conditions, their adaptability to waste water environments has not been studied until now. This research study utilized resipod meter for measuring

the surface resistivity of the concrete sewer pipe. Although the sensor has shown physical robustness to deployed sewer conditions, the measurements were found to be affected by nearby metals (rebar). Therefore, it needs an on-site calibration for estimating the moisture levels from resistivity values. In order to determine the surface moisture conditions automatically based on resistivity measurements, it is important to know the location of rebar inside the concrete pipe. Also, in the case of field evaluation, a commercially available sensor was used, which has a fixed operating frequency. However, the effects of rebar can be minimized by setting an appropriate operating frequency of the sensor, so that it limits the penetration of electric field into the concrete. In addition, a sensor placed perpendicular to the rebar during measurements experiences more influence of the rebar. Therefore, appropriate placement of sensor is recommended for determining the surface moisture conditions automatically without on-site calibration.

During the phase of field deployment, the resipod data logging system had an issue starting from the 21st December to the 28th December of 2016. This was apparently due to a suspected computer restart causing the data logging program to shut down. The data logging software was restarted after visiting the site on the 28th of December. From the post-deployment validation study, it can be concluded that the sensor was in working condition and the resistivity measurements from the sewer concrete surface were legitimate. However, the surface resistivity data contained 1.28% of anomalies. They were manually removed for computation and analysis which was conducted in Chapter 3.

For locating the presence of rebar inside the concrete, the laboratory study reported in this dissertation only focussed on a single rebar presence to demonstrate the feasibility. In future prospects, investigations will be conducted on the rebar mesh.

The sensor enclosure was visually inspected after the field trial campaign. No visual damage was apparent on the sensor enclosure other than a slight decoloration of the material. All the sensors survived the three months period of field trials and the measurements generated by the deployed sensors were reasonable. The sewer site used in this study has no access to any electrical mains. In order to operate the sensor system, other means of supplying power to the monitoring unit was necessary. The option of using solar panels was not preferred by the sewer operators mainly because of their past

experiences, where solar panels were damaged or removed by some external party. So, a DC battery was used to power the sensor system. Due to the high power consumption of the sensor system, the DC battery was replaced with the recharged ones every week throughout the field testing. The resistivity measurements were stored on ODROID based data logger, which was power hungry. To mitigate this issue, presently we are exploring the options of using micro-controller based data logging instrument. Also, every time the DC battery was swapped, the ODROID based data logger needed to be restarted to perform sensing and data logging at desired time intervals.

Finally, in the SFDA algorithm, it requires training data for a few days to forecast the trends of sensor variables. Presently, the algorithm uses 24 data per day for forecasting the subsequent day. This is the reason for the SFDA algorithm to forecast 24 steps ahead. This indeed increases the amount of data utilized for training the forecasting process. However, this concern may be addressed by incorporating mutual information feature between the data points and then forecasting the sensor data trends.

The sensor failure detection of the SFDA algorithm is set to a heuristic criterion, which is based on the continuity of faulty data three successive times or more. This criterion was based on the reason that the IRR sensor and resistivity meter are most unlikely going to produce more than 3 successive faulty data unless there is an issue with the sensing system itself. Hence, this is the reason for the continuity to be three or more successive times.

The size of the sliding window was heuristically chosen as 6 based on the knowledge of sensor characteristics and therefore, each window takes 6 sensor measurements.

5.3 Implications for the Water Industry

The data from the developed sensor technologies will be valuable to water utilities in identifying high-risk areas of the sewer pipes through model based predictions. It will also significantly improve the predictive accuracy of corrosion models by reducing the large uncertainties associated with data inputs used for corrosion model prediction. Consequently, this research enables water utilities to better manage their underground and aboveground sewer assets, whilst reducing on-going maintenances costs associated

with preventing sewer corrosion. For instance, Sydney Water Corporation, the main funding partner for the research pursued in this dissertation uses a 3 level sewer inspection process for asset renewals: i) L1: Prioritize with historical records, ii) L2: Visual inspection with sensor deployment and iii) L3: New design with an improved prediction model. The outcomes of this research will enable water utilities such as Sydney Water Corporation to make a better strategic decision on where to invest $50 Million per year at L1 and inspect at L2 for corrosion maintenance, whilst reducing asset maintenance and operational costs associated with chemical dosing and sewer pipe rehabilitation.

Overall, this dissertation has the potential to innovate the current sewer corrosion monitoring practice by improving the monitoring process and enabling a high-level of managing control across the sewer network in order to protect the concrete sewer pipes from structural failure and thereby support the economies and communities dependant on those essential services.

5.4 Future Research

Research work presented in this dissertation is intended to extend in the following directions:

- From the conducted research study, it is established that there are differences between the surface temperature and gaseous temperature conditions near the crown of the sewer pipe. This finding has led to discussions with Melbourne Water Corporation to investigate the temperature levels at different heights from the crown surface of the sewer pipe. This work may shed light on the corrosion occurrence at different locations of the confined concrete sewers.
- Surface Moisture measurements are influenced by the presence of rebar at different locations inside concrete. This concern may be addressed by developing a sensing mechanism by exploiting information-driven machine learning approaches that can estimate the depth of rebar by using surface resistivity data. Then, Gaussian

process regression modelling may be used to predict the surface moisture conditions by making rebar depth as one of the observations.

- The developed new robust sensor technologies along with H_2S sensor may be strategically deployed in sewer pipe locations where the concrete pipes are prone to a high-risk of corrosion; areas where there is at present low confidence of predictive modelling and feasibility for water utilities to install the sensors inside sewer pipes. The monitoring process after deployment can increase the sewer monitoring capabilities for water utilities.

- Presently, the SFDA algorithm utilizes equally spaced temporal data for training the forecasting process. In future, this process can be made to utilize only the most informative temporal data for training purposes. This will minimize the data used for training whilst attaining the forecasting trends. Then, the SFDA algorithm can be implemented in real-time to perform cognitive computing in cloud platforms.

Bibliography

[1] Introducing the 4th Generation SewerVUE Surveyor, 2015. URL `http://sewervue.com/long-range-pipe-inspection-tracked-robot-surveyor.html`.

[2] Csaba Ekes and Boriszlav Neducza. Robot Mounted GPR for Pipe Inspection. In *International Conference on Ground Penetrating Radar (GPR)*, Shanghai, China, 2012.

[3] A. N. Angelakis, D. Koutsoyiannis, and G. Tchobanoglous. Urban wastewater and stormwater technologies in ancient Greece. *Water Research*, 2005. ISSN 00431354. doi: 10.1016/j.watres.2004.08.033.

[4] SJ Burian and FG Edwards. Historical Perspectives of Urban Drainage. *Ninth International Conference on Urban Drainage*, 2002.

[5] Giovanni de Feo, George Antoniou, Hilal Franz Fardin, Fatma El-Gohary, Xiao Yun Zheng, Ieva Reklaityte, David Butler, Stavros Yannopoulos, and Andreas N. Angelakis. The historical development of sewers worldwide, 2014. ISSN 20711050.

[6] W. M. Olmstead and H Hamlin. Converting Portions of the Los Angeles Outfall Sewer into a Septic Tank. *Engineering News and American Railway Journal*, 44 (19):317–318, 1990.

[7] C D Parker. The Corrosion of Concrete 1. The isolation of a species of bacterium associated with the corrosion of concrete exposed to atmospheres containing hydrogen sulphide. *Australian Journal of Experimental Biology & Medical Science*, 23(2), 1945.

[8] C D Parker. The Corrosion of Concrete 2. The function of thiobacillus concretivorus (Nov.Spec.) in the corrosion of concrete exposed to atmospheres containing hydrogen sulphide. *Australian Journal of Experimental Biology & Medical Science*, 23(2), 1945.

[9] Richard Pomeroy and Fred D Bowlus. Progress report on sulfide control research. *Sewage Works Journal*, 18(4):597–640, 1946. ISSN 0096-9362.

[10] Kenneth B Tator. Preventing hydrogen sulfide and microbiologically influenced corrosion in wastewater facilities. *Materials performance*, 42(7):32–37, 2003. ISSN 0094-1492.

[11] Ji-Dong Gu, Tim E Ford, Neal S Berke, and Ralph Mitchell. Biodeterioration of concrete by the fungus Fusarium. *International biodeterioration & biodegradation*, 41(2):101–109, 1998. ISSN 0964-8305.

[12] Wolfgang Sand, Thierry Dumas, Serge Marcdargent, Albert Pugliese, and Jean-Louis Cabiron. Tests for biogenic sulfuric acid corrosion in a simulation chamber confirms the on site performance of calcium aluminate based concretes in sewage applications. In *Infrastructure: New Materials and Methods of Repair*, pages 35–55. ASCE, 1992.

[13] Anna Romanova, Asaad Faramarzi, Mojtaba Mahmoodian, and Morteza Alani. An evolutionary polynomial regression (EPR) model for prediction of H2S induced corrosion in concrete sewer pipes. 2014.

[14] Steve Barclay. Corrosion Protection of Sydney Water's Sewer Assets Using Sulfalock Higel, 2014.

[15] Tony Wells, Robert E Melchers, and Phil Bond. Factors involved in the long term corrosion of concrete sewers. *Australasian corrosion association proceedings of corrosion and prevention, Coffs Harbour, Australia*, 11, 2009.

[16] Arthur G Boon. Septicity in sewers: causes, consequences and containment. *Water Science and Technology*, 31(7):237–253, 1995. ISSN 0273-1223.

[17] Guangming Jiang, Jurg Keller, and Philip L Bond. Determining the long-term effects of H 2 S concentration, relative humidity and air temperature on concrete sewer corrosion. *Water research*, 65:157–169, 2014. ISSN 0043-1354.

[18] Antony P Joseph, Jrg Keller, Heriberto Bustamante, and Philip L Bond. Surface neutralization and H 2 S oxidation at early stages of sewer corrosion: Influence of temperature, relative humidity and H 2 S concentration. *Water research*, 46(13): 4235–4245, 2012. ISSN 0043-1354.

[19] P Wells and Robert E Melchers. Microbial Corrosion of Sewer Pipe in AustraliaInitial Field Results. In *18th International Corrosion Congress Proceedings November*. Citeseer, 2011.

[20] Lehua Zhang, Peter De Schryver, Bart De Gusseme, Willem De Muynck, Nico Boon, and Willy Verstraete. Chemical and biological technologies for hydrogen sulfide emission control in sewer systems: a review. *Water research*, 42(1):1–12, 2008. ISSN 0043-1354.

[21] Margarito Quintero-Núñez, Benjamin Valdez, and Michael Schorr. Effect of H2S on corrosion in polluted waters. In *Advanced Materials Research*, volume 95, pages 33–36. Trans Tech Publ, 2010. ISBN 0878492895.

[22] Ilje Pikaar, Keshab R Sharma, Shihu Hu, Wolfgang Gernjak, Jrg Keller, and Zhiguo Yuan. Reducing sewer corrosion through integrated urban water management. *Science*, 345(6198):812–814, 2014. ISSN 0036-8075.

[23] Esam Hewayde, M Nehdi, E Allouche, and G Nakhla. Effect of mixture design parameters and wetting-drying cycles on resistance of concrete to sulfuric acid attack. *Journal of Materials in Civil Engineering*, 19(2):155–163, 2007. ISSN 0899-1561.

[24] M P H Brongers, P Y Virmani, and J H Payer. Drinking water and sewer systems in corrosion costs and preventative strategies in the United States. *United States Department of Transportation Federal Highway Administration*, 2002.

[25] Gerhardus H Koch, Michiel P H Brongers, Neil G Thompson, Y Paul Virmani, and Joe H Payer. Corrosion cost and preventive strategies in the United States. Technical report, 2002.

[26] Esam Hewayde, M Nehdi, E Allouche, and G Nakhla. Effect of mixture design parameters and wetting-drying cycles on resistance of concrete to sulfuric acid attack. *Journal of Materials in Civil Engineering*, 19(2):155–163, 2007. ISSN 0899-1561.

[27] T Wells and R E Melchers. Modelling concrete deterioration in sewers using theory and field observations. *Cement and Concrete Research*, 77:82–96, 2015. ISSN 0008-8846.

[28] Yiwen Liu, Keshab R Sharma, Markus Fluggen, Kelly O'halloran, Sudhir Murthy, and Zhiguo Yuan. Online dissolved methane and total dissolved sulfide measurement in sewers. *Water research*, 68:109–118, 2015. ISSN 0043-1354.

[29] L S M Alwis, H Bustamante, K Bremer, B Roth, T Sun, and K Grattan. Evaluation of the durability and performance of FBG-based sensors for monitoring moisture in an aggressive gaseous waste sewer environment. *Journal of Lightwave Technology*, PP(99):1, 2016. ISSN 0733-8724. doi: 10.1109/JLT.2016.2593260.

[30] T Wells and R E Melchers. An observation-based model for corrosion of concrete sewers under aggressive conditions. *Cement and Concrete Research*, 61:1–10, 2014. ISSN 0008-8846.

[31] Yiqi Liu, Yarong Song, Jurg Keller, Philip Bond, and Guangming Jiang. Prediction of concrete corrosion in sewers with hybrid Gaussian processes regression model. *RSC Adv.*, 2017. ISSN 2046-2069. doi: 10.1039/C7RA03959J.

[32] Guangming Jiang, Jurg Keller, Philip L Bond, and Zhiguo Yuan. Predicting concrete corrosion of sewers using artificial neural network. *Water research*, 92:52–60, 2016. ISSN 0043-1354.

[33] Guangming Jiang, Jurg Keller, and Philip L Bond. Determining the long-term effects of H 2 S concentration, relative humidity and air temperature on concrete sewer corrosion. *Water research*, 65:157–169, 2014. ISSN 0043-1354.

[34] B. Li, X. Fan, J. Zhang, Y. Wang, F. Chen, S. Kodagoda, T. Wells, L. Vorreiter, D. Vitanage, G. Iori, D. Cunningham, and T. Chen. Predictive Analytics Toolkit for H2S Estimation and Sewer Corrosion. In *OZWater*, Sydney, 2017. Australian Water Association.

[35] Anna Romanova, Mojtaba Mahmoodian, and Morteza A Alani. Influence and interaction of temperature, H2S and pH on concrete sewer pipe corrosion.

International Journal of Civil, Architectural, Structural, Urban Science and Engineering, 8(6):592–595, 2014. ISSN 1307-6892.

[36] O A C Hoes, R P S Schilperoort, W M J Luxemburg, FHLR Clemens, and N C Van De Giesen. Locating illicit connections in storm water sewers using fiber-optic distributed temperature sensing. *Water research*, 43(20):5187–5197, 2009. ISSN 0043-1354.

[37] C de Haan, J G Langeveld, R P S Schilperoort, and M Klootwijk. Locating and classifying illicit connections with Distributed Temperature Sensing. In *12th International Conference on Urban Drainage, Porto Alegre/Brazil*, 2011.

[38] Jaap Nienhuis, Cornelis De Haan, J G Langeveld, Martijn Klootwijk, and FHLR Clemens. Assessment of detection limits of fiber-optic distributed temperature sensing for detection of illicit connections. In *9th International Conference on Urban Drainage Modelling, Belgrade, Serbia, 4-6 September 2012*. IAHR/IWA Joint Committee Urban Drainage, Working Group on Data and Models, 2012.

[39] K Thiyagarajan, S Kodagoda, and J K Alvarez. An instrumentation system for smart monitoring of surface temperature. In *2016 14th International Conference on Control, Automation, Robotics and Vision (ICARCV)*, pages 1–6, 2016. doi: 10.1109/ICARCV.2016.7838845.

[40] K Thiyagarajan and S Kodagoda. SMART monitoring of surface temperature and moisture content using multisensory data fusion. In *2015 IEEE 7th International Conference on Cybernetics and Intelligent Systems (CIS) and IEEE Conference on Robotics, Automation and Mechatronics (RAM)*, pages 222–227, 2015. ISBN 2326-8123. doi: 10.1109/ICCIS.2015.7274624.

[41] K Thiyagarajan, S Kodagoda, and N Ulapane. Data-driven machine learning approach for predicting volumetric moisture content of concrete using resistance sensor measurements. In *2016 IEEE 11th Conference on Industrial Electronics and Applications (ICIEA)*, pages 1288–1293, 2016. doi: 10.1109/ICIEA.2016.7603783.

[42] P A Tipler and G Mosca. *Physics for Scientists and Engineers*. 2008.

[43] John G. Webster and H. Eren. *Measurement, Instrumentation and Sensors. The Handbook*. 1999. ISBN 0-8493-2145-X. doi: 10.1017/CBO9781107415324.004.

[44] Walt Jung. *Op Amp Applications Handbook*. 2005. ISBN 9780750678445. doi: 10.1016/B978-0-7506-7844-5.X5109-1.

[45] D D Pollock. Thermocouples: Theory and Properties. *Boca Raton, FL: CRC Press*, 1991.

[46] C Mansley, J Connell, C Isci, J Lenchner, J O Kephart, S McIntosh, and M Schappert. Robotic mapping and monitoring of data centers. In *2011 IEEE International Conference on Robotics and Automation*, 2011. doi: 10.1109/ICRA.2011.5980554.

[47] A. Gontean, R. Szabo, and I. Lie. Surface temperature measurement with thermocouple matrix using a switch control unit. In *Design and Technology in Electronic Packaging (SIITME), 2012 IEEE 18th International Symposium*, page 283288, 2012.

[48] S. D. Wood, B. W. Mangum, J. J. Filliben, and S. B. Tillett. An investigation of the stability of thermistors. *Journal of Research of the National Bureau of Standards*, 1978. ISSN 0160-1741. doi: 10.6028/jres.083.015.

[49] Xavier P. Maldague. *Theory and Practice of Infrared Technology for Nondestructive Testing*. Wiley, New York, 2001. ISBN 978-0-471-18190-3.

[50] Michael F. Modest. *Radiative Heat Transfer*. 2013. ISBN 9780123869449. doi: 10.1016/C2010-0-65874-3.

[51] M. Vollmer and K.-P. Möllmann. *Infrared Thermal Imaging: Fundamentals, Research and Applications*. 2010. ISBN 9783527407170. doi: 10.1002/9783527630868.

[52] Stephen Vidas, Peyman Moghadam, and Michael Bosse. 3D thermal mapping of building interiors using an RGB-D and thermal camera. In *Robotics and Automation (ICRA), 2013 IEEE International Conference on*, pages 2311–2318. IEEE, 2013. ISBN 1467356417.

[53] J. Tanaka, M. Shiozaki, F. Aita, T. Seki, and M. Oba. Thermopile infrared array sensor for human detector application. In *Proceedings of the IEEE International Conference on Micro Electro Mechanical Systems (MEMS)*, 2014. ISBN 9781479935086. doi: 10.1109/MEMSYS.2014.6765866.

[54] A. Emadi, H. Wu, S. Grabarnik, G. De Graaf, and R. F. Wolffenbuttel. Infrared thermopile detector array for the integrated micro spectrometer. In *Proceedings of IEEE Sensors*, 2007. ISBN 1424412617. doi: 10.1109/ICSENS.2007.4388429.

[55] Terumi Inagaki and Yoshizo Okamoto. Surface temperature measurement near ambient conditions using infrared radiometers with different detection wavelength bands by applying a grey-body approximation: Estimation of radiative properties for non-metal surfaces. *NDT and E International*, 1996. ISSN 09638695. doi: 10.1016/S0963-8695(96)00039-4.

[56] P Lecomte, P Y Deschamps, and J C Vanhoutte. Reducing Error in the Measurement of Ocean Surface Temperature by Using an Infrared Radiometer with a Polarizer. . *Applied Optics*, 1973.

[57] SI-111: Standard Field of View Infrared Radiometer Sensor. URL `https://www.apogeeinstruments.co.uk/standard-field-of-view-infrared-radiometer-sensor-si-111/`.

[58] S Yin. Fiber Optic Sensors and Applications IX. In *Fiber Optic Sensors and Applications IX*, 2012. ISBN 0277786X; 9780819490483 (ISBN).

[59] Raman Kashyap. *Fiber Bragg Gratings (C4)*. 2010. ISBN 9780123725790. doi: 10.1016/B978-0-12-372579-0.00004-1.

[60] S Asher and R Bormett. Chapter 2. Raman instrumentation. In *Raman Scattering in Materials Science*. 2013. ISBN 3662042215.

[61] John Crisp and Barry Elliott. *Introduction to Fiber Optics*. 2005. ISBN 9780750667562. doi: 10.1016/B978-0-7506-6756-2.X5000-5.

[62] R P S Schilperoort and FHLR Clemens. Fibre-optic distributed temperature sensing in combined sewer systems. *Water Science and Technology*, 60(5):1127, 2009. ISSN 0273-1223.

[63] Devices Fiber Optics Handbook, Fiber, E Systems for Optical CommunicationBass, and E.W. Van Stryland. Fiber Optics Handbook, Fiber, Devices and Systems for Optical Communication. *Networks*, 2002.

[64] T Wells and R E Melchers. Modelling concrete deterioration in sewers using theory and field observations. *Cement and Concrete Research*, 77:82–96, 2015. ISSN 0008-8846.

[65] SIF-100 Series Fast-Response Infrared Radiometers, 2017. URL `http://www.ictinternational.com/products/sif-100-series-fast-response-infrared-radiometers/sif-100-series-fast-response-infrared-radiometers/?from=/supplier/apogee/plants/infrared-temperature-sensors/`.

[66] THERM-EP Epoxy Thermistor, 2017. URL `http://www.ictinternational.com/products/therm-ep/therm-ep-epoxy-thermistor/`.

[67] Kathryn L. Van Alstyne and Theresa K. Olson. Estimating variation in surface emissivities of intertidal macroalgae using an infrared thermometer and the effects on temperature measurements. *Marine Biology*, 2014. ISSN 00253162. doi: 10.1007/s00227-014-2429-3.

[68] Chiachung Chen. Determining the Leaf Emissivity of Three Crops by Infrared Thermometry. *Sensors*, 15(5):11387–11401, 2015.

[69] Tony Wells. Identification of controlling factors for the corrosion rate of concrete. Technical report, Centre for Infrastructure Performance and Reliability, The University of Newcastle, 2016. URL `https://score.org.au/++theme++/score-kms/Reports/SP1/Final%20report%20SP1B.pdf`.

[70] Il Choi, Hyunjoo Lee, Joungdu Shin, and Hyunook Kim. Evaluation of the effectiveness of five odor reducing agents for sewer system odors using an on-line

total reduced sulfur analyzer. *Sensors (Switzerland)*, 2012. ISSN 14248220. doi: 10.3390/s121216892.

[71] J Hur, B-M Lee, T-H Lee, and D-H Park. Estimation of biological oxygen demand and chemical oxygen demand for combined sewer systems using synchronous fluorescence spectra. *Sensors*, 2010. ISSN 1424-8220. doi: 10.3390/s100402460.

[72] Yiwen Liu, Keshab R Sharma, Sudhir Murthy, Ian Johnson, Ted Evans, and Zhiguo Yuan. On-line monitoring of methane in sewer air. *Scientific reports*, 4:6637, 2014. doi: 10.1038/srep06637 http://www.nature.com/articles/srep06637#supplementary-information.

[73] P Wells and Robert E Melchers. Microbial Corrosion of Sewer Pipe in AustraliaInitial Field Results. In *18th International Corrosion Congress Proceedings November*. Citeseer, 2011.

[74] K Bremer, M Meinhardt-Wollweber, T Thiel, G Werner, T Sun, K T V Grattan, and B Roth. Sewerage tunnel leakage detection using a fibre optic moisture-detecting sensor system. *Sensors and Actuators A: Physical*, 220:62–68, 2014. ISSN 0924-4247.

[75] American Society for Testing, Materials, United States of America Standards Institute, and American Association of State Highway Officials. *Standard Method of Test for Surface Moisture in Fine Aggregate*. American Society for Testing and Materials, 1967. URL `https://books.google.com.au/books?id=voKmnQEACAAJ`.

[76] K.M. DeAngelis. Measurement of soil moisture content by gravimetric method. Technical report, American Society of Agronomy, 2007.

[77] Jana Šelih, Antonio C.M. Sousa, and Theodore W. Bremner. Moisture transport in initially fully saturated concrete during drying. *Transport in porous media*, 1996. ISSN 0169-3913. doi: 10.1007/BF00175604.

[78] J C. Amba, J P. Balayssac, and C H Détriché. Characterisation of differential shrinkage of bonded mortar overlays subjected to drying. *Materials and Structures*, 43(1):297, 3 2009. ISSN 1871-6873. doi: 10.1617/s11527-009-9489-8.

[79] S. Multon, E. Merliot, Michel Joly, and Francois Toutlemonde. Water distribution in beams damaged by Alkali-Silica Reaction: global weighing and local gammadensitometry. *Materials and Structures*, 2004. ISSN 1359-5997.

[80] L J Parrott. *A review of methods to determine the moisture conditions in concrete.* 1990. ISBN 0721013961.

[81] Rob B Polder. Test methods for on site measurement of resistivity of concretea RILEM TC-154 technical recommendation. *Construction and building materials*, 15 (2):125–131, 2001. ISSN 0950-0618.

[82] Lianzhen Xiao and Zongjin Li. Early-age hydration of fresh concrete monitored by non-contact electrical resistivity measurement. *Cement and Concrete Research*, 38 (3):312–319, 2008. ISSN 0008-8846.

[83] Md Nazmul Alam, Rashed H Bhuiyan, Roger Dougal, and Mohammod Ali. Concrete moisture content measurement using interdigitated near-field sensors. *Sensors Journal, IEEE*, 10(7):1243–1248, 2010. ISSN 1530-437X.

[84] Anton Fuchs, Hubert Zangl, and Gert Holler. Capacitance-based sensing of material moisture in bulk solids: Applications and restrictions. In *Lecture Notes in Electrical Engineering*, 2008. ISBN 9783540795896. doi: 10.1007/978-3-540-79590-2-16.

[85] Hinrich Römhild. Microwave-Resonator-Based Sensors: An Accurate Solution for Measuring the Water Content in Paper. Technical report, Sensorsmag, 2012.

[86] S B Jones, J M Wraith, and Dani Or. Time domain reflectometry measurement principles and applications. *Hydrological Processes*, 2002.

[87] H Tian, L Ye, and H Chen. Study on effect of soil temperature on FDR soil moisture sensor in frozen soil. In *Proceedings of SPIE - The International Society for Optical Engineering*, 2013. doi: 10.1117/12.2019726.

[88] Ye Linmao, Xue longqin, Zhang guangzhou, Chen haibo, Shi likuai, Wu zhigang, Yu gouhe, Wang yanbin, Niu sujun, Ye Jin, and Jin Qi. FDR Soil Moisture Sensor for Environmental Testing and Evaluation. *Physics Procedia*, 2012. ISSN 18753892. doi: 10.1016/j.phpro.2012.03.271.

[89] L. Alwis, T. Sun, and K. T.V. Grattan. Optical fibre-based sensor technology for humidity and moisture measurement: Review of recent progress, 2013. ISSN 02632241.

[90] T. Venugopalan, T. Sun, and K. T.V. Grattan. Long period grating-based humidity sensor for potential structural health monitoring. *Sensors and Actuators, A: Physical*, 2008. ISSN 09244247. doi: 10.1016/j.sna.2008.07.015.

[91] Slade, Jeremiah, et al. "Humidity sensor and method for monitoring moisture in concrete., 2006.

[92] D Matthew, Zachary C. Grasley, David A. Lange, Matthew D. D'Ambrosia, and Salvador Villalobos-Chapa. Relative Humidity in Concrete. *Concrete International*, 2006. ISSN 01624075.

[93] T.L. Yeo, T. Sun, K.T.V. Grattan, D. Parry, R. Lade, and B.D. Powell. Characterisation of a polymer-coated fibre Bragg grating sensor for relative humidity sensing. *Sensors and Actuators B: Chemical*, 2005. ISSN 09254005. doi: 10.1016/j.snb.2005.01.033.

[94] Qamar A. Shams, Jr. Cecil G. Burkett, Taumi S. Daniels, George Tsoucalas, Toby Comeaux, and Bradley S. Sealey. Characterization of Polymer-Coated Mems Humidity Sensors for Flight Applications. Technical report, NASA, 2005.

[95] Zhu Wenjing, Mao Hanping, Zhou Ying, and Zhang Xiaodong. Hyperspectral imaging technology of nitrogen status diagnose for tomato leaves. *()*, 2014.

[96] N. Sanchez, J. Martinez-Fernandez, M. Piles, A. Camps, M. Vall-Llossera, and A. Aguasca. Hyperspectral-derived indices for soil moisture estimation at very high resolution. In *International Geoscience and Remote Sensing Symposium (IGARSS)*, 2014. ISBN 9781479957750. doi: 10.1109/IGARSS.2014.6947082.

[97] Nilda Sánchez, Maria Piles, Jos Martínez-Fernández, Merc Vall-llossera, Luca Pipia, Adriano Camps, Albert Aguasca, Fernando Pérez-Aragüés, and Carlos M. Herrero-Jiménez. Hyperspectral Optical, Thermal, and Microwave L-Band Observations For Soil Moisture Retrieval at Very High Spatial Resolution. *Photogrammetric Engineering & Remote Sensing*, 2014. ISSN 00991112. doi: 10.14358/PERS.80.8.745.

[98] Robert T Kester, Liang Gao, and Tomasz S Tkaczyk. Development of image mappers for hyperspectral biomedical imaging applications. *Applied optics*, 2010. ISSN 1539-4522. doi: 10.1364/AO.49.001886.

[99] F. Racek, T. Baláž, and P. Melša. Hyperspectral data conversion in the case of military surveillance. *Advances in Military Technology*, 2015. ISSN 18022308.

[100] Raghav Khanna, Inkyu Sa, Juan Nieto, and Roland Siegwart. On field radiometric calibration for multispectral cameras. In *Proceedings - IEEE International Conference on Robotics and Automation*, 2017. ISBN 9781509046331. doi: 10.1109/ICRA.2017.7989768.

[101] Xun Cao, Tao Yue, Xing Lin, Stephen Lin, Xin Yuan, Qionghai Dai, Lawrence Carin, and David J. Brady. Computational Snapshot Multispectral Cameras: Toward dynamic capture of the spectral world, 2016. ISSN 10535888.

[102] Audrey Lesaignoux, Sophie Fabre, Xavier Briottet, and Albert Olioso. Soil moisture impact on lab measured reflectance of bare soils in the optical domain [0.4 - 15 μM]. In *International Geoscience and Remote Sensing Symposium (IGARSS)*, 2009. ISBN 9781424433957. doi: 10.1109/IGARSS.2009.5417807.

[103] Farshad Rajabipour, Gaurav Sant, and Jason Weiss. Development of electrical conductivity-based sensors for health monitoring of concrete materials. In *TRB Annual Conference*, page 16, 2007.

[104] L J Parrott. *A review of methods to determine the moisture conditions in concrete*. 1990. ISBN 0721013961.

[105] Lianzhen Xiao and Zongjin Li. Early-age hydration of fresh concrete monitored by non-contact electrical resistivity measurement. *Cement and Concrete Research*, 38 (3):312–319, 2008. ISSN 0008-8846.

[106] Carl Edward Rasmussen. Gaussian processes for machine learning. 2006.

[107] Nalika N B Ulapane and Sunil G Abeyratne. Gaussian process for learning solar panel maximum power point characteristics as functions of environmental conditions.

In *Industrial Electronics and Applications (ICIEA), 2014 IEEE 9th Conference on*, pages 1756–1761. IEEE, 2014. ISBN 1479943169.

[108] Resipod Surface Resistivity Meter. *www.forconstructionpros.com*, 2011.

[109] Alena Mudroch, Jos M Azcue, and Paul Mudroch. *Manual of physico-chemical analysis of aquatic sediments*. CRC Press, 1996. ISBN 1566701554.

[110] L J Parrott. *A review of methods to determine the moisture conditions in concrete*. 1990. ISBN 0721013961.

[111] Karthick Thiyagarajan and Sarath Kodagoda. Analytical Model and Data-driven Approach for Concrete Moisture Prediction. In *33rd International Symposium on Automation and Robotics in Construction (ISARC 2016)*, pages 298–306, Auburn, 2016. IAARC.

[112] Sathira Wickramanayake Mudalige Don. Design and development of a resistivity measuring device for structural health monitoring. page 68, 2017.

[113] Linh V. Nguyen, Sarath Kodagoda, and Ravindra Ranasinghe. Spatial Sensor Selection via Gaussian Markov Random Fields. *IEEE Transactions on Systems, Man, and Cybernetics: Systems*, 2016. ISSN 10834427. doi: 10.1109/TSMC.2015.2503382.

[114] Havard Rue and Leonhard Held. *Gaussian Markov Random Fields*. CRC Press, 2005. ISBN 1584884320. doi: 10.1007/s00184-007-0162-3.

[115] R Ranasinghe and S Kodagoda. Spatial prediction in mobile robotic wireless sensor networks with network constraints. In *2016 14th International Conference on Control, Automation, Robotics and Vision (ICARCV)*, pages 1–6. IEEE, 2016.

[116] L V Nguyen, S Kodagoda, R Ranasinghe, and G Dissanayake. Mobile robotic wireless sensor networks for efficient spatial prediction. *2014 IEEE/RSJ International Conference on Intelligent Robots and Systems*, 2014. ISSN 2153-0858. doi: 10.1109/IROS.2014.6942706.

[117] Finn Lindgren, Hvard Rue, and Johan Lindström. An explicit link between gaussian fields and gaussian markov random fields: The stochastic partial differential equation

approach. *Journal of the Royal Statistical Society. Series B: Statistical Methodology*, 2011. ISSN 13697412. doi: 10.1111/j.1467-9868.2011.00777.x.

[118] Peter J Diggle and Paulo J Ribeiro Jr. An overview of model-based geostatistics. In *Model-based Geostatistics*. 2006. ISBN 978-0-387-32907-9, 978-0-387-48536-2. doi: 10.1111/j.1541-0420.2008.01026_3.x.

[119] P.J. Diggle and P.J. Ribeiro Jr. Gaussian models for geostatistical data. *Model-based Geostatistics*, 2007. doi: 10.1007/978-0-387-48536-2_3.

[120] Finn Lindgren, Hvard Rue, and Johan Lindström. An explicit link between gaussian fields and gaussian markov random fields: The stochastic partial differential equation approach. *Journal of the Royal Statistical Society. Series B: Statistical Methodology*, 2011. ISSN 13697412. doi: 10.1111/j.1467-9868.2011.00777.x.

[121] Alfio Quarteroni and Alberto Valli. Numerical Approximation of Partial Differential Equations (Springer Series in Computational Mathematics). *Springer Series in Computational Mathematics*, 1996. doi: 10.1007/978-3-540-85268-1.

[122] C. M. Bishop. Pattern Recognition and Machine Learning. In *Pattern Recognition and Machine Learning*. 2006. ISBN 0387310738. doi: 10.1117/1.2819119.

[123] Dennis S. Bernstein. Matrix mathematics: Theory, facts, and formulas with application to linear systems Theory, 2006. ISSN 1066033X.

[124] Douglas Tomlinson, Farid Moradi, Hamzeh Hajiloo, Pouria Ghods, Aali Alizadeh, and Mark Green. Early age electrical resistivity behaviour of various concrete mixtures subject to low temperature cycling. *Cement and Concrete Composites*, 2017. ISSN 09589465. doi: 10.1016/j.cemconcomp.2017.07.028.

[125] Shen Yin, Steven X Ding, and Donghua Zhou. Diagnosis and prognosis for complicated industrial systems-Part I. *IEEE Transactions on Industrial Electronics*, 63(4):2501–2505, 2016.

[126] Po Yu Chen, Shusen Yang, and Julie A. McCann. Distributed real-time anomaly detection in networked industrial sensing systems. *IEEE Transactions on Industrial Electronics*, 2015. ISSN 02780046. doi: 10.1109/TIE.2014.2350451.

[127] Liu Yi, Xu Ke, and Song Junde. Research on forecasting and early-warning methods. In *Proceedings - IEEE 9th International Conference on Mobile Ad-Hoc and Sensor Networks, MSN 2013*, 2013. ISBN 9780768551593. doi: 10.1109/MSN.2013.57.

[128] Animesh Patcha and Jung Min Park. An overview of anomaly detection techniques: Existing solutions and latest technological trends. *Computer Networks*, 2007. ISSN 13891286. doi: 10.1016/j.comnet.2007.02.001.

[129] Ihab Samy, Ian Postlethwaite, and Da Wei Gu. Detection and accommodation of sensor faults in UAVs - A comparison of NN and EKF based approaches. In *Proceedings of the IEEE Conference on Decision and Control*, 2010. ISBN 9781424477456. doi: 10.1109/CDC.2010.5716956.

[130] C Aubrun and C Leick. Sensor fault accommodation: Application to an activated sludge process. *IFAC Proceedings Volumes*, 38(1):371–375, 2005. ISSN 1474-6670.

[131] Saed Hussain, Maizura Mokhtar, and Joe M Howe. Sensor failure detection, identification, and accommodation using fully connected cascade neural network. *IEEE Transactions on Industrial Electronics*, 62(3):1683–1692, 2015. ISSN 0278-0046.

[132] Youmin Zhang and Jin Jiang. Bibliographical review on reconfigurable fault-tolerant control systems. *Annual Reviews in Control*, 2008. ISSN 13675788. doi: 10.1016/j.arcontrol.2008.03.008.

[133] Ihab Samy, Ian Postlethwaite, and Da Wei Gu. Survey and application of sensor fault detection and isolation schemes. *Control Engineering Practice*, 2011. ISSN 09670661. doi: 10.1016/j.conengprac.2011.03.002.

[134] Philippe Goupil. AIRBUS state of the art and practices on FDI and FTC in flight control system. *Control Engineering Practice*, 2011. ISSN 09670661. doi: 10.1016/j.conengprac.2010.12.009.

[135] Samuel Toma, Laurent Capocchi, and Gerard Andre Capolino. Wound-rotor induction generator inter-turn short-circuits diagnosis using a new digital neural network. *IEEE Transactions on Industrial Electronics*, 2013. ISSN 02780046. doi: 10.1109/TIE.2012.2229675.

[136] R. Isermann and P. Ballé. Trends in the application of model based fault detection and diagnosis of technical processes. *Control Eng. Practice*, 1997. ISSN 09670661. doi: 10.1016/S0967-0661(97)00053-1.

[137] Tom Kuzin and Tom Borovicka. Early Failure Detection for Predictive Maintenance of Sensor Parts.

[138] Nilesh Subhash Nalawade and Minakshee M Pawar. Forecasting telecommunications data with Autoregressive Integrated Moving Average models. In *Recent Advances in Engineering & Computational Sciences (RAECS), 2015 2nd International Conference on*, pages 1–6. IEEE, 2015. ISBN 1467382531.

[139] Le Roy F Simmons. M-competition - A closer look at NAIVE2 and median APE. A note. *International Journal of Forecasting*, 1986. ISSN 01692070. doi: 10.1016/0169-2070(86)90092-0.

[140] Everette S. Gardner. Exponential smoothing: The state of the art-Part II. *International Journal of Forecasting*, 2006. ISSN 01692070. doi: 10.1016/j.ijforecast.2006.03.005.

[141] Prapanna Mondal, Labani Shit, and Saptarsi Goswami. Study of effectiveness of time series modeling (ARIMA) in forecasting stock prices. *International Journal of Computer Science, Engineering and Applications*, 4(2):13, 2014. ISSN 2231-0088.

[142] George E P Box and George C Tiao. Intervention analysis with applications to economic and environmental problems. *Journal of the American Statistical association*, 70(349):70–79, 1975. ISSN 0162-1459.

[143] George E P Box, Gwylim M Jenkins, and Gregory C Reinsel. Time Series Analysis: Forecasting and Control. *Journal of Time Series Analysis*, 2013. ISSN 01439782.

[144] Zongliang Qiao, Jianxin Zhou, Fengqi Si, Zhigao Xu, and Lei Zhang. Fault diagnosis of slurry pH data base on autoregressive integrated moving average and least squares support vector machines. In *Natural Computation (ICNC), 2013 Ninth International Conference on*, pages 141–145. IEEE, 2013. ISBN 1467347140.

[145] Chang Shou Luo, Li Ying Zhou, and Qing Feng Wei. Application of SARIMA Model in Cucumber Price Forecast. *Applied Mechanics and Materials*, 2013. ISSN 16609336. doi: http://dx.doi.org/10.4028/www.scientific.net/AMM.373-375.1686.

[146] Tsan Ming Choi, Yong Yu, and Kin Fan Au. A hybrid SARIMA wavelet transform method for sales forecasting. *Decision Support Systems*, 2011. ISSN 01679236. doi: 10.1016/j.dss.2010.12.002.

[147] Habib Allah Mombeni, Sadegh Rezaei, Saralees Nadarajah, and Mahsa Emami. Estimation of Water Demand in Iran Based on SARIMA Models. *Environmental Modeling and Assessment*, 2013. ISSN 14202026. doi: 10.1007/s10666-013-9364-4.

[148] Kalid Yunus, Torbjorn Thiringer, and Peiyuan Chen. ARIMA-Based Frequency-Decomposed Modeling of Wind Speed Time Series. *IEEE Transactions on Power Systems*, 2016. ISSN 08858950. doi: 10.1109/TPWRS.2015.2468586.

[149] A.K. Rajeevan, P.V Shouri, and Usha Nair. ARIMA Based Wind Speed Modeling for Wind Farm Reliability Analysis and Cost Estimation. *Journal of Electrical Engineering and Technology*, 2016. ISSN 1975-0102. doi: 10.5370/JEET.2016.11.4.869.

[150] Javier Contreras, Rosario Espinola, Francisco J Nogales, and Antonio J Conejo. ARIMA models to predict next-day electricity prices. *IEEE transactions on power systems*, 18(3):1014–1020, 2003. ISSN 0885-8950.

[151] A Geetha and G M Nasira. Time series modeling and forecasting: Tropical cyclone prediction using ARIMA model. In *2016 3rd International Conference on Computing for Sustainable Global Development (INDIACom)*, pages 3080–3086, 2016.

[152] Rodrigo N. Calheiros, Enayat Masoumi, Rajiv Ranjan, and Rajkumar Buyya. Workload prediction using ARIMA model and its impact on cloud applications' QoS. *IEEE Transactions on Cloud Computing*, 2015. ISSN 21687161. doi: 10.1109/TCC.2014.2350475.

[153] Rob J Hyndman and George Athanasopoulos. *Forecasting: Principles and Practice: Notes*. 2014.

[154] Alysha M De Livera, Rob J Hyndman, and Ralph D Snyder. Forecasting time series with complex seasonal patterns using exponential smoothing. *Journal of the American Statistical association*, 106(496):1513–1527, 2011. ISSN 0162-1459.

[155] Sutharshan Rajasegarar, Christopher Leckie, and Marimuthu Palaniswami. Hyperspherical cluster based distributed anomaly detection in wireless sensor networks. *Journal of Parallel and Distributed Computing*, 2014. ISSN 07437315. doi: 10.1016/j.jpdc.2013.09.005.

[156] S.a Subramaniam, T.b Palpanas, D.c Papadopoulos, V.c Kalogeraki, and D.c Gunopulos. Online outlier detection in sensor data using non-parametric models. In *VLDB 2006 - Proceedings of the 32nd International Conference on Very Large Data Bases*, 2006.

[157] J.W. Branch, C. Giannella, B. Szymanski, R. Wolff, and H. Kargupta. In-network outlier detection in wireless sensor networks. *Knowledge and Information Systems*, 2013. ISSN 02191377 02193116. doi: 10.1007/s10115-011-0474-5.

[158] Mahmoud Reza Saybani, Teh Ying Wah, Amineh Amini, and Saeed Reza Aghabozorgi Sahaf Yazdi. Anomaly detection and prediction of sensors faults in a refinery using data mining techniques and fuzzy logic. *Scientific Research and Essays*, 6(27):5685–5695, 2011. ISSN 1992-2248.

[159] H Zare Moayedi and M A Masnadi-Shirazi. Arima model for network traffic prediction and anomaly detection. In *2008 International Symposium on Information Technology*, volume 4, pages 1–6, 2008. ISBN 2155-8973. doi: 10.1109/ITSIM.2008.4631947.

[160] Xiao He, Zidong Wang, Yang Liu, Liguo Qin, and Donghua Zhou. Fault Tolerant Control for an Internet-Based Three-Tank System: Accommodation to Sensor Bias Faults. *IEEE Transactions on Industrial Electronics*, 2016. ISSN 0278-0046.

[161] Keith W Hipel and A Ian McLeod. *Time series modelling of water resources and environmental systems*, volume 45. Elsevier, 1994. ISBN 0080870368.

[162] Jiban Chandra Paul and Shahidul Hoque. Selection of best ARIMA Model for Forecasting Average Daily Share Price Index of Pharmaceutical Companies in

Bangladesh: A Case Study on Square Pharmaceutical Ltd. *Global Journal of Management and Business Research*, 2013.

[163] George E P Box, Gwilym M Jenkins, Gregory C Reinsel, and Greta M Ljung. *Time series analysis: forecasting and control*. John Wiley & Sons, 2015. ISBN 1118675029.

[164] Ratnadip Adhikari and R K Agrawal. An introductory study on time series modeling and forecasting. *arXiv preprint arXiv:1302.6613*, 2013.

[165] I.Bustoni I.A. Permanasari, A.E. Hidayah. SARIMA (Seasonal ARIMA) implementation on time series to forecast the number of Malaria incidence. *Information Technology and Electrical Engineering (ICITEE),2013 International Conference* ., 2013. doi: 10.1109/ICITEED.2013.6676239.

[166] Rob J. Hyndman and Yeasmin Khandakar. Automatic time series forecasting: The forecast package for R. *Journal Of Statistical Software*, 2008. ISSN 10411135. doi: 10.18637/jss.v027.i03.

[167] Denis Kwiatkowski, Peter C.B. Phillips, Peter Schmidt, and Yongcheol Shin. Testing the null hypothesis of stationarity against the alternative of a unit root. *Journal of Econometrics*, 1992. ISSN 03044076. doi: 10.1016/0304-4076(92)90104-Y.

[168] Ralph D Snyder, J. Keith Ord, and Anne B Koehler. Prediction Intervals for ARIMA Models. *Journal of Business & Economic Statistics*, 2001. ISSN 0735-0015. doi: 10.1198/073500101316970430.

[169] Ronald L. Wasserstein. The ASA's statement on Statistical Significiance and P-values. *The American Statistician*, 2016. ISSN 0003-1305. doi: 10.1080/00031305.2016.1154108.